POLITECNICO DI TORINO

Collegio di Ingegneria Chimica e dei Materiali

Master of Science Course in Materials Engineering for Industry 4.0

Master of Science Thesis

Optimization of piezoelectric thin film sputtering



Tutor

prof. Carlo Ricciardi

Candidate

Matteo Gambato Guidastri

Abstract

Piezoelectric thin films play a crucial role in the modern communication world, as they are the core of radio frequency (RF) filters used in virtually all mobile devices. These components ensure the transmission and reception of signals at specific frequencies. Surface Acoustic Wave resonators (SAW) and Bulk Acoustic Wave (BAW) resonators are the current standard for piezoelectric-based RF filters, with Aluminum Nitride (AlN) being one of the most commonly used material. As mobile network technology advances, RF filters must work at higher frequencies with larger bandwidths, and the devices' designs and materials must be developed too. In this context, this thesis aims to optimize the sputtering deposition of piezoelectric thin films. The experimental work has been carried out in the Center of MicroNanotechnology (CMi) at the École Polytechnique Fédérale de Lausanne (EPFL) under the direction of the Advanced NEMS Laboratory led by Prof. Guillermo Villanueva. The optimization process focused on tuning the deposition parameters of a newly available sputtering tool, the Alliance Concept CT200 Clustertool. The research was organized keeping in mind the final application of the thin films. The optimization process hence included the development of a quality bottom electrode in Platinum, the deposition of AlN thin films, and the characterization of their properties. Finally, to study the piezoelectric properties of the deposited films, a Free-Standing Bulk Acoustic Resonator (FBAR) microdevice was realized to analyze its frequency response. A brief investigation of the tool's potentiality of co-sputtering Sc-alloyed AlN (AlScN) was also carried out. Crystallographic measurements indicated the production of poly-crystalline AlN thin films with a good degree of orientation along the [001] direction (FWHM of the rocking curve: 1.72°), proving the efficacy of the tool to deposit piezoelectric thin films on the bottom electrodes. The Pt electrode also showed a good degree of crystallization along the [111] direction, and electrical measurement indicated films only 10% more resistive than the bulk material. Composition and thickness of the thin films were proven consistent over several depositions by measurements, while film crystallinity results were less conclusive, as they were influenced by tool contamination. The realization of FBAR was successful, and the frequency response measurement indicated that the device had an effective coupling coefficient k_{eff}^2 equal to 6.20%, compared to a theoretical value k_{33}^2 of 7.46%. This result proved that the AlN thin films deposited with the sputtering tool were compatible with RF microdevices. Finally, the composition analysis of the AlScN films proved the capability of the tool of co-sputtering films with a controlled doping content.

Contents

Al	ostrac	t	iii
1	Intr	oduction	1
	1.1	Aluminum Nitride and its piezoelectric properties	1
	1.2	Deposition of AlN thin films by Magnetron Sputtering	3
	1.3	Aluminum and Scandium Nitride	5
2	_	erimental method and instrumentation	7
	2.1	Process flow	7
	2.2	Thin film deposition instrumentation and substrates	9
		2.2.1 Alliance Concept CT200 Sputtering Cluster tool	9
		2.2.2 Pfeiffer SPIDER 600 Sputtering cluster tool	10
		2.2.3 Alliance-Concept EVA 451 Thermal Evaporator	11
		2.2.4 Substrates	11
	2.3	Microdevices realization instrumentation	11
		2.3.1 EVG 150 Automatic Coating and Development tool	11
		2.3.2 MLA150 Writing tool	11
		2.3.3 Nexus IBE350	12
		2.3.4 TMAH wet etching	12
		2.3.5 SPTS Xactix X4	13
		2.3.6 Tepla GIGAbatch and Tepla 300	13
	2.4	Characterization techniques and instrumentation	13
		2.4.1 Curvature measurements with Toho Technology FLX2320-S	13
		2.4.2 Sheet resistance measurement with Filmetrics R50 - 200 - 4PP	14
		2.4.3 Spectroscopic ellipsometry for thickness determination with Woollam RC2	15
		2.4.4 Surface Microroughness measurement with Bruker Dimension FastScan AFM .	15
		2.4.5 Scanning Electron Microscopy and Composition analysis with Zeiss MERLIN .	16
		2.4.6 X-Ray analysis with Bruker D8 Discover Plus TXS	16
		2.4.7 Frequency response measurements with Rohde & Schwarz ZNB20	18
			- 0
3		om electrode development	19
	3.1	Material selection	19
	3.2	Adhesion layer deposition	20
	3.3	Sputtering power influence tests	20
	3.4	Process pressure influence test	22
	3.5	Optimized recipe tests and chamber contamination	26
	3.6	Spider600 bottom electrodes	27
4	Piez	oelectric layer deposition	29
•	4.1	Reference setting and preliminary depositions	29
	4.2	Depositions pressure test	31
	4.3	Substrate bias test	34
	4.4	Gas ratio test	36
	4.4	Optimized recipe and deposition on patterned electrode	39
	4.6	Sc alloying calibration test	39 41
	4.0	be anothing callulation test	+ 1

5	Mic	rodevices realization	45
	5.1	FBAR design	45
	5.2	HBAR development	47
		5.2.1 First HBAR design	
			48
	5.3	FBAR realization	51
	5.4		
6	Con	clusions	57
Li	st of l	Figures	60
Li	st of [Tables	61
Ał	brev	iation and symbol list	63
	6.1	Symbols	63
	6.2	Abbreviations	64
Re	feren	nces	73
Ac	knov	vledgments	75

1. Introduction

Modern telecommunications employ a wide range of signal frequencies to deliver information in an ever more connected world. To be able to receive the information encoded in these signals, a device must be equipped with an appropriate filter able to separate useful frequencies from noise and unwanted signals. At the core of most Radio Filters chips lays a piezoelectric micro-electromechanical system, either in the configuration of a Bulk Acoustic Wave (BAW) Resonator or Surface Acoustic Wave (SAW) Resonator. These devices utilize a thin piezoelectric layer to generate a clear response to a determined input frequency with Aluminum Nitride (AIN) being one of the most used material for this application. The advancement of communication technologies requires that RF Filters work at higher frequencies and broader bandwidths. To do so both the research on devices design and materials must be developed further.

In this context, this thesis aims at optimizing the deposition by sputtering of AlN thin piezoelectric films using the Alliance Concept CT200 Cluster Sputtering tool. The resulting thin films must have adequate properties for the integration in microdevices. In order to do so, the experimental work unfolded in three parts: the development of a Pt layer, with optimized properties to function both as a growth template for the piezoelectric layer and as a bottom electrode; the optimization of the deposition parameters for the AlN piezoelectric layer; and finally the development of a simple Free-standing Bulk Acoustic Resonator (FBAR) to prove that the process is compatible with the realization of microdevices and to assess the piezoelectric quality of the film. To assess the quality of the thin films deposited with the CT200 tool, several direct characterization techniques are employed, in particular X-Ray Diffraction Measures to determine the crystalline properties of the thin films and Spectroscopic Ellipsometry to measure the film thickness and uniformity. The characterization of piezoelectric properties is done by studying the frequency response of the FBARs.

This thesis is divided in chapters according to the work outline described above. This chapter is dedicated to the introduction of Aluminum Nitride, its piezoelectric properties sputtering deposition and Scandium doping. Chapter 2 covers the experimental methods and details. Chapter 3 focuses on the development of the Pt bottom electrode, discussing the material selection and the various depositions processes. In Chapter 4 the optimization process for the AlN deposition is discussed, and the potentiality of the machine to produce Sc-doped AlN thin layers is briefly investigated. The development of the microdevices and the results of the frequency response measurement are discussed in Chapter 5. Finally, Chapter 6 ties together the results of every step to draw the conclusions of this work.

1.1 Aluminum Nitride and its piezoelectric properties

Aluminum Nitride is a III-V semiconductor, characterized by excellent mechanical, thermal, electrical, chemical and optical properties. The main properties highlighted by literature are the high thermal conductivity, in the order of 300 W m $^{-1}$ K $^{-1}$ [1], the wide direct band gap of 6.2 eV [2], the high acoustic velocity, in the range of 10^4 m s $^{-1}$ [3]. AlN crystallizes in a wurtzite lattice under normal pressure conditions, with cell parameters a = 0.3110 nm, c = 0.4980 nm [4]. The wurzite crystalline lattice, reported in Figure 1.1, is not centro-symmetric, and this causes the formation of an electric dipole moment in the crystalline cell along the c-direction. The dipole moment density, or polarization, varies when the material is subjected to an external stress that modifies the interatomic distance along the c-axis. At the same time, and external electrical field applied to the material can deform the crystalline lattice, generating a strain in the material. These two phenomena are the direct and inverse piezoelectric effect, that allow AlN to be used to convert mechanical energy into electrical energy and viceversa. Piezoelectricity is at the core of several kinds of Micro Electro Mechanical Systems (MEMS), including Frequency Filters [5, 6], Energy Harvesters [7–9], Sensors [10, 11] and Precision transducers [12].

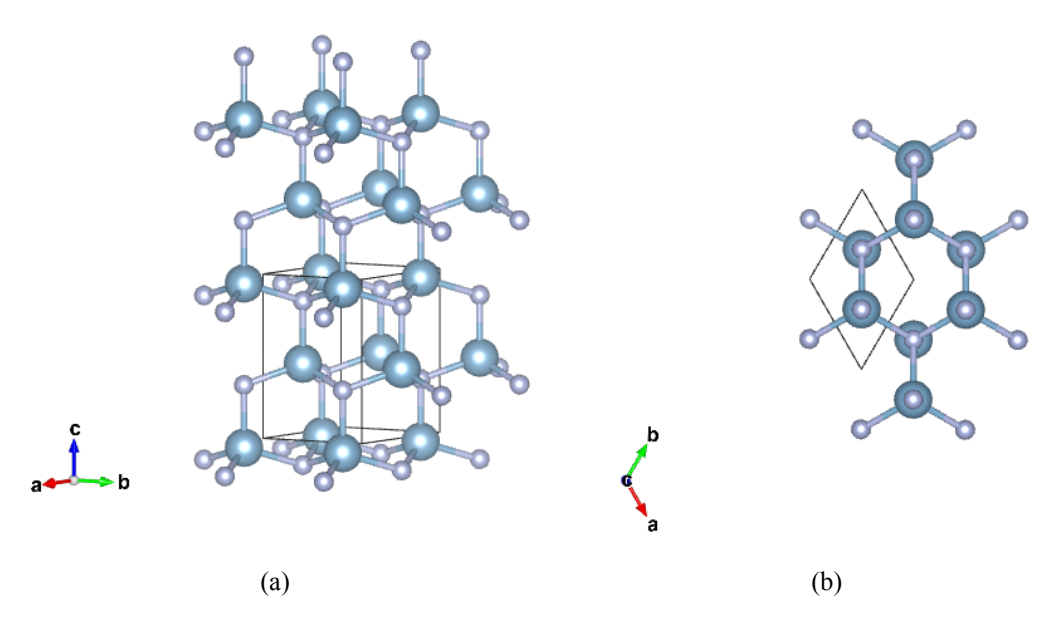


Figure 1.1: AlN wurtzite crystalline lattice, view from a plane parallel (a) and perpendicular (b) to c direction [4, 13]

Piezoelectricity can be be modeled as a linear interaction between the electrical and mechanical state of the material. The resulting fundamental equations of piezoelectricity (Eq 1.1 to 1.4), that express the relationship between stress T, strain S, electric field E and electric displacement D can be reported as:

$$S = s^E T + d^t E (1.1)$$

$$D = dT + \varepsilon^T E \tag{1.2}$$

$$T = c^E S + e^t E ag{1.3}$$

$$D = e S + \varepsilon^S E \tag{1.4}$$

In which s^E is the elastic compliance matrix at constant electrical field, d and its transpose d^t are the matrix of piezoelectric strain coefficients, ε^T is the permittivity matrix measured at fixed stress, c^E is the stiffness matrix at constant electrical field, e is the matrix of piezoelectric stress coefficients and ε^S is the permittivity matrix at constant strain [14]. Eq 1.1 and 1.2 use the Stress-Charge notation and Eq 1.3 and 1.4 use the Strain-Charge notation, which are interchangeable using Eq 1.5 to 1.7:

$$s^E = \frac{1}{c^E} \tag{1.5}$$

$$d = \frac{e}{c^E} \tag{1.6}$$

$$\varepsilon^T = \varepsilon^S + De \tag{1.7}$$

For AlN, considering the symmetry of the lattice, Eq 1.1 and Eq 1.2 can be rewritten with the Voigt notation as Eq 1.8 and 1.9:

$$\begin{bmatrix} S_{1} \\ S_{2} \\ S_{3} \\ S_{4} \\ S_{5} \\ S_{6} \end{bmatrix} = \begin{bmatrix} s_{11}^{E_{1}} & s_{12}^{E_{2}} & s_{13}^{E_{3}} & 0 & 0 & 0 \\ s_{21}^{E_{1}} & s_{22}^{E_{2}} & s_{32}^{E_{2}} & 0 & 0 & 0 \\ s_{21}^{E_{2}} & s_{22}^{E_{2}} & s_{33}^{E_{2}} & 0 & 0 & 0 \\ s_{31}^{E_{2}} & s_{32}^{E_{2}} & s_{33}^{E_{3}} & 0 & 0 & 0 \\ 0 & 0 & 0 & s_{44}^{E_{4}} & 0 & 0 \\ 0 & 0 & 0 & 0 & s_{55}^{E_{5}} & 0 \\ 0 & 0 & 0 & 0 & 0 & s_{66}^{E_{5}} \end{bmatrix} \begin{bmatrix} T_{1} \\ T_{2} \\ T_{3} \\ T_{4} \\ T_{5} \\ T_{6} \end{bmatrix} + \begin{bmatrix} 0 & 0 & d_{31} \\ 0 & 0 & d_{32} \\ 0 & 0 & d_{33} \\ 0 & d_{24} & 0 \\ d_{15} & 0 & 0 \\ 0 & 0 & 0 \end{bmatrix} \begin{bmatrix} E_{1} \\ E_{2} \\ E_{3} \end{bmatrix}$$

$$(1.8)$$

$$\begin{bmatrix}
D_1 \\
D_2 \\
D_3
\end{bmatrix} = \begin{bmatrix}
0 & 0 & 0 & 0 & d_{15} & 0 \\
0 & 0 & 0 & d_{24} & 0 & 0 \\
d_{11} & d_{22} & d_{33} & 0 & 0 & 0
\end{bmatrix} \begin{bmatrix}
T_1 \\
T_2 \\
T_3 \\
T_4 \\
T_5 \\
T_6
\end{bmatrix} + \begin{bmatrix}
\varepsilon_{11} & 0 & 0 \\
0 & \varepsilon_{22} & 0 \\
0 & 0 & \varepsilon_{33}
\end{bmatrix} \begin{bmatrix}
E_1 \\
E_2 \\
E_3
\end{bmatrix}$$
(1.9)

Where for strain and stress components S_i and T_i , the subscript 1,2,3 denote normal strain and stress components along the main direction, and 4,5,6 shear stress and strain components. For the piezoelectric coefficients, d_{ij} and e_{ij} i denotes the direction in which the electric field is applied and j where the strain or stress is obtained. The piezoelectric coefficients are defined accordingly by Eq 1.10 and 1.11:

$$d_{ij} = \left(\frac{\partial S_j}{\partial E_i}\right)_T \tag{1.10}$$

$$e_{ij} = \left(\frac{\partial T_j}{\partial E_i}\right)_S \tag{1.11}$$

In AlN, direction 3 is assigned to the c-axis direction, and hence the main modes of piezoelectric excitation are the thickness mode, governed by d_{33} , and the transversal mode governed by d_{31} . The values of AlN piezoelectric coefficient reported in literature are 5.5 pC N⁻¹ for d_{33} [15] and -0.893 pC N⁻¹ for d_{33} [16]. These values however can vary greatly due to the quality of the material, its production methods, and the configuration with which the measurement was conducted.

All piezoelectric material present a critical temperature above which the non-centrosymmetry of their crystalline lattice is broken, and the material is no more capable of coupling electrical and mechanical energy. This temperature is defined as the piezolectric Curie temperature, and for AlN it is equal to 1150 °C [15]. AlN piezoelectricity can then be exploited at temperatures at which other piezoelectric materials loses their properties or undergo thermal decomposition [17]. The stability of AlN at high temperatures however is not the only property that makes this material suitable for MEMS production. Implementing AlN in piezoelectric MEMS offers several advantages [18]. For instance, the high stiffness coefficients and a relatively low density (3.255 kg m⁻3) give AlN excellent acoustic properties, such as high sound velocity and acoustic impedance, useful for the confinement of mechanical energy in Acoustic Wave Resonators. AlN thermal and chemical stability reduce significantly the risk of diffusion between different layers of the devices, and make the material suitable for the realization of sensors employable in aggressive environments. AlN can also be produced in form of thin films with a large number of depositions techniques, with an easier and better control over its stoichiometry compared to piezoelectric material made of ternary compounds, such as Lead Zirconate Titanate. Finally, thanks to this production flexibility, AlN is also depositable as an oriented polycrystalline thin film using Magnetron Sputtering at temperatures below 500°C, making it integrable with the production of Complementary Metal-Oxide-Semiconductor (CMOS) technologies [19].

1.2 Deposition of AlN thin films by Magnetron Sputtering

Sputtering is a Physical Vapor Deposition technique that utilizes a plasma to eject matter from a target cathode and deposit it on the desired substrate. As plasma is composed of electrically charged particles, it is capable of conducting current and magnetic field can be used to contain it in the proximity of the targets. The confinement implies a higher plasma density that make the sputtering more efficient. To deposit a material in a system like the one reported in Figure 1.2, the deposition chamber is firstly evacuated to a base pressure value set, then the sputtering gas, very frequently represented by Argon, is pumped in the chamber to reach the desired process pressure. The plasma is created by imposing a potential difference between the cathode and the anode. Depending on how the power is provided to the cathode,

the sputtering can be classified as Direct Current, in which the power is supplied continuously, as pulsed Direct current, in which the power supply is periodically shut off and as Radio Frequency, when the power source uses Alternated Current. The magnets responsible for the confinement of plasma are generally planar and located behind the target [20]. By implementing heating elements in the substrate holders it is also possible to deposit films at high temperature, to possibly enhance the properties of the film sputtered The deposition of AlN via sputtering requires the presence of Nitrogen in the sputtering gas. This variation of sputtering is defined as reactive sputtering, as the N_2 gas in the plasma gets ionized and reacts with the particles ejected from the target. The reaction however occurs also on the target. If the rate of sputtering is lower than the rate of reaction, on top of the target a layer of nitride is formed, poisoning it. The resulting nitride is dielectric, and if the sputtering power is being supplied continuously, charges accumulate on the surface of the target, reducing or stopping completely the ion bombardment from the plasma. For this reason AlN sputtering is prevalently deposited in pulsed-DC or RF configuration. Target poisoning however can be used to control effectively the stoichiometry of the films at the expense of deposition rate. If the reaction rate and etching rate of the nitride on the target are equal, the deposition rate is constant and both Al and N atoms are extracted with the same rate from the target.

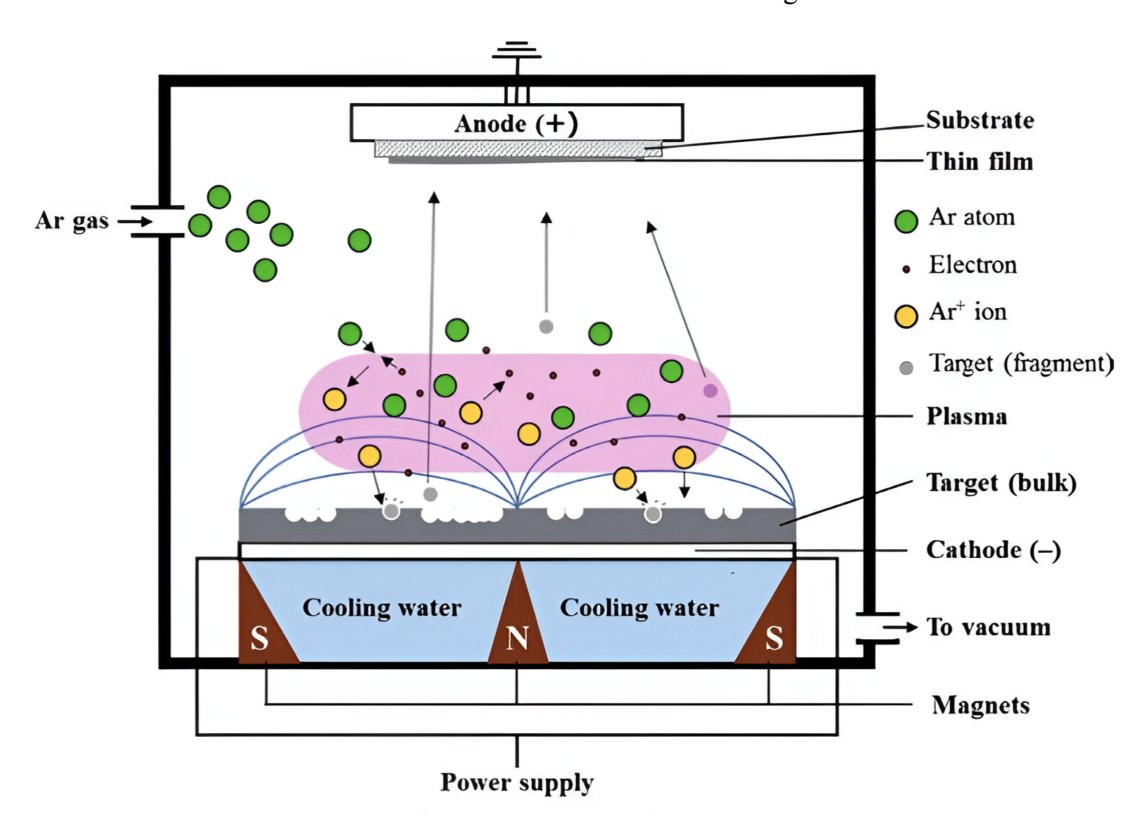


Figure 1.2: Schematics of a generic magnetron sputtering tool. Adapted from [19]

The operating parameters strongly influence the properties of sputtered films. The mean free path L_{mean} of particles in the plasma depends on its pressure and temperature according to Eq 1.12 [21]:

$$L_{mean} = \frac{k_b T}{\sqrt{2}P(4\pi r_{mean}^2)} \tag{1.12}$$

where k_b is the Boltzmann constant and r_{mean} is the mean radius of the constituent species in the plasma. The mean free can then be related to the collision probability Q_{hit} of a particle ejected from the target hitting the substrate at a distance D_{TS} 1.13:

$$Q_{hit} = 1 - \exp\frac{-D_{TS}}{L_{mean}} \tag{1.13}$$

If the substrate is put at a distance where Q_{hit} is below a certain value (0.5 for AlN in [21]) the film will always be amorphous. These relationship however is limited to the transport of the sputtered particles to the substrate, where the film growth also involves their adsorption, and the movement of the adsorbed atoms through surface and bulk diffusion. In order to obtain a determined crystalline structure, the particles impinging on the surface of the growing film must have and adequate energy that allows their adsorption and provides sufficient mobility to the adatoms. If the energy is too elevated, the particle can effectively damage the surface, while if it is too low, the adsorption might not happen or the mobility is then not sufficient to modify the microstructure. Thorthon [22] developed a zone model for the sputtering of metallic coating that related the obtained microstructure with the sputtering pressure and the temperature of the substrate, showing of these two parameters can be tuned to obtain a desired microstructure. For the deposition of AlN however a lot of parameters are involved in the determination of the final microstructure, especially if considering that the plasma composition is not uniform. Several studies have been carried out to determine the correlation between the sputtering condition and the final microstructure of AlN thin films [23, 24], with demonstration of the capability of producing AlN nanostructures or nanostructured films using magnetron sputtering [7, 25].

The main process parameters that are controlled for the deposition of AlN are the gas ratio of N_2 to Ar [6, 23, 26–29], the substrate temperature [6, 27, 29, 30], the sputtering power [23, 28] and the deposition pressure [23, 28, 29]. Other parameters that were also proved to be effective for depositing AlN with controlled microstructure were the configuration of magnetic field containing the plasma [31], the configuration of pulsed sputtering power [26] and the application of a bias to the substrate [23, 30].

It has to be pointed out that while general correlations can be traced between sputtering parameters and the resulting film properties, the complexity of the system implies each sputtering tool with different configuration has a different parameter tuning to obtain the desired microstructure of the AlN films. As the piezoelectric properties of AlN are maximum along the c-direction, the most common target configuration for these applications are polycrystalline films grown along the (002) planes, with the highest possible grain orientation in the c-direction [24].

1.3 Aluminum and Scandium Nitride

Despite the several excellent properties of AlN, its actual piezoelectric coefficients are modest if compared to other piezoelectric materials, such as Lead Zirconate Titanate, that can reach d_{33} values 75 times greater than those of AlN. [32] In order to address this issue, is possible to modify the composition of the material by adding Scandium, creating the Aluminum Scandium nitride alloy, AlScN. This can be done wither by mean of conventional magnetron sputtering using a target of Al-Sc alloy at fixed composition [33], or by the simultaneous sputtering of two targets. This technique is called co-sputtering and was used by Akiyama et al. [15], who were the first to report the effect of Sc concentration on the piezoelectric coefficient of AlScN, proving a five fold increase in the d_{33} coefficient compared to pure AlN with a Sc concentration of 43%. Thanks to co-sputtering by providing different powers to each target the Sc concentration in the film can be effetively regulated. The concentration at which the maximum peizoelectric coefficient was measured was also proved to be the limit for for which the material still exhibit piezoelectricity, as at Sc concentrations above 46% AlScN crystallizes in a cubic form, which is typical of ScN. The Sc doping modifies the lattice, increasing the a parameter while decreasing the c parameter. Tasnádi et al. explained this enhancement through ab-initio calculations [34]. As Al and Sc atoms compete to bond with N atoms, the lattice parameter decreases in the c direction and the lattice becomes more deformable. This in turn causes a softening of the elastic stiffness coefficient c_{33} , and doing so the material becomes more reactive to polarization, increasing the piezoelectric response. Following works [33, 35] proved this effect, which combined with a slightly higher density results in lower acoustic velocities in the c-direction. A further investigation conducted by Satoh et al. [36] on the phase transitions of the AlN-ScN system proved that in the range of Sc concentration between 35% and 43% the wurtzite and cubic crystalline structure coexist. This in turn can lead in the formation of Abnormally Oriented Grains, AOGs, that can reduce the piezoelectric response of the film and modify the stress distribution of the film [37]. The advantages of alloying AlN with ScN however are not limited to the increase in the piezoelectric response: above a Sc concentration of 27%, AlScN exhibit clear ferroelectric properties [38]. Ferroelectricity in a material is the presence of a spontaneous polarization in its crystalline lattice, which value and direction can be varied with the application of an external fields. While all ferroelectric material are piezoelectric, the opposite is not true, as demonstrated by the absence of ferroelectric properties of AlN. Thanks to the enhancement of piezoelectric properties and the acquisition of ferroelectricity, AlScN configures itself as a material capable of substituting AlN in most application. However, as the research in this field began only 16 years ago, AlScN technology is not as ready as the AlN's one to enter the phase of mass-production [39]. While control over the Sc concentration of film deposited has been managed from the beginning of Akiyama et al. research [15], the production of highly ordered and uniform has been more challenging, especially at higher Sc concentration.

2. Experimental method and instrumentation

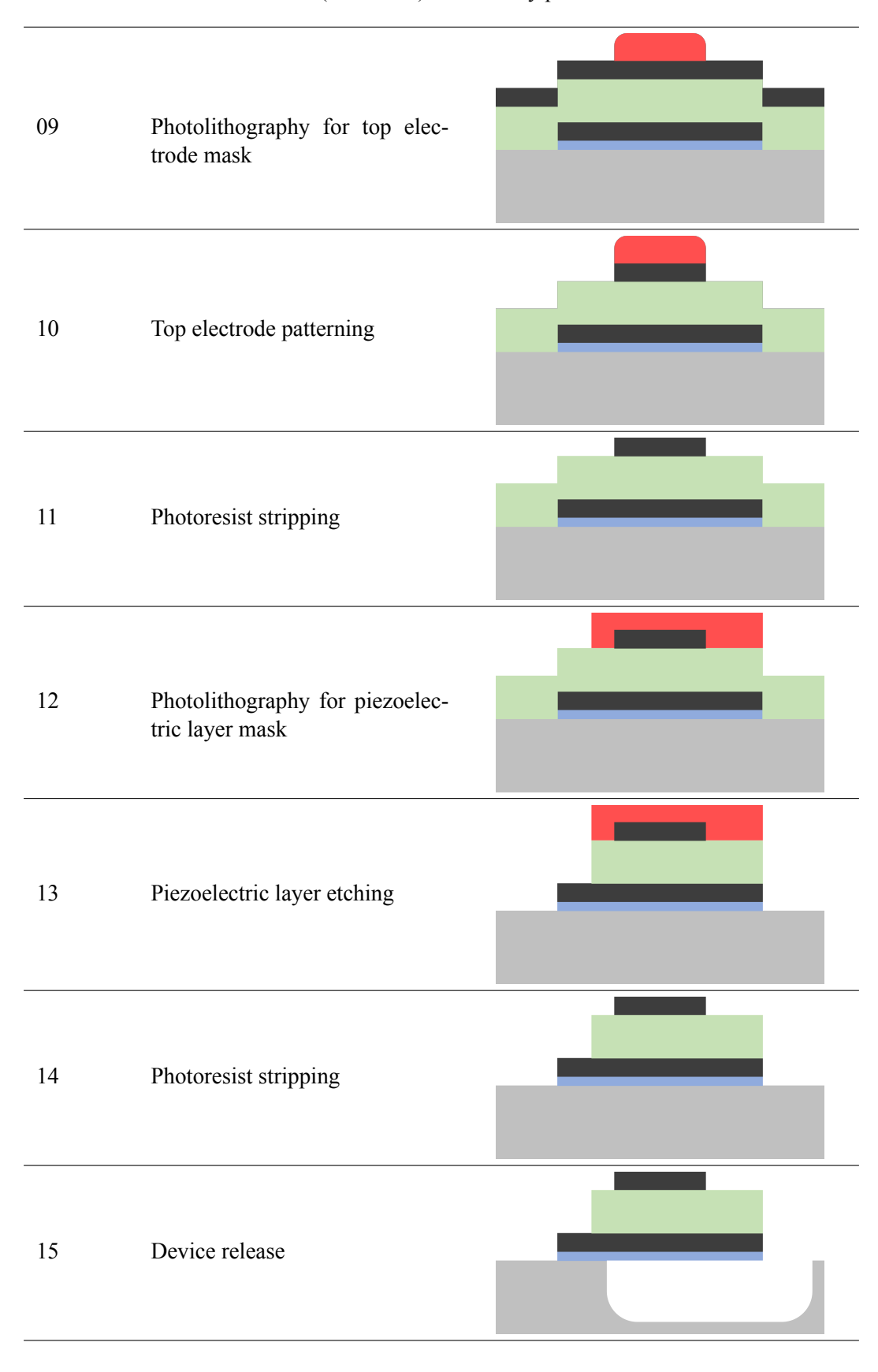
2.1 Process flow

To determine the experimental outline of the work, an initial process flow was developed. This process flow is aimed to produce FBAR devices by means of sputtering deposition of metal electrodes and piezoelectric layers, photolithography of photoresist masks for etching steps, Ion beam etching for patterning the electrodes, wet etch to pattern the AlN layer and Xenon diflouride etching for the release of the devices. The process flow is summarized in Table 2.1

Table 2.1: Preliminary process flow

Step	Process description	Cross-section after process
01	Wafer curvature measurement	
02	Adhesion layer deposition	
03	Bottom electrode deposition	
04	Photolithography for bottom electrode mask	
05	Bottom electrode patterning	
06	Photoresist stripping	
07	Piezoelectric layer deposition	
08	Top electrode deposition	

Table 2.1: (continued) Preliminary process flow



2.2 Thin film deposition instrumentation and substrates

2.2.1 Alliance Concept CT200 Sputtering Cluster tool

As stated in the Scope of Work section, the CT200 Sputtering Cluster by Alliance Concept [40], is the main experimental instrumentation, around which the optimization of deposition parameters is centered. In particular the tool utilizes four variations of Magnetron Sputtering: Radio-Frequency (RF) Sputtering, Direct Current (DC) Sputtering, pulsed DC (p-DC) Sputtering and High-Power Impulse Magnetron Sputtering (HiPIMS). The core of the machine is a transfer module equipped with a robotic arm that moves the samples between the chambers and the loadlock, all without breaking vacuum. The tool was configured to have five deposition chambers, each equipped with different targets and complementary equipment. All chambers except for PM 4 contain a heating system that can bring the substrate holder up to 950°C for high temperature depositions. All the chambers are equipped with throttle valves to control the pressure in the modules and two gauges to measure the pressure. The whole system and each chamber are outfitted with primary pumps and cryogenic or turbomolecular pump for High Vacuum. All the the substrate holders can be polarized with a RF generator. Figures 2.1 and 2.2 shows the configuration of the tool. The substrate holders are discs of stainless steel used to allow the robot to move the substrates for one chamber to another without directly touching it. In CMi they also are used as adapters, as the CT200 intended configuration is for 200 mm diameter wafers, while the most common size used for experimental purposes in the laboratory is 100 mm. This causes the substrate holders to have a significant thermal mass, which in turn causes a difference between the temperature set in the deposition program and the actual temperature measured on the wafer. For a set point of 500°C, the temperature measured on the wafer is around 350°C. All the following references to the deposition temperature concerning the CT200 will refer to the setpoint and not to the actual measured temperature on the substrate, which is obtainable only by positioning external thermocouples on the substrate. Additionally, before each high temperature process, a wait time of 15 minutes is added to ensure that the wafer is heated properly. The depositions chambers, excluded PM 4, contain multiple sputtering targets (3 or 4) in a confocal configuration, tilted by about 15° and distant around 100 mm from the substrate. To ensure that the film thickness is homogeneous, the substrate is rotated during deposition.



Figure 2.1: Front view of CT200 cluster, showing the loadlock open and the control screens.



Figure 2.2: Back view of CT200 cluster, with all the modules open.

The chambers used in this work were Process Module (PM) 2, 4 and 6. PM 2 is dedicated to the deposition of oxides and metals and was used to deposit the Pt electrodes. This deposition chamber is equipped with three confocal targets with a diameter of 100 mm and RF and p-DC generators. The Pt target purity is of 99.99 %. he process gases available in this chamber are Ar, N_2 and O_2 . PM 4 is dedicated to the deposition of Silicon Oxide (SiO₂) by RF sputtering, and it is the only one capable of actively cooling the samples, and it was used in this work for that purpose for every high temperature deposition. PM 6 is dedicated to the deposition of nitrides and was used for the deposition of all the piezoelectric films. It is equipped with 3 confocal targets (Al, Sc, TiN) with a diameter of 100 mm and RF and p-DC generators. The Al and Sc target purity are respectively 99.999% and 99.99%. The process gases available are Ar and N_2 .

Before deposition, each chamber was pumped down to a base pressure of 10^-8 Pa. After that, the wafers were heated in the PM to reach the deposition temperature set, and a pres-sputtering step was done before the actual deposition, to clean the target from impurities. To avoid contaminating the films, this process was done with both the target and the substrate shutter closed. The deposition of nitrides was conducted by pulsed-DC reactive sputtering, with a pulse frequency of 20 kHz and an off-time of 5 μ s, in a Ar and N₂ mixture. Before the actual sputtering, a step in the process was dedicated to poisoning the target, to ensure that the films is sputtered with the right stoichiometry. The deposition of Pt used DC sputtering, with only Ar as the processing gas.

How the other deposition parameters were chosen and modified to test their influence on the thin films is reported in Chapters 3 and 4.

2.2.2 Pfeiffer SPIDER 600 Sputtering cluster tool

Due to several maintenance interventions occurring on the CT200 during the thesis duration, some metallic films were deposited using the cluster tool Pfeiffer SPIDER 600 [41], which is used for the sputtering of several materials. It is composed of four chambers each equipped with a 200mm diameter planar target and a plasma generator, either RF, DC or p-DC and a substrate RF generator. The substrate can also be heated, up to 350°C. Three process gases are available, Ar, N₂ and O₂. The pressure is also controlled with a throttle valve, that however can only be set in three different positions: the deposition pressure is in fact determined by the flux of process gases in the chamber. This tool has some advantages and disadvantages compared to the CT200: bigger targets allow for higher plasma powers, which in turn results in significantly higher deposition rates; on the other hand, only one material can be deposited at the same time on the substrate. As this tool was used as a replacement for the CT200 when it was not available and

only to deposit some metal films with no optimization, the results of these depositions are only briefly reported on Chapter 3.

2.2.3 Alliance-Concept EVA 451 Thermal Evaporator

EVA 451 by Alliance-Concept [42] is a thermal evaporator that was used in this work for the quick coating of dielectric samples for inspection with Scanning Electron Microscopy (SEM) or Energy Dispersive X-Ray Spectroscopy (EDX). The system is fitted with four thermal sources for the deposition of Cr, and with quartz microbalances to control the deposition rate. One source is also fitted with an additional quartz microbalance under the shutter to control more accurately the deposition rate. The substrate itself is mounted on a fixture that is actively cooled down to avoid the heating of the sample. This system was preferred over other evaporators as it utilizes a loadlock to maintain the evaporation chamber in vacuum thus reducing the time needed for the coating.

2.2.4 Substrates

For the deposition tests 100 mm p-doped <100> Si wafers were used. These wafers were 525 μ m thick, polished on only one side. They were acquired at the Center of MicroNanotechnology and produced by Siegert Wafer. For the realization of the devices 100 mm High Resistivity (HR) <100> Si wafers were used, to avoid parasitic currents developing in the substrate from the bottom electrodes. These wafers were also 525 μ m thick, but they were polished on both sides and acquired by the ANEMS Laboratory from the producer Biotain Crystal.

2.3 Microdevices realization instrumentation

For the realization of microdevices photolithography and different etching techniques were used. As the device's optimization was not in the goals of this work, simplicity and rapidity of processes were favored. The critical dimension for the photolithography was set to $1 \mu m$.

2.3.1 EVG 150 Automatic Coating and Development tool

EVG 150 Automatic Coating and Development tool The EVG 150 [43] is a cluster tool for the automatic coating and development of photoresists (PR). It is equipped with three spin-coating modules and a development module, eight hotplates and three coolplates. The tool is also capable of pretreatments for preparing the wafer's surface to be coated. All the wafers that were exposed during this work were coated with a positive photoresist, specifically AZ ECI 3007 by Merck [44] chemically amplified and sensitive to light with wavelengths ranging from 436 nm to 356 nm. The use of one formulation or the other was determined by the desired thickness of the PR mask: for thinner masks, below 1 µm, AZ ECI 3007 was used, while for thicker masks, around 2 µm, AZ ECI 3027 was used. Before each coating the wafers underwent a dehydration process to ensure a good adhesion of the coating to the layer that was going to be patterned. The development of the exposed PR consisted in a post exposure bake at 110°C for 90 s and then a coating of the wafer with a layer of AZ 726 MIF developer by Merck [45]. This is a water solution of 2.38% Tetramethylammonium Hydroxide (TMAH) with the addition of surfactant, that makes it suitable for puddle (this case) and immersion development. The development phase for the PR used in this work was 50 s. It is important to note that if the PR masked a metal layer that was going to be dry etched the coating was reflowed after exposure. In this process the PR is heated above its glass transition temperature, to reduce its surface roughness and produce rounded sidewalls, to avoid redeposition of metal bridges during the ion bombardment. This was done on a hotplate at 125 °C for 120s.

2.3.2 MLA150 Writing tool

The MLA150 by Heidelberg Instrument [46] is a laser writing tool that exposes photoresists without the need of producing a mask. The light is focused on and scanned over the sample following the design contained inside a digital file. The system has two light sources, at 375 nm and 405 nm that can expose PR at different intensities and focus length. The minimum feature size that this tool can successfully write

on a PR is of $1\mu m$, which is compatible with the design requirements of the devices. For the PR used in this work the wavelength used was always 405 nm, as its source had a higher power and ensured a shorter writing time. The machine was in general chosen to avoid the need to produce a mask for exposure that would have required much more work and validation steps.

2.3.3 Nexus IBE350

Nexus IBE350 by Veeco [47] is an ion beam etcher that utilizes an Inductively Coupled Plasma (ICP) to produce Ar ions. The ICP source has a diameter of 350 mm, which allows for the production of a highly uniform plasma. A system of three Molybdenum grids, the ion optics, then extracts, accelerates and collimates the ion beam. The ions can be accelerated with a voltage ranging from 50V to 800V, in accordance to the desired etch rate. The substrate to be etched is placed on a fixture that is actively cooled and always kept below 90°C during processing. The fixture can be rotated, up to 10 rpm and tilted from +90° to -70°. After the ion optics a plasma bridge neutralizer injects electrons into the ion beam to neutralize it. The electrons do not combine with the ions but ensure that no space or surface charging occurs. The system is also fitted with a Secondary Ion Mass Spectroscopy (SIMS) that detects in real time the mass and hence the chemical nature of the ions ejected from the substrate. The system is kept in vacuum by a turbomolecular pump, and a loadlock to insert the wafer to be etched without breaking the vacuum in the etching chamber. The system configuration is represented in Figure 2.3. The system was used for the etching of the electrodes, as they were realized with Platinum, a metal that can be wet etched only by aqua regia. The dry etching is highly directional. The etching parameters are reported in Chapter 5.

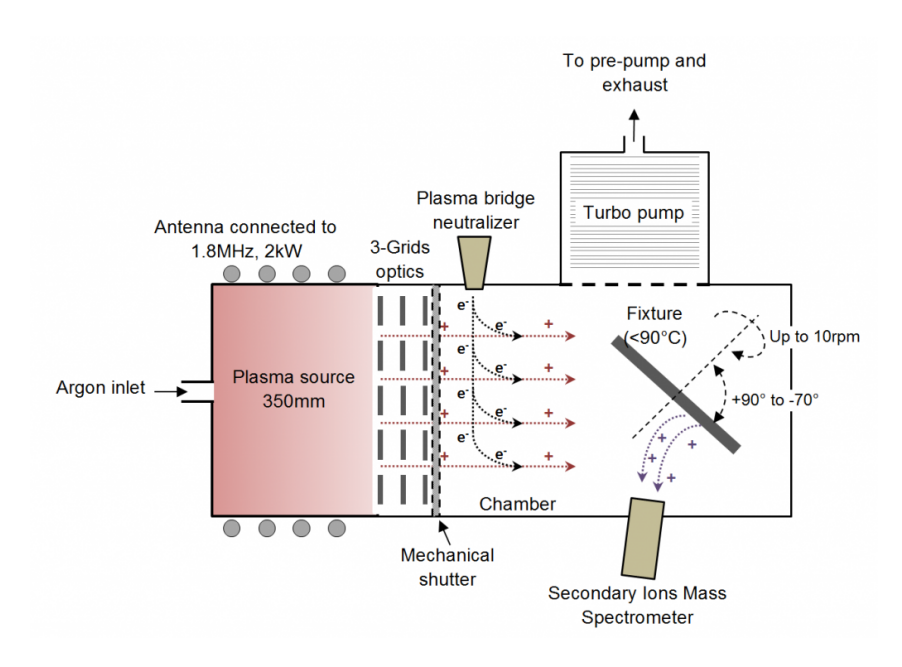


Figure 2.3: Schematics of IBE350. The loadlock is not represented.

2.3.4 TMAH wet etching

While also the piezoelectric layer can be etched with an ion beam, to simplify the production of the devices, the etching step of AlN was done in AZ 726 MIF developer [45], as it can be effectively used to etch both Aluminum and its Nitride. TMAH, the active principle of this developer, is an effective etchant of AlN. The developer itself was safer to handle than a maximum concentration solution of TMAH and provided a more controllable etch rate. The discussion of the wet etching parameter for the piezoelectric layer is reported in Chapter 5.

2.3.5 SPTS Xactix X4

SPTS Xactix X4 by KLA [48] is a Xenon Difluoride (XeF₂) etching system that is mainly used for the selective and isotropic etching of Silicon, in particular for the release of suspended microdevices. XeF_2 is a substance with a vapor pressure of $6.0 \cdot 10^2$ Pa at 298 K, about 4,5 torr. When in contact with Silicon it is adsorbed on the surface and split in Xe and F. The latter reacts with Si to form SiF_4 , which is gaseous, effectively etching the Si surface. This tool is composed of a chamber connected to a system of tubing and valves that allows for the controlled injection of etching vapors and purging of the residual vapors and products. The vapor is produced from a chamber containing solid XeF_2 that is heated to 35°C. The vapor is then directed in one of the two expansion chambers, where the pressure can be increased up to 6 torr. From the expansion chamber the vapor is sent to the etching chamber where it stays for the determined amount of time assigned for each etching cycle. While a cycle is ongoing, the other expansion chamber is filled with vapors to prepare the other cycle. The release of the microdevices was done with cycles of 45s at 5 torr. The results are reported in Chapter 5.

2.3.6 Tepla GIGAbatch and Tepla 300

Both the GiGAbatch and model 300 by PVA TePla [49] are microwave plasma systems used for the stripping of photoresist coatings after they are no longer needed. They utilize a high frequency Oxygen plasma to quickly oxide the polymer composing the photoresist, removing it from the surface of the wafer. The main difference between the two machines is the power that can be selected for the processes. These tools were always employed after each photolithography step, either by themselves if the carbon contamination was not important in the successive steps or combined with a wet PR stripping using the solvent SVC-14 [50] at 70°C for a combined time of 10 minutes. The wet PR stripping was especially used in the case that the PR had been exposed to degradation by Ion bombardment.

2.4 Characterization techniques and instrumentation

Several techniques were used to inspect the thin films deposited and their properties. While some properties were easily determined by a direct measurement or a simple formula, such as resistance, composition, crystalline orientation, the direct measurement of piezoelectric properties posed more challenges. In the first place, the instrumentation for a direct measurement of the piezoelectric constant according to the Berlincourt method [51] was not available. This quasistatic measurement procedure requires a double laser interferometer to detect the displacement of the film when subjected to an electric field. On the second hand, measuring the piezoelectric coefficient of thin films yields results that are strongly influenced by the geometrical configuration of the sample [52]. The coefficient measured directly differs from a bulk free-standing piezoelectric material due to the clamping acted from the substrate to the film. Keeping this in mind, the observation and characterization of piezoelectric properties of the thin films were done by studying the response of resonators microdevices.

2.4.1 Curvature measurements with Toho Technology FLX2320-S

The intrinsic stress of thin film is an important parameter that must be controlled to ensure that the film is suitable to be implemented in microdevices. Films too stressed bend when they are released from the substrate they are clamped to, and this in turn can break the microdevices realized with it. Stress can also modify the crystalline lattice, modifying other properties of the film. The variation of the radius of curvature of a wafer after the deposition of a layer on top of it can be correlated to the stress in the film. The correlation is represented by the Stoney Equation [53] (Eq 2.1):

$$T_f = \frac{1}{6} \frac{E}{1 - \nu} \frac{h^2}{t} \cdot \left(\frac{1}{R} - \frac{1}{R_0}\right) \tag{2.1}$$

In which T_f is the film built-in stress, E is the Young's modulus of the substrate, ν is the Poisson's modulus of the substrate, h is the thickness of the substrate, t the thickness of the film and R_0 and R are the curvature radius of the wafer before and after the deposition. The biaxial elastic modulus $E/(1-\nu)$

of Silicon is set equal to 180.5 MPa. To determine the stress of every layer it is then necessary to measure the curvature radius before and after its deposition. The FLX 2320-S by Toho Technology [54] uses two laser sources to scan the wafer and determine the angle of reflection in function of the distance from the scanning point. The slope of this function gives the curvature of the wafer, that is the inverse of the radius of curvature. The machine can vary the wavelength of the lasers to maximize the reflected signal. The manufacturer declares an accuracy of measurement of 1 MPa or lower than 2.5 % of the measurement. The latter value was used as the relative error for every curvature radius measured, as the software used in the machine does not account for the uncertainty of the film thickness. The minimum radius measurable by the machine is 2.0 m and the maximum is 33 km.

All the measurements of the curvature radius were done along the direction perpendicular to the wafers flat, identified as 0° and the direction parallel to the wafers flat, identified as 90° , to obtain an average value of the stress in the wafer.

2.4.2 Sheet resistance measurement with Filmetrics R50 - 200 - 4PP

One of the most important characterizations for metallic thin films is the measurement of sheet resistance. It is directly measured with a four-points probe system and is a quick assessment of the electrical properties of the thin film. If the thickness of the film is uniform in the area that is being measured, the resistivity of the film, ρ_e , is calculated the product of the sheet resistance R_{sh} and the film thickness t. Thanks to this correlation the sheet resistance values can be used both to evaluate the resistivity of the thin film but also estimate the thickness of a metal film with know resistivity. Considering a single metallic film, and supposing a uniform resistivity, a map of sheet resistance value can be used to determine the thickness distribution of the film. The measures were done by Filmetrics R50 - 200 -4PP by KLA Instruments [55]. This tool allows for the measurement and mapping of the sheet resistance of wafers, with an accuracy of \pm 1%, a repeatability lower than 0.5% and a range of measuring between 5 m Ω /sq and 5 M Ω /sq. All the wafers were measured on 25 points and the sheet resistance value reported was the arithmetic average, and the standard deviation as its error. Figure 2.4 is a map of sheet resistance of a bottom electrode layer, showing the disposition of the measured points on the wafer surface.

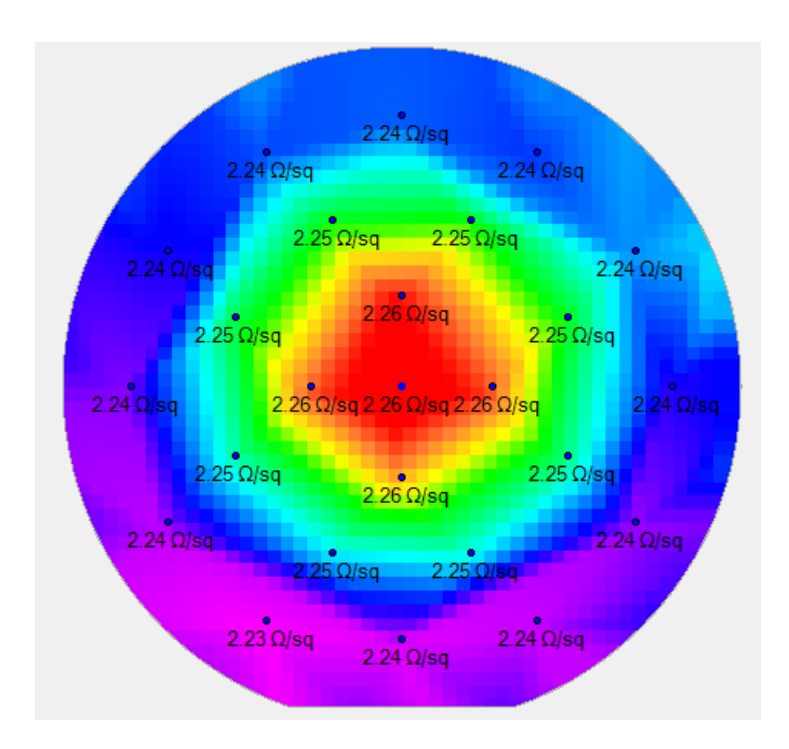


Figure 2.4: Measurement map of a sample Pt thin layer deposited with CT200.

2.4.3 Spectroscopic ellipsometry for thickness determination with Woollam RC2

The deposition rate of a material must be precisely determined to ensure that the fabrication process yields consistent results and the microdevices work as close as possible to the design specifications. To assess the deposition rate, thickness of test layers must be measured accurately. There are several characterization techniques that allow to characterize the thickness of a film, and in this work ellipsometry is used for the determination of the thickness of non-opaque films. Spectroscopic ellipsometry is an optical characterization technique that utilizes polarized light to determine the thickness of thin films and their optical properties. The name of the technique stems from the fact that the light that is analyzed is elliptically polarized. The polarized light beam is reflected by the surface of the wafer. The interaction of the light wave with the sample's materials has different effects on its components, in this case identified as parallel to the surface, s-direction or perpendicular to it, p-direction. The instrument measures two values: the variation Δ between the phase shift between the wave in the p-direction and the s-direction before and after the reflection; and the value Ψ , the angle whose tangent is the ratio between the magnitude of total reflection coefficient for the p- and s- directions, R_p and R_s . If the incident light is linearly polarized Δ is the opposite of the phase difference in the reflected beam. The fundamental equation of ellipsometry (Eq 2.2) correlates these two values:

$$\frac{R_p}{R_s} = \tan(\Psi)e^{i\Delta} \tag{2.2}$$

The instrument measures these two values in function of the incident wavelength and the incident angle. To derive the thickness and other optical properties of the film regression models are employed to fit the values measured [56]. The instrument used for these measures was the RC2 Ellipsometer by J.A. Woollam [57], equipped with a Xenon Arc Lamp (Power 75W) that can produce light with wavelength ranging from 210 nm (UV) to 2500 nm (NIR). The beam diameter is around 3 mm, and the stage is motorized to analyze several points of the wafer surface. The incident angle can be varied between 45° and 90°. The measures were used to determine the thickness of the piezoelectric layers and were carried out on 37 points per wafer with three angles of incidence, 55°, 65° and 75°. The fitting of the raw ellipsometry data were carried out in the CompleteEASE software by J.A. Woollam [58], and the value of thickness was the arithmetic average of the fitted thickness value of all point, and its standard deviation was considered as the absolute error. This method is not applicable for the determination of the thickness of metallic films above 10-20 nm, as they are completely opaque to the wavelengths used in this analysis, and the model requires the light to be reflected by a layer and the one under it to determine its thickness.

2.4.4 Surface Microroughness measurement with Bruker Dimension FastScan AFM

The physical configuration of a surface plays an essential role in several phenomena, including the growth of another layer on top of it and in the transmission and reflection of acoustic waves. Determining the surface roughness is then important to assess if a film contains defects, if it would work as a good growth layer or its properties (optical, acoustical ...) are fully exploitable in a microdevice. Depositing the thin film on polished surfaces, the roughness obtained are in the order of nanometers, and Atomic Force Microscopy (AFM) is an excellent technique to characterize surfaces at that resolution. This extremely high-resolution imaging technique utilizes a physical probe to scan the surface of a sample. The probe is mounted on a cantilever, which is deflected when the probe interacts with the surface at sub nanometric distances. A laser reflects on the cantilever, and a photodetector measures the deflection, reconstructing the intensity of the interaction and the topography of the sample. AFM can be conducted in different configurations, with the tapping mode being the most used and the one used in this work. In this case the cantilever is oscillated near its resonance frequency, with a constant amplitude. When the probe interacts with the sample, the oscillation amplitude changes, and this variation is fed back to the piezoelectric controls to adjust the height of the cantilever to maintain the amplitude constant. The Dimension FastScan AFM by Bruker [59] was used in this work to analyze the surface roughness of the thin films deposited to observe the presence of abnormally oriented grains and other deposition defects. All the measures were done with ScanAsyst Fluid+ [60] tips with a nominal tip radius of 20 nm. The scanning parameters that were adapted for each measure were the scan size, the scan rate and the number of samples per line. The images were analyzed with the NanoScope Analysis Software (v1.80) by Bruker [61]. The parameter chosen to represent the roughness of the surface was the quadratic mean roughness, R_q , which is derived from a set of N height measures z as follows (Eq 2.3):

$$R_q = \sqrt{\frac{1}{N} \sum_{i=1}^{N} z_i} \tag{2.3}$$

To derive the Roughness parameter, a 3-rd order plane fit was executed to remove the effect of the wafer tilting and bowing.

2.4.5 Scanning Electron Microscopy and Composition analysis with Zeiss MERLIN

SEM was used to inspect the results of the photolithography steps and eventual defects of the thin films. The MERLIN system by Zeiss is based on a GEMINI II [ZeissMerlin] column that uses a field emission gun and can accelerate the electron with a voltage up to 30 kV. The tool is equipped with three electron detectors: an in-lens secondary electron annular detector used for high resolution imaging; a Everhart-Thornley detector sensitive to secondary and backscattered electrons, used mainly for topography purposes; an annular in-column Energy Selective Backscattered detector used to observe compositional contrast. The system is also equipped with a X-Ray detector, the X-Max 50mm2 by Oxford Instruments [62], to perform compositional analysis by Energy Dispersive X-Ray spectroscopy, EDX. The accuracy of this measurement is about 1% atomic and is hindered by the volume of interaction of the electron beam in the sample, which is often greater than the thin film thickness. Nevertheless, EDX was chosen as the composition analysis technique as it is relatively quick and non destructive. Compositional analysis were carried out to quickly asses the correct stoichiometry of the nitride films and investigate the eventual presence of contaminants.

2.4.6 X-Ray analysis with Bruker D8 Discover Plus TXS

The piezoelectric properties of a thin film heavily depends on its crystalline configuration. The amount of crystalline phase, the dimensions and orientation of the crystalline grains determine how effectively the material convert electrical energy into mechanical and vice versa. Crystallinity is also important for the metal films, as it influences resistivity and the efficacy as growth layer for the AlN layers. X-Ray Diffractometry (XRD) was used to determine the crystallographic properties of the films. As X-Rays are a versatile probe for the analysis of materials, by slight modification of the measuring configurations, X-Ray Reflectrometry was also possible in the same tool. This technique was used to determine the thickness of the metal films.

XRD relies on the diffraction of X-Rays by crystalline lattices to identify the crystalline phases according to Bragg Equation (Eq 2.4):

$$n\lambda = 2d_{hkl}\sin\theta_B \tag{2.4}$$

Where n is an integer, λ is the wavelength of the radiation, d_{hkl} is the interplanar distance for the Miller indexes h, k, l and θ_B is the Bragg angle, for which constructive interference between reflected rays from the different crystalline planes is observed. XRD measures can be conducted moving the source and the detector at the same time, with the two moving symmetrically, giving this configuration the name of θ -2 θ scan, as the incident beam impinges on the sample at an angle θ and the detector captures a signal at an angle 2θ from the direction of the incident beam. This configuration is used to scan the sample to identify the crystalline phases present and their relative concentration [63]. Another information that can be obtained from θ -2 θ is the average crystalline domain size τ , employing the Scherrer Equation (Eq 2.5) [64]:

$$\tau = \frac{K\lambda}{\beta \cos \theta_B} \tag{2.5}$$

in which K is a geometrical parameter, (set to 0.89 in this work) and β is the Full Width Half Maximum (FWHM) of the diffraction peak, to which an instrumentation widening is 0.05° is removed. Another

configuration possible for an XRD measurement is the ω -scan, where the source angle (in this case indicated by ω) is varied in a small range centered around a Bragg angle θ_B , and the detector is set still at an angle $2\theta_B$. This kind of measurement is also called a rocking curve, as the source is rocked around the diffraction angle. The result is a bell curve that can be related with the orientation of a crystalline film. The width of this curve grows as the film becomes less oriented, contains more defects or as the surface of the sample becomes more curved. For thin film the rocking curve is used to determine whether the crystalline growth was correctly oriented and how much the orientation varies [63].

XRR instead exploits the reflection of X-Rays from the sample at low incident angles. Below a critical angle all the incident radiation is reflected, while increasing the angle the intensity diminishes. In case the film is composed of different layers, the intensity of the reflected beam oscillates with the angle of incidence. This effect is caused by the variation of electron density at the interfaces between layers, and by fitting the measurement with mathematical models it is possible to infer the thickness of the layer analyzed. It is worth noting that thicker layers produce oscillations that are closer to each other, complicating the model fitting and reducing the accuracy of the thickness value obtained. The measurement proceeds in the same way as a θ - 2θ scan, but for a lower range of angles [65].

Both XRD and XRR measurements were carried out with the D8 Discover Plus TXS by Bruker [66]. This XRD tool is fitted with the ATLAS Goniometer, which allows for a maximum angular deviation from the measured angle of 0.007° . The X-Ray source is a Turbo X-Ray Source (TXS), that utilizes electrons emitted by a tungsten wire via thermionic effect to bombard a copper cathode to emit X-Rays. The cathode spins at 104 rpm to spread the bombardment and emission on all the surface of the cathode, allowing for a more efficient dissipation of heat. This configuration of the source allows for a higher intensity of the X-Ray beam. The source emits X-Rays at a defined wavelength, nominally at 0.154060 nm, the Cu K- α 1 line, and 0.139222 nm, the K- β 1 line, which is not used for measuring due to its lower intensity. All the measures reported in this work occurred with the generator source set at 120 kV and 45 mA.

The detector is the EIGER2 500K [67], a solid-state detector with a large area composed of 500000 75x75µm² pixels. This detector supports three data acquisition modes: 0D, 1D and 2D, based on whether all the signal from each pixel is integrated over the whole area (0D), a line (1D) or reported as is (2D, not used in this work). The system is then equipped with different optic components to adapt the X-Ray beam to the measurement happening. Both for XRD and XRR measures a Göbel Mirror is mounted after the source. This parabolic mirror composed of several crystalline layers turns the divergent beam into a parallel one, with the downside of reducing its intensity. After the mirror a horizontal Ni collimation slit is mounted to reduce the dimension of the beam in the vertical axis. The slit used for XRD measures was 0.2 mm large, while the XRR measures were done with a 0.1 mm slit.

For the XRD configuration after the mirror and the slit a 2-bounce monochromator is mounted. In this device the incident beam hit on the first Ge crystal, that diffracts the beam to another Ge crystal, producing a highly monochromatic beam that allows for a high resolution of the measurement, at the cost of the beam intensity. On the other arm of the tool, a 2.5° Soller slit is put in front of the detector to reduce the divergence of the diffracted beam in the horizontal axis. This component is made of an array of vertical thin Cu parallel plates. Before each measure an alignment procedure was carried out. For the θ -2 θ scans, the 2 θ values varied between 32° and 72°, with an increment per step of 0.005° and an acquisition time of 0.1 s per step. The detector aperture was set to a square of 2°x 2°, the acquisition mode was set to 1D. The rocking curves were carried out after identifying the peaks with the 2 θ scans, and the indecent angle varied by 15°, centered around the θ B detected. The increment per step was 0.01° and the acquisition time per step was 0.1 s. The θ -2 θ scans are comparable to each other thanks to the presence of the Si (100), that is used as reference to normalize the intensity of different scans.

For the XRR measures after the Ni slit a 2.5° Soller slit was mounted, and a motorized slit was installed in front of the detector, and set to the minimum aperture, 0.01 mm. 2θ varied between 0.2° and 5.999° degrees, with steps of 0.003°, with an acquisition time of 0.2 s per step. XRD results were analyzed with the Diffrac.Eva software by Bruker [68]. The Bragg's angles θ_B were determined as the one with the highest signal intensity. The peaks were fit with gaussian curves to obtain the FWHM.

XRR results were analyzed with Diffrac.Leptos by Bruker [69]. The curves were fit using VarMetrix - Simplex algorithm, and the error of the fit was used as absolute error for the thickness values.

2.4.7 Frequency response measurements with Rohde & Schwarz ZNB20

As was stated above, the piezoelectric properties of the AlN films were characterized by measuring the frequency response of microdevices. To do so the devices were activated with a Ground-Signal-Ground (GSG) probe, the T26A by MPI [70], connected to a Vector Network Analyzer (VNA), the ZNB20 by Rohde & Schwarz [71]. The Probe has a characteristic impedance of 50 Ω , a frequency range up to 26 GHz, an insertion loss lower than 0.4 dB and a return loss greater than 16 dB. The VNA has a frequency range from 100 kHz to 20 GHz and a dynamic range of 140 dB. The measures were done after an Open-Short-Match calibration. The results are discussed in Chapter 5.

3. Bottom electrode development

3.1 Material selection

The first step to creating a suitable bottom electrode was the deposition of a metallic film that could allow the growth of an oriented crystalline layer. The goal thickness of the bottom electrode was set to 50 nm, as it would be a suitable thickness for an FBAR device, avoiding an excessive mass loading of the resonator [72]. Metallic films of these thicknesses exhibit higher resistivity than the bulk material, as the surface scattering of electrons has a greater effect on the conduction of charge in the film [73]. In the selection of the material, it is also important to consider the deposition conditions for the piezoelectric thin film. The AlN would have been deposited by reactive sputtering at high temperature, so the bottom electrode must be able to withstand these conditions, not react with the N_2 plasma and be stable at the selected temperature. To promote an oriented growth of AlN, which has a wurtzite crystalline structure, the underlying layer should have a hexagonal texture, such as the (111) face of face-centered cubic lattice (fcc) [74]. The lattice parameters of the growth layer as close as possible to AlN to reduce the strain of the sputtered film and the amount of defects in it [75].

Researching literature, several metals had been used as substrate for the growth of AlN, including Al [74–77], Au [75], Cu [77], Mo [74–78], Pt [74, 75] and Ti[74, 75, 77]. While Al, Au, Cu and Pt have fcc lattices, Mo has a body-centered cubic lattice (bcc) and Ti has a hexagonal close-packed (hcp) lattice. Mo is considered despite its lattice mismatch with AlN for bottom electrode production due to its high acoustic impedance and relatively low resistivity [78]. Other properties that an ideal bottom electrode should have are: a thermal expansion coefficient close to AlN (for high temperature depositions), ease of patterning and ease of deposition. In Table 3.1 the values for the metals cited are reported.

Table 3.1: Summary of metal properties. AlN properties reported too at the end. The mismatch refers to the in-plane lattice parameter [79–85].

Metal	lattice	direction	a (pm)	mismatch %	$\alpha (10^{-6} \text{K}^{-1})$	ρ_e (n Ω m)	$\rho (\mathrm{g \ cm^{-3}})$
Al	fcc	(111)	404.93	7.99	22.87	26.5	2.699
Au	fcc	(111)	407.86	7.33	14.13	21.92	19.283
Cu	fcc	(111)	361.5	17.86	16.64	16.76	8.935
Mo	bcc	(110)	314.71	12.42	5.1	53.4	10.223
Pt	fcc	(111)	392.36	10.85	8.93	100.87	21.452
Ti	hcp	(0001)	295.05	5.19	9.68	7.86	4.502
AlN	wurt. (a)	(0001)	311.0	-	4.2	-	3.255
	wurt. (c)		498.0	-	5.3	-	

The material that was selected for the bottom electrode was Pt, as the AlN films deposited on it were the one with the best orientation [74, 75]. Pt also exhibits good stability at the process temperature and does not react with the N_2 plasma. Its high density and high resistivity can affect the quality of the resonators produced with it, but in accordance with the scope of this work the quality of the AlN film was privileged over the quality of the microdevices. Pt however shows poor adhesion to Si, so an adhesion layer must be implemented. AlN shows good adhesion to Si [86] and Pt shows good adhesion to AlN [87]. In addition, AlN diffuses in Pt happens only at temperatures above 900° [88] . AlN was chosen as an adhesion layer to reduce the number of materials sputtered. The target thickness for the adhesion layer was initially set to 20 nm. The influence of the adhesion layer was also analyzed.

3.2 Adhesion layer deposition

After the selection of Pt as the bottom electrode material, a brief investigation of the AlN adhesion layer was carried out, mainly to determine the deposition rate of AlN at different sputtering power for the Al cathode. This had not been tested for powers over 200 W in the CT200 machine. The first deposition of AlN was carried out with the deposition parameters reported in Table 3.2, which are based on a deposition recipe developed by CMi staff to ensure the complete poisoning of the Al cathode.

Table 3.2: Deposition parameters for the adhesion layer test

Wafer #	$P_{Al}(W)$	P (Pa)	F_{Ar} (sccm)	F_{N2} (sccm)	T_{dep} (°C)	$\overline{t_{dep}\left(\mathbf{s}\right)}$
1	300	0.5	50	15	500	1200
2	350	0.5	50	15	500	1200
3	400	0.5	50	15	500	1200

The results of these tests are summarized by Table 3.3, that confirms that the deposition rate increases with sputtering power.

Table 3.3: Results summary for the adhesion layer test

Wafer #	P_{Al} (W)	t_{dep} (s)	t_f (nm)	$r_{dep} ({nm} {min}^{-1})$
1	300	1200	83,74	4,19
2	350	1200	95,33	4,77
3	400	1200	109,36	5,47

To reduce the production times, all subsequent AIN depositions were carried out at 400 W, the maximum power that was considered safe to deliver to the Al cathode. The deposition rate with these reference conditions was determined to be approximately 5.5 nm min⁻¹. XRD measures were carried out to determine whether the thin film had grown with some crystalline order. The θ -2 θ measurement of the wafers showed no diffraction peaks associated with AIN. Considering that the thickness of these films was significantly higher than target ones, it was concluded that the AIN adhesion layer would not influence the XRD results for the AIN layers grown on top of Pt.

An adhesion layer's thickness was measured from the following deposition batch. The deposition parameters were the same as wafer # 1, save for the deposition time, set to 220 s, to achieve a goal thickness of 20 nm. The ellipsometry reported a thickness of 21.3 nm, which was deemed satisfactory. After the characterization of the Pt films deposited on these two batches of wafer (discussed in the following section), it was decided to reduce the thickness of the adhesion layer, to ensure that the quality of the bottom electrode was virtually uninfluenced by the adhesion layer. The new target thickness was set to 10 nm (deposition time of 105 s), and the following batch of adhesion showed an average thickness of 10.8 nm. After these results, the following adhesion layers were not characterized, as their efficacy had already been proven.

3.3 Sputtering power influence tests

The first deposition batch focused on determining the effect of the sputtering power on the Pt films. The deposition parameters are reported in Table 3.4. The adhesion layers used for this deposition were the first ones that were produced.

Table 3.4: Deposition parameters for the sputtering power test

Wafer #	$P_{Pt}\left(\mathbf{W}\right)$	P (Pa)	F_{Ar} (sccm)	T_{dep} (°C)	t_{dep} (s)
1	100	0.5	50	350	300
2	125	0.5	50	350	300
3	150	0.5	50	350	300

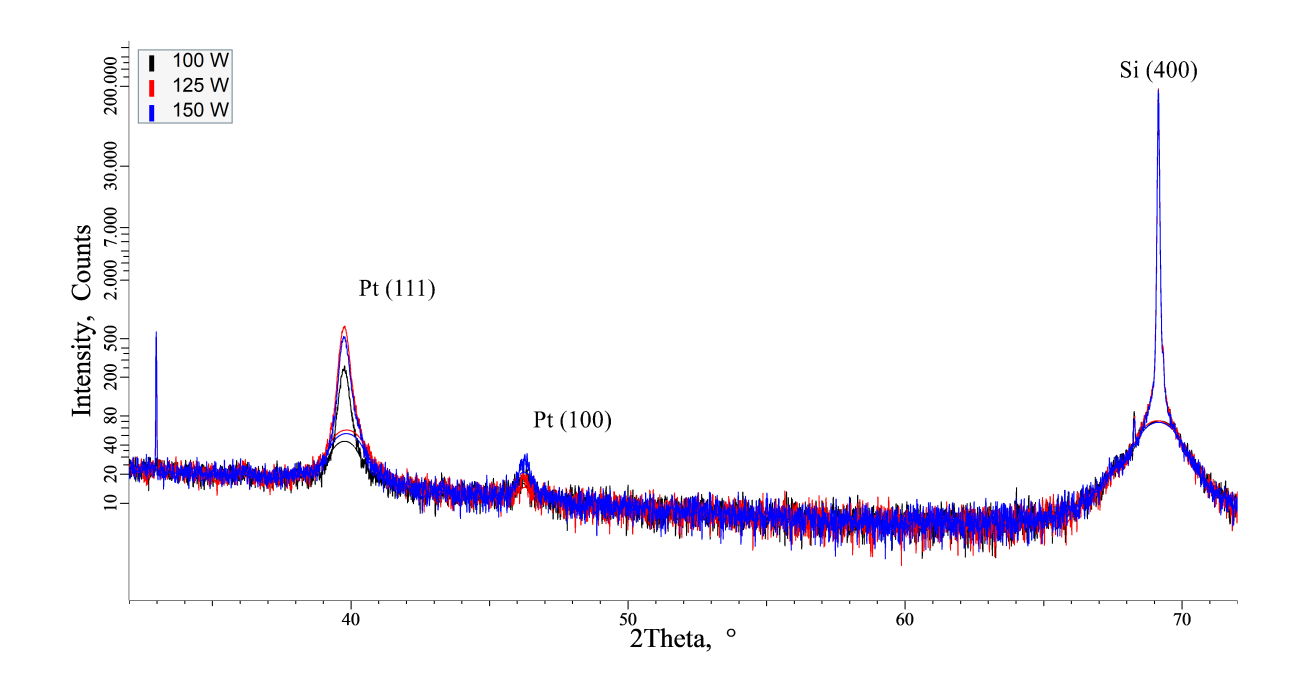


Figure 3.1: θ -2 θ scan for the sputtering power test.

The characterization of these films showed poor quality of the films. The XRD measures, reported in Figure 3.1, reveal very low diffraction peaks for the Pt (111) reflection, with an additional undesired peak for the (100) reflection. The average crystallite size was in the order of 29 nm. This shows that the nucleation of crystalline grains was very limited, and the film is prevalently amorphous. Sheet resistance measurements correlate with thickness measurements, as thicker films, obtained at higher sputtering powers, have lower sheet resistance values. However, the resistivity of the films is up to 65% higher than in the bulk counterpart (17.9· 10^{-6} Ω m vs 10.9· 10^{-6} Ω m), once again showing the poor quality of the obtained films.

The sputtering power was set to 125 W for the following depositions, as it showed the strongest Pt (111) reflection peak, and the deposition rate of around 9.7 nm min⁻¹ was deemed satisfactory. This is coherent with the results from Schmidl et al. [89] and Slavcheva et al. [90] that report a decrease in the Pt (111) intensity by increasing excessively the sputtering power.

The following batch of wafers were deposited on thinner adhesion layers, as described in the previous section, with the deposition parameters reported in Table 3.5. This batch was used to confirm that 125 W would be a suitable sputtering power for Pt deposition. The deposition pressure and the Ar flow were also slightly changed to determine whether one of the two parameters had a more substantial influence on the Pt films. While the resistivity of the film was still 53% higher than the bulk one, the crystallinity improved, with the absence of the Pt (100) peak and higher intensity for the Pt (111) reflection. The average crystallite size was similar to the previous depositions, with an average of 30 nm. The θ -2 θ scans are reported in Figure 3.2. The average stress decreased, from an average of 640 MPa in the previous set of wafers to an average of 412 MPa. The surface roughness of the films was also measured, resulting in an average R_q of 1.1 nm. The Pt film deposited at the highest pressure and flow (0.5 Pa and 50 sccm) showed the overall best properties.

Table 3.5: Deposition parameters for the second test batch

Wafer #	$P_{Pt}\left(\mathbf{W}\right)$	P (Pa)	F_{Ar} (sccm)	T_{dep} (°C)	t_{dep} (s)
1	125	0.4	50	350	300
2	125	0.5	40	350	300
3	125	0.5	50	350	300

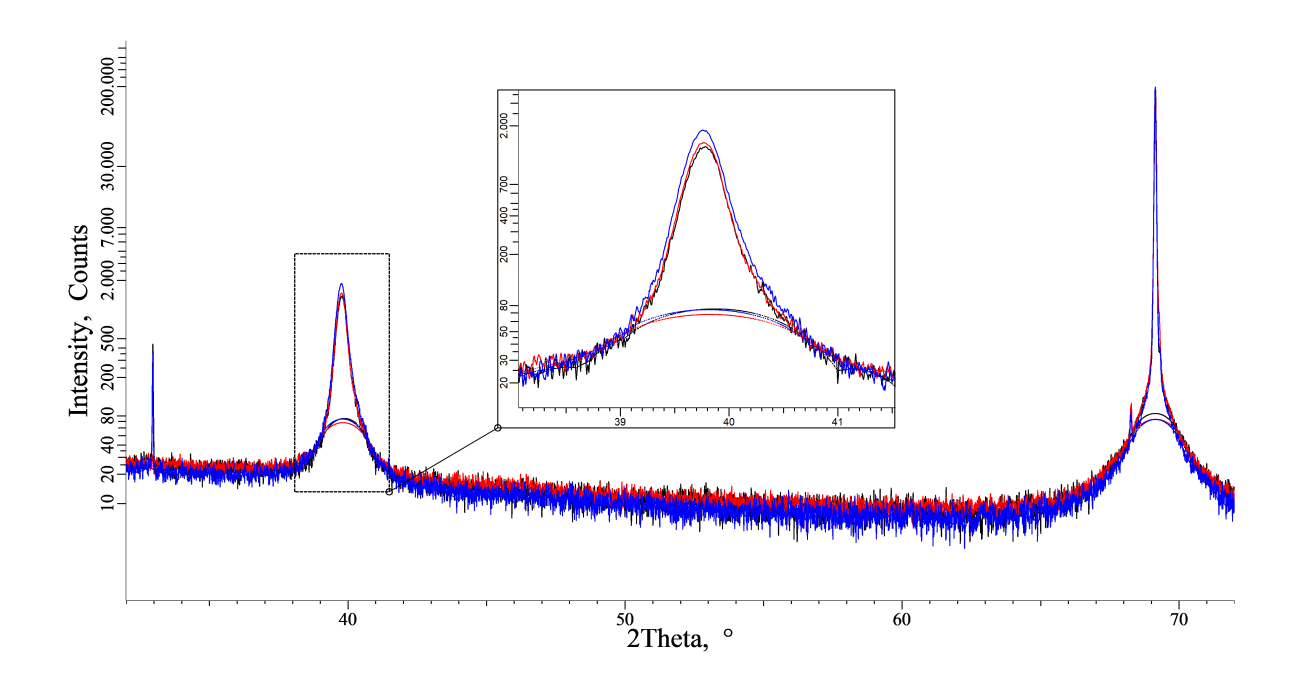


Figure 3.2: θ -2 θ scan for the second test batch, with a magnification of the Pt (111) peak.

Considering these results, three actions were taken to continue the optimization process:

- 1. Reducing the thickness of the adhesion layer from 20 nm to 10 nm, as all the films deposited in the second batch showed better crystalline properties than the previous one.
- 2. Increasing the deposition temperature to 500°C, to promote the nucleation of crystallites in the film [91].
- 3. Varying the pressure in a wider range of values, as it was reported by Schmidl [89] as the most influential parameter on crystallinity.

3.4 Process pressure influence test

The deposition parameters are reported in Table 3.6. The films produced in this test proved to be significantly improved compared to the previous runs. In the first place, the resistivity of the films decreased significantly, reaching a value only 10% higher than bulk. The stress increased again to values around 600 MPa, and the roughness values remained in the order of 1.0 nm. XRR measures reported films thickness varying significantly with the deposition pressure, while still being on average slightly higher than the previous batch. The θ -2 θ scans (Figure 3.3) showed significantly stronger Pt (111) peaks, with narrower FWHM, resulting in an average crystallite size of 45 nm, 50% larger than previously measured. All these results confirmed that more crystalline grains nucleated and grew larger. The intensity of the peak increases with the amount of crystalline phase. The resistivity decreases as grain size growth as the density of grain borders decreases. The stress increases as the crystals grains grow due to the lattice mismatch with the adhesion layer.

Table 3.6: Deposition parameters for the pressure test

Wafer #	$P_{Pt}\left(\mathbf{W}\right)$	P (Pa)	F_{Ar} (sccm)	T_{dep} (°C)	t_{dep} (s)
1	125	0.8	50	500	300
2	125	1.6	50	500	300
3	125	2.4	50	500	300
4	125	3.2	50	500	300
5	125	4.0	50	500	300
6	125	4.8	50	500	300

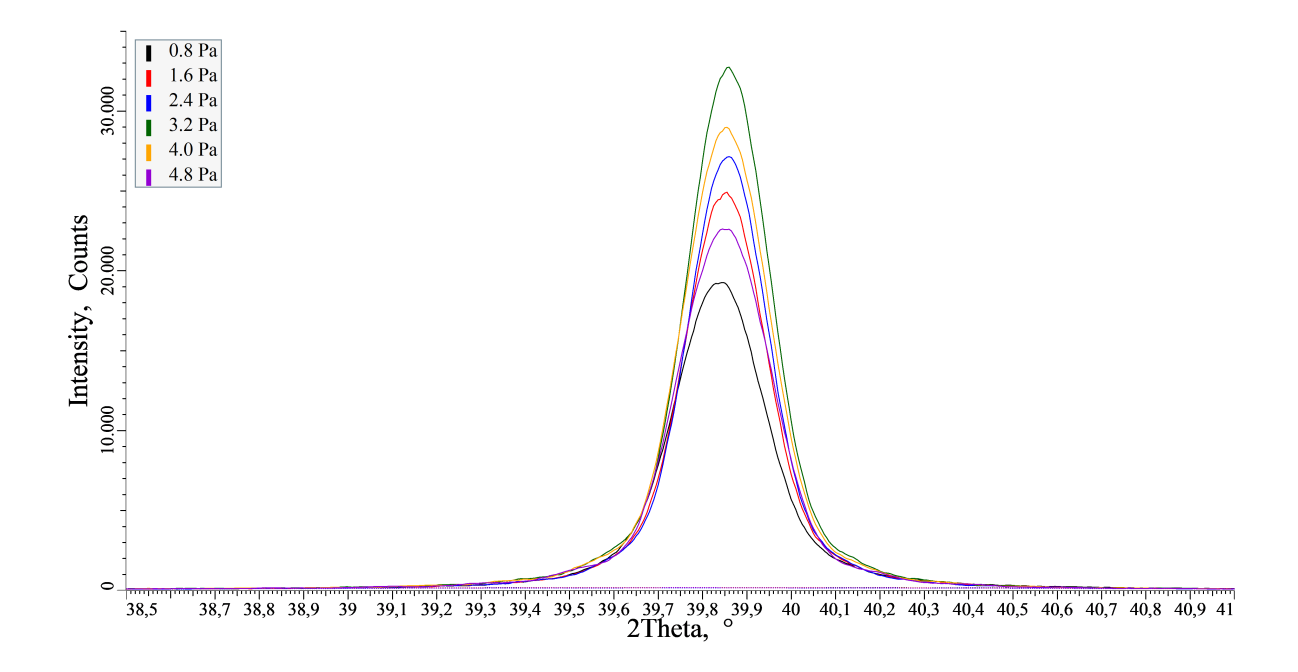


Figure 3.3: θ -2 θ scan of the Pt(111) peaks fo the films deposited in the pressure test.

Correlating the properties of the film and the deposition pressure, these trends can be observed:

- Peak intensity of Pt(111), crystallite size and deposition rate grow to a maximum and then decrease with the pressure (Figure 3.3, 3.4a, 3.4b).
- Resistivity decreases by raising pressure, stabilizing to a value around $12.0 \cdot 10^{-8} \Omega m$ (Figure 3.4c).
- Roughness is poorly influenced by pressure (Figure 3.4d).
- Stress values show a more complex behavior, initially decreasing with higher pressure, but the last film (4.8 Pa) shows a higher stress than the previous (Figure 3.4e).

All results are summarized in Table 3.7. The deposition rate behavior is easily explained by the initial increase of sputtering yield due to higher plasma density, that then lowers as the plasma becomes too resistive. Peak intensity and crystallite size behaviors have a similar explanation, as the sputtered particles initially arrive on the substrate with more energy as the pressure increases, but then when the plasma becomes too dense the mean free path of the sputtered particles reduces and they hit the substrate with lower energy. The energy of the impinging particles is fundamental to ensure mobility and crystallization, and hence the crystallinity is depended on the deposition pressure. Rising the substrate temperature is also an effective way to provide more energy to the substrate, further increasing the crystallinity. In light of these results, the optimal deposition pressure was determined to be 3.2 Pa, and the deposition parameters were considered optimized.

Table 3.7: Summary of results from the pressure deposition test

P (Pa)	t_f (nm)	r_{dep} (nm min $^-1$)	ρ_e (10 ⁻⁷ Ω m)	θ _B Pt (°)	β (°)	τ (nm)
0.8	51.47 ± 0.14	10.29 ± 0.03	1.27 ± 0.01	39.845	0.239	42.8
1.6	54.76 ± 0.12	10.95 ± 0.02	1.24 ± 0.01	39.855	0.219	46.7
2.4	54.32 ± 0.17	10.86 ± 0.03	1.22 ± 0.01	39.86	0.214	47.8
3.2	51.4 ± 0.16	10.28 ± 0.03	1.21 ± 0.01	39.86	0.220	46.4
4.0	47.68 ± 0.11	9.54 ± 0.02	1.20 ± 0.01	39.855	0.231	44.4
4.8	42.87 ± 0.03	8.57 ± 0.01	1.20 ± 0.01	39.845	0.247	41.5

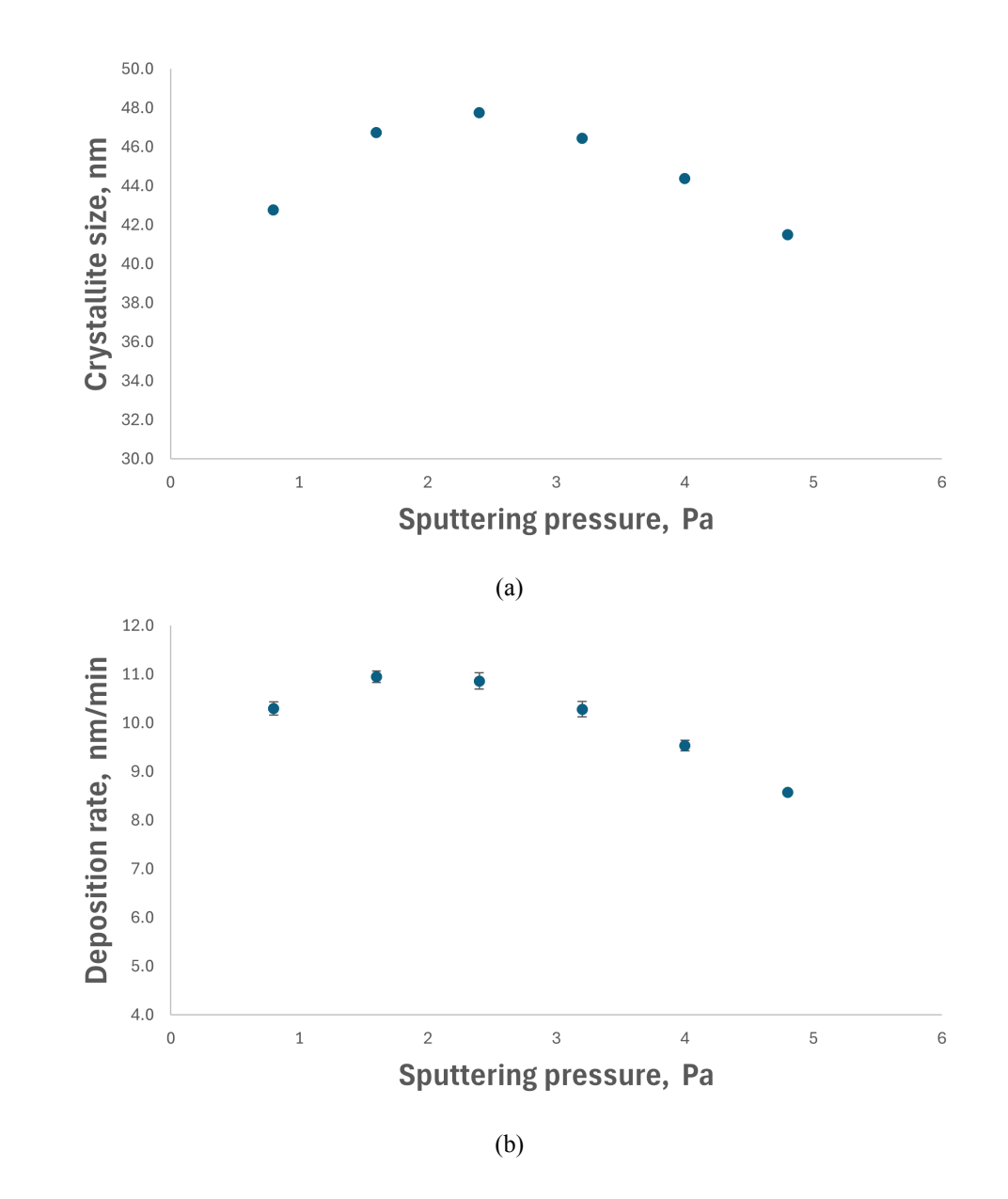


Figure 3.4: Influence of deposition pressure on average crystallite size (a), deposition rate (b).

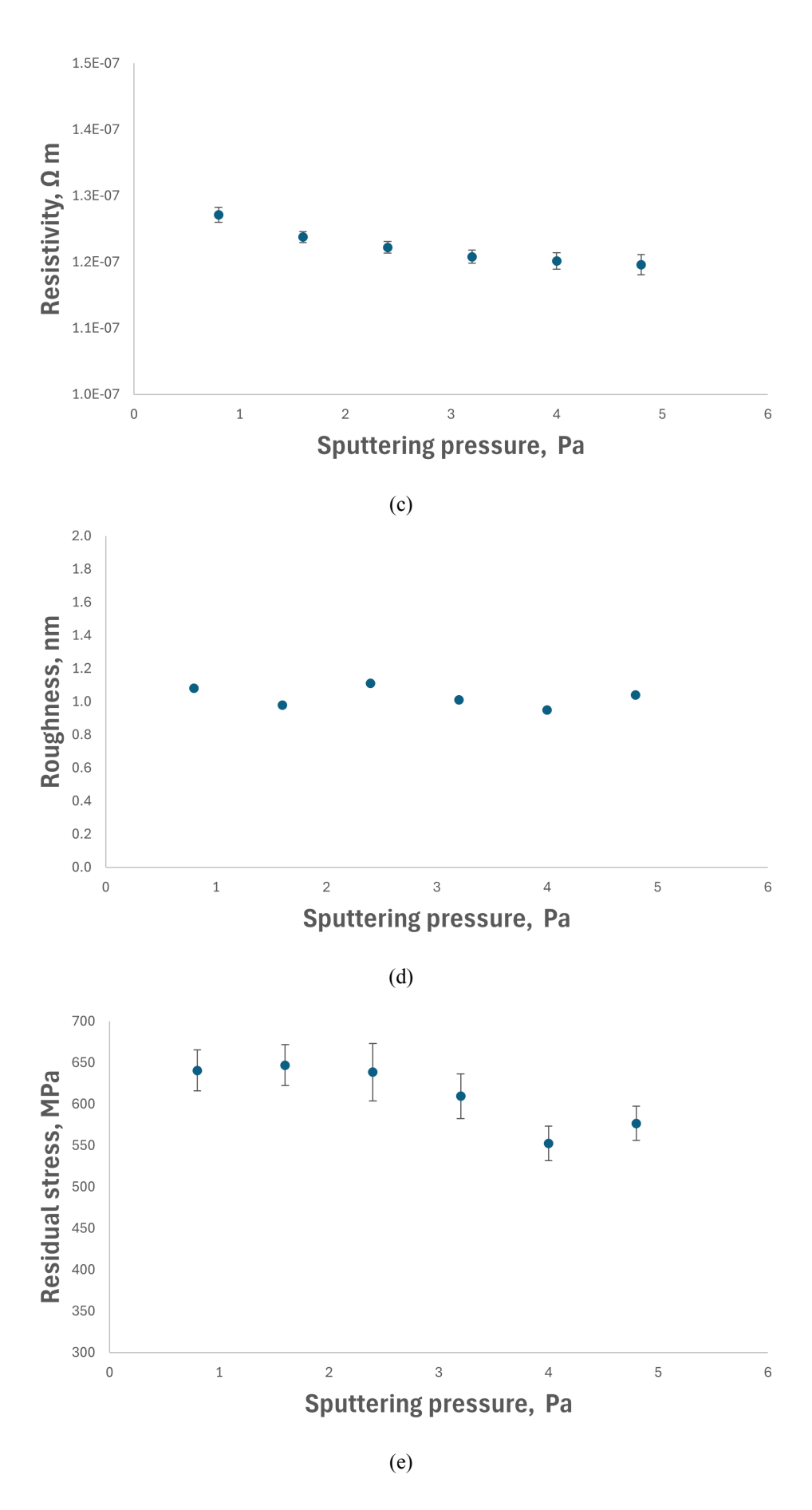


Figure 3.4: (continued) Influence of deposition pressure on resistivity (c), roughness (d) and average residual stress (e).

3.5 Optimized recipe tests and chamber contamination

After obtaining a clear set of deposition parameters, a recipe was developed to streamline the production of bottom electrodes to use for the AIN deposition test. The recipe combined the deposition of the adhesion layer and of the bottom electrodes, and two batches of three wafers were tested. In an attempt to reduce the process duration, the heating time in PM 2 was set to 5 minutes instead of 15. Thickness, resistivity and stress of these Pt films were consistent with the test deposition at 3.2 Pa. Roughness was not measured as it appeared consistent in all of the previous depositions. The crystallographic properties were instead different. While first film of each batch had an intensity comparable to the one obtained in the pressure test, the following two films showed a noticeably smaller peak, as can be seen in Figure 3.5. The rest of the film's properties, including average crystallite size, were consistent with the results, as reported in Table 3.8. The immediate hypothesis for this behavior was that the heating time in PM 2 had not been sufficient, and the chamber had actually cooled too much due to the insertion and extraction of wafers. To test this hypothesis other thin films were deposited with a complete heating time of 15 minutes in PM 2.

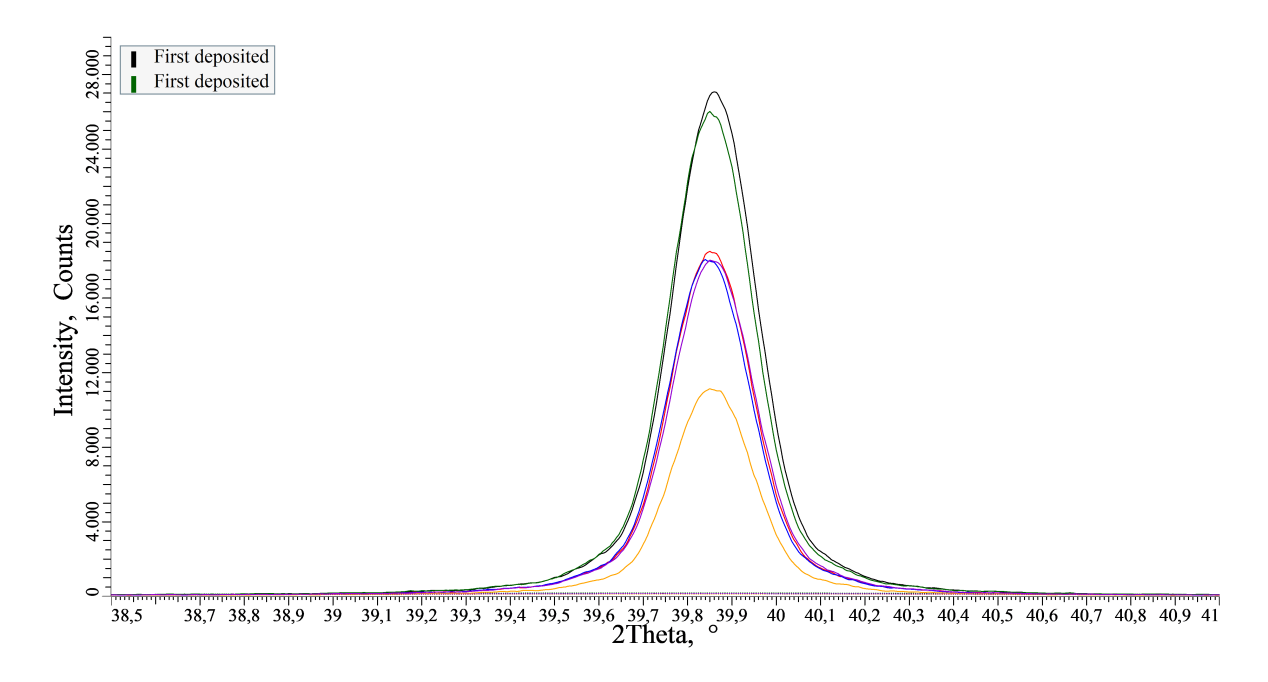


Figure 3.5: θ -2 θ scan of the Pt(111) peaks of the two batches of films deposited with the combined recipe for adhesion layer and bottom electrode.

Film ρ_e (10⁻⁷ Ω m) β(°) t_f (nm) r_{dep} (nm min θ_B Pt (°) τ (nm) 1 51.60 ± 0.31 10.32 ± 0.06 1.23 ± 0.01 39.860 0.222 46.1 2 51.42 ± 0.42 10.28 ± 0.08 1.22 ± 0.02 39.850 0.219 46.8 3 51.47 ± 0.46 10.29 ± 0.09 1.22 ± 0.02 39.845 0.220 46.4 4 51.61 ± 0.32 10.32 ± 0.06 1.23 ± 0.02 39.850 0.222 46.2 5 51.57 ± 0.46 10.31 ± 0.09 1.22 ± 0.02 0.216 47.5 39.850 6 51.48 ± 0.39 39.850 0.220 46.5 10.30 ± 0.08 1.22 ± 0.02

Table 3.8: Results summary for the combined recipe result

The results of these depositions were even worse: while all the other properties remained coherent between depositions, the intensity of the Pt(111) peak decreased abruptly, as shown in Figure ??. An additional test, whose results are included in the Figure mentioned above, was carried out to test it was the combined recipe to yield a poorly crystalline film, by testing the combined recipe against the two

separate recipes. The results of this test also had small Pt(111) peaks. The problem were caused by the other target available in the PM2, nominally SiO₂ and TiO₂. After the pressure test several long lasting deposition test (up to 24h) were conducted in PM2, depositing large quantities of oxides on the walls of the chambers. These oxides deposits were identified as the cause of the poor crystalline properties of the films, as once they were removed, the results returned to be coherent with the pressure test results (Figure 3.6). The mechanism with which the oxides deposits damaged the crystallinity of the Pt films is supposed to be linked with pressure regulation. The oxides depositions test were carried out at room temperatures, while all the Pt depositions at high temperatures. This caused the deposits to out gas a lot of trapped gas or byproducts, which troubled the pressurization of the chamber. Several depositions were severely delayed by the machine as the PM 2 would struggle to reach the base pressure due to the presence of these deposits. As shown before, pressure is a very influential parameter on crystalline properties of the sputtered film, and if the chamber had another source of gas during the depositions, it is reasonable to assume that it was the cause of the poor quality of the films.

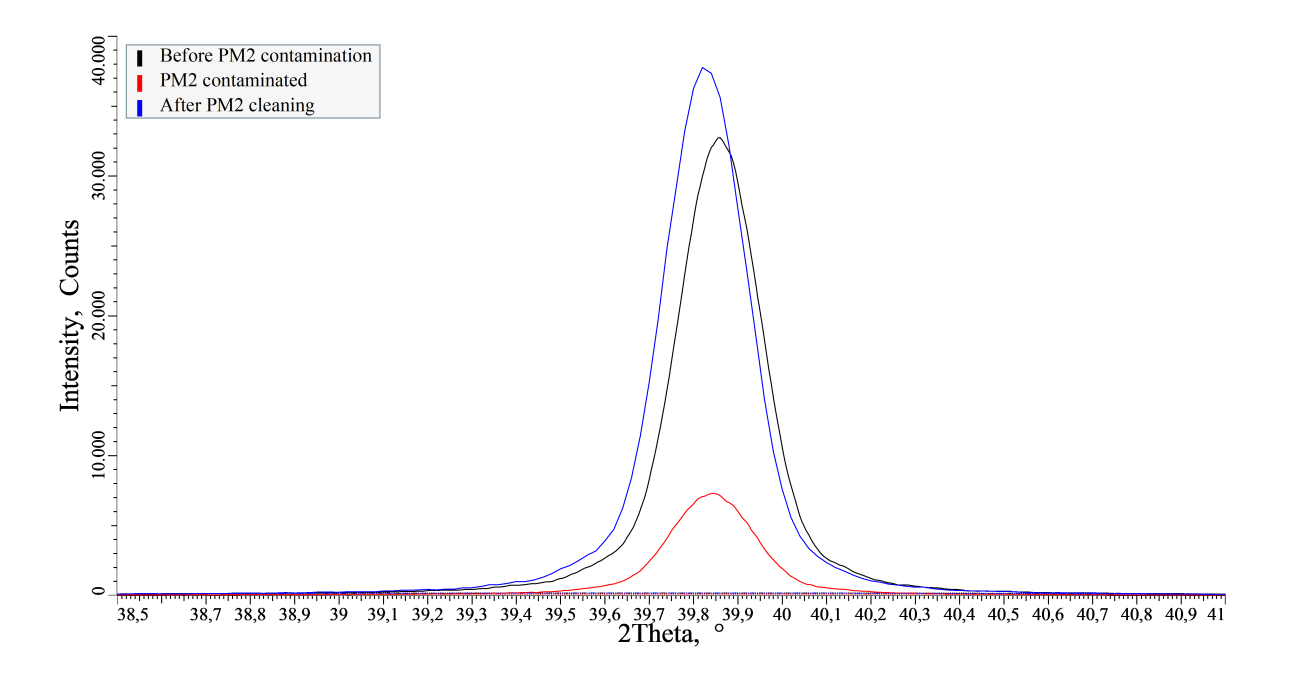


Figure 3.6: θ -2 θ scans of the Pt(111) peaks of film deposited before PM2 contamination, with PM2 contaminated and after PM2 cleaning.

The final optimized recipe for the deposition of Pt electrode was then set with the parameters reported in Table 3.9.

Table 3.9: Optimized parameters for Pt sputtering.

$P_{Pt}(W)$	P (Pa)	F_{Ar} (sccm)	T_{dep} (°C)	t_{dep} (s)
125	3.2	50	500	295

3.6 Spider600 bottom electrodes

To continue the experiments on AlN depositions other bottom electrodes were deposited with the Spider600. The deposition of Pt had already been optimized with this tool [33], so a standard recipe for 25 nm of Pt on 10 nm of Ti was employed, with the exception of one films that had a target thickness of 50 nm, to be confront it with the CT200 films. XRR measures indicated film thickness around 40 nm, in good accordance with the target. Sheet resistance measures reported film with higher resistivity, also due to their reduced thickness, and a lower level of uniformity in the film, as the standard deviation of

 R_{sh} measures was about ten times higher than for the films produced in the CT200. Crystallographic measures show films with a good degree of crystallization and orientation. Crystallites are smaller, with an average value of 27 nm. In Table 3.10 is reported the confront between the 50 nm Pt film deposited with the Spider600 and the films obtained with the optimized recipe in the CT200.

Table 3.10: Confront between 50 nm Pt electrodes deposited with different sputtering tools

Tool	R_{sh} (Ω/sq)	T_f (MPa)	θ _B Pt (°)	τ (nm)
CT200	$2.35{\pm}0.01$	610±27	39.860	46.4
Spider600	2.89 ± 0.13	327 ± 14	39.760	39.1

4. Piezoelectric layer deposition

4.1 Reference setting and preliminary depositions

Once the bottom electrodes were developed, the deposition of the AIN piezoelectric layer deposition was addressed. As discussed in Chapter 1, several deposition parameters can be tuned to modify the properties of the thin films. It was necessary to select few depositions parameters for two main reasons: to comply with the tool operational limits and to contain the time needed for experiments, as the deposition rate of AlN in the CT200 is pretty low, averaging just over 5 nm min $^{-1}$. The main tool's limits considered were the maximum power deliverable to the targets, nominally 400 W for Al, the maximum N₂ flow deliverable to PM6, 25 sccm, and the temperature limit of 500°C to move the wafers from a chamber to another. This last factor was not in itself a limit of the tool, but it substantially increased the process time, already aggravated by 15 minutes of thermal stabilization time. The low deposition rate comported that to reach the target thickness of 400 nm the sputtering process should have run for at least 75 minutes per each deposition. The sputtering power was already address in the adhesion layer deposition tests, and it was set to the maximum value to not decrease the deposition rate. The process temperature was set to 500°C not only to comply with the tool programming, but two other reasons: better film properties were reported with deposition temperatures up to 500°C [27, 30], and this temperature is compatible with Complementary Metal-Oxide-Semiconductor (CMOS) production processes. Deposition pressure was chosen as one of the deposition parameters because it showed the most impact on Pt properties and it was a way to exploit the potentiality of CT200 to decouple the control of the gas flow and the processing pressure. The second selected deposition parameter was the application of a RF bias to the substrate, which is used to improve the growth orientation of the thin film along the c-direction [30]. The effect of the N₂ ratio in the gas flux was the last parameter to be analyzed, as it can greatly influence the quality of the grown films, with the possible downside of reducing the deposition rate [23, 26].

Two preliminary AlN depositions were done to be set as references for the following depositions. The first deposition was done following the recipe developed by CMi engineers to ensure that the Al cathode is fully poisoned before deposition, with the only modification being the sputtering power for Al raised to 400 W to maximize the deposition rate. The parameters are reported in Table 4.1. The first deposition was run for 3600 s, to control that the deposition rate remained consistent over longer depositions. Ellipsometry measures revealed that the average thickness of the film was 341.9 nm, resulting in a deposition rate of 5.7 nm min⁻¹, coherent with previous results. The uniformity of the film was also assessed at a standard deviation of 3.6 nm and a maximum thickness variation of 4.1% of the average thickness. The film was also significantly more stressed than the Pt films deposited before, with an average stress of 874±22 MPa. The XRD measures showed that the AlN film did crystallize in the desired direction showing only the (002) reflection peak, with an average crystallite size of 47 nm (Figure 4.1), confirming the effectiveness of the bottom electrodes as growth layers for AlN. The rocking curve measures showed also a level of grain orientation, with a FWHM of 5.83°. The most concerning results however were some macroscopic defects visible in the films, which were then investigated with electron microscopy. In Figure 4.2 is possible to see the morphology of one of these defects, whose sizes range from 3 µm to 30 µm. Analyzing the composition of the films with EDX, the presence of iron was revealed, suggesting that the defects are most likely inclusions of particles produced by the deposition chamber or the substrate holder.

Table 4.1: Basic recipe for the deposition of AlN in CT200

Al sputtering Power	Substrate Power	Pressure	Ar flux	N ₂ flux	Temperature
400 W	0 W	0.5 Pa	50 sccm	15 sccm	500 °C

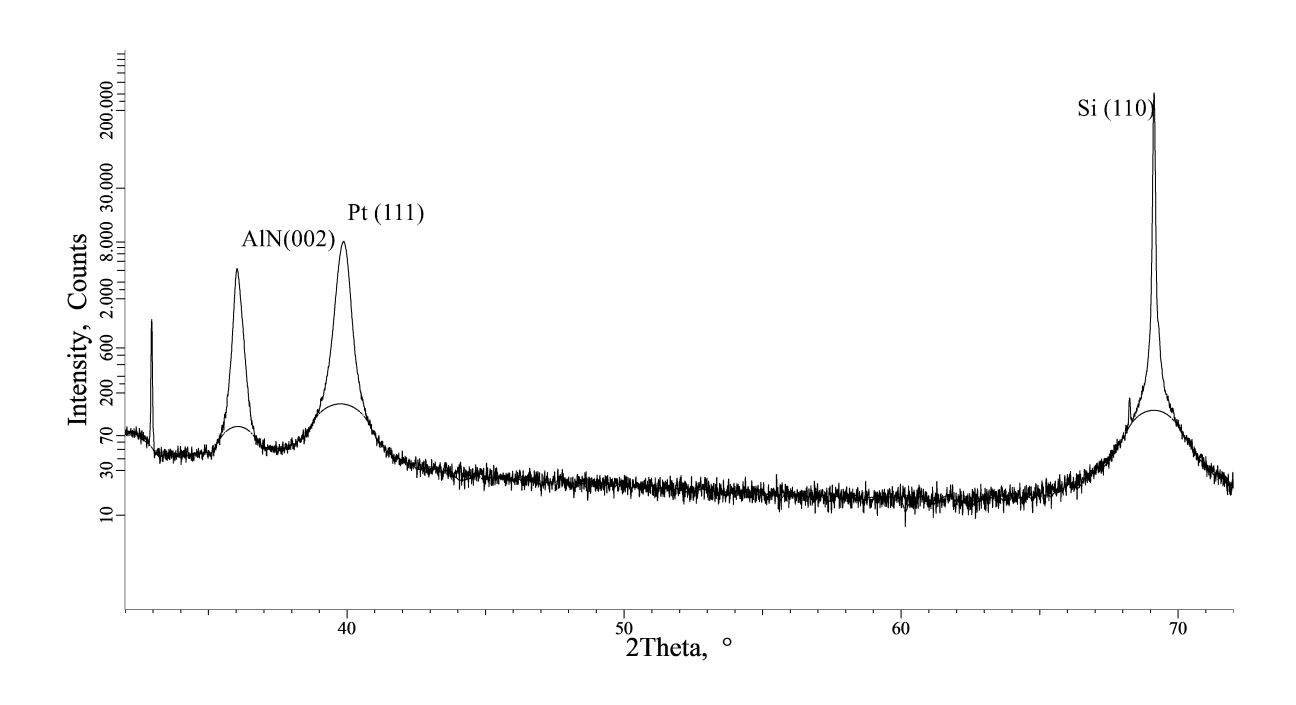


Figure 4.1: θ -2 θ scan of the first AlN film deposited, with peaks indexed.

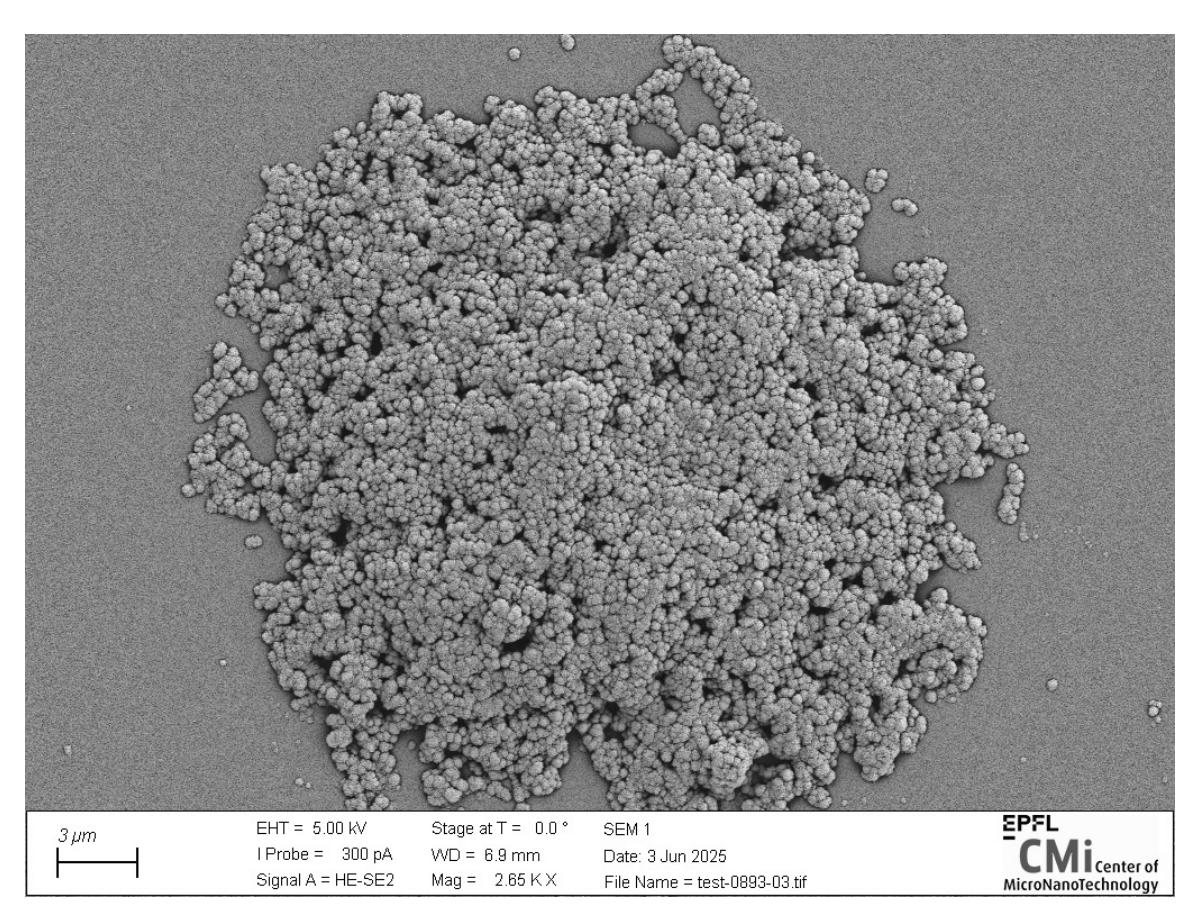


Figure 4.2: SEM image of a defect in the first AlN film deposited.

To rule out the substrate holder as the cause of the contamination, another deposition was run using a different substrate holder and following the same recipe as before, only increasing the deposition time to 4500 s, to meet the target thickness of 400 nm. This film still showed some macroscopic defects, but

in smaller numbers and the EDX analysis didn't show any iron contamination, proving that the problem was caused by a substrate holder that had deflaked during sputtering. The substrate holder responsible was sanded down by CMi staff and an additional maintenance break solved the problem, as all the following films deposited had no macroscopic defects. This film also showed a slightly improved thickness uniformity, as ellipsometry measures reported a thickness of 408.7 ± 0.9 nm, with a maximum variation of 0.72%. As the thickness goal for the film was reached, all the following deposition time were set to 4500 s. At the same time the average stress decreased to 437 ± 10 MPa, and the XRD measures reported a higher intensity for the AlN(002) peak, and an average crystallite size of 64 nm (Figure 4.3). The growth orientation was also higher, as the FWHM of the rocking curve decreased to 3.33° . A final deposition proved that the film contained no inclusions, and the first deposition parameter was tested, the deposition pressure.

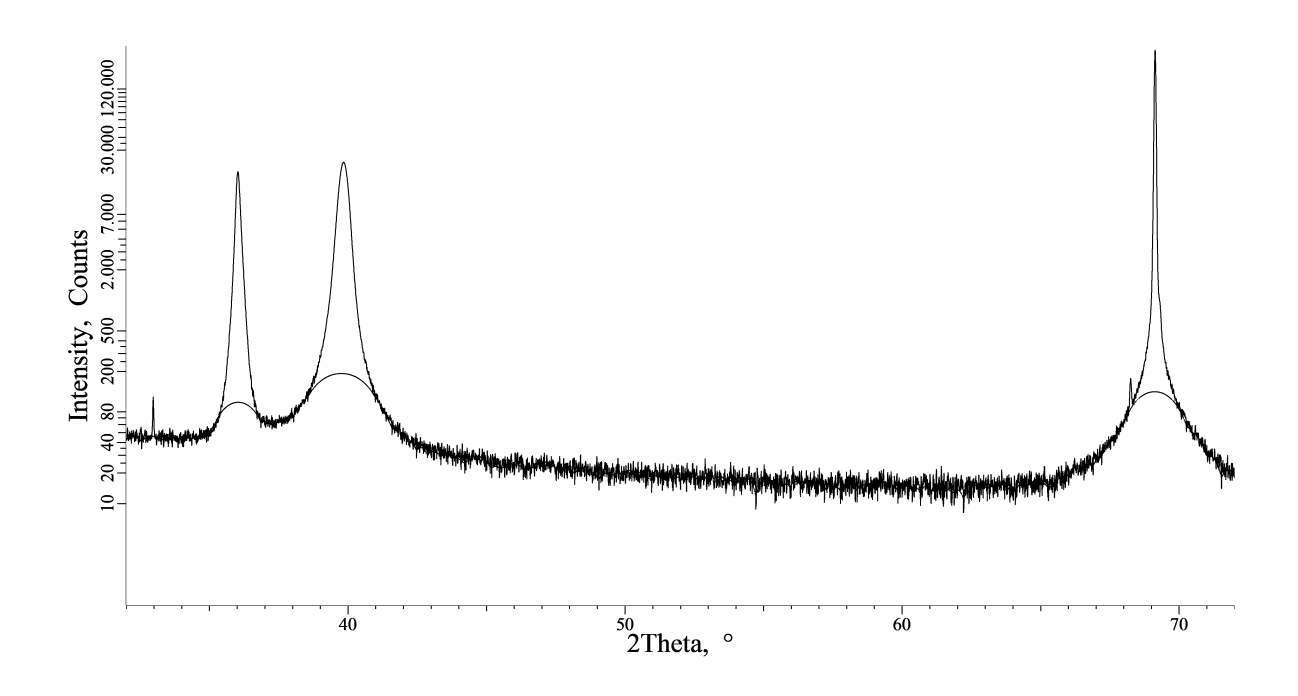


Figure 4.3: θ -2 θ scan of the second AlN film deposited.

4.2 Depositions pressure test

To test the influence of the process pressure on the AlN films, five films were deposited, with pressures ranging from 0.5 Pa (the first film without inclusions from the preliminary depositions) to 2.5 Pa. The results of these depositions are summarized in Table 4.2. The thickness of the films decreases linearly with pressure, reducing the deposition rate to half of the first value at the maximum pressure (Figure 4.4). XRD measures reveals that the intensity of the AlN(002) peak drops drastically, possibly affected by the reduced thickness, to the point where the peak is basically absent, revealing a completely amorphous film, as shown in Figure 4.5. The average crystallite size also decreases with increasing pressure, and is of course null at the maximum pressure 4.6. Also the orientation of the films decrease significantly, as the FWHM of the rocking curve grows from 3.09 ° to 5.84 ° up to 1.5 Pa, after which the rocking curve is not detectable, showing no orientation of the few crystalline grains if presents. Thickness uniformity behaves less predictably, with standard deviations ranging from 0.5 nm to 3.3 nm and maximum thickness variation reaching a maximum of 5.4%. The average stress of the films decreases significantly, even becoming compressive at the maximum deposition pressure, as shown in Figure 4.7. This can be explained by the combined effect of reduced crystallinity and reduced thickness of the film.

Table 4.2: Summary of results from the pressure deposition test

P (Pa)	t_f (nm)	r_{dep} (nm min $^{-1}$)	Δt_f	θ_B AlN (°)	τ (nm)	rc FWHM (°)	T _{av} (MPa)
0.5	$410.4{\pm}2.3$	5.47	3.3%	36.030	67	3.09	479±11
1.0	348.4 ± 0.5	4.64	0.5%	36.005	53	4.92	260 ± 7
1.5	286.9 ± 2.2	3.83	2.7%	35.995	49	5.84	93 ± 8
2.0	229.0 ± 3.2	3.05	5.4%	35.995	39	-	87 ± 9
2.5	197.0 ± 2.4	2.63	5.0 %	-	-	-	-77±7

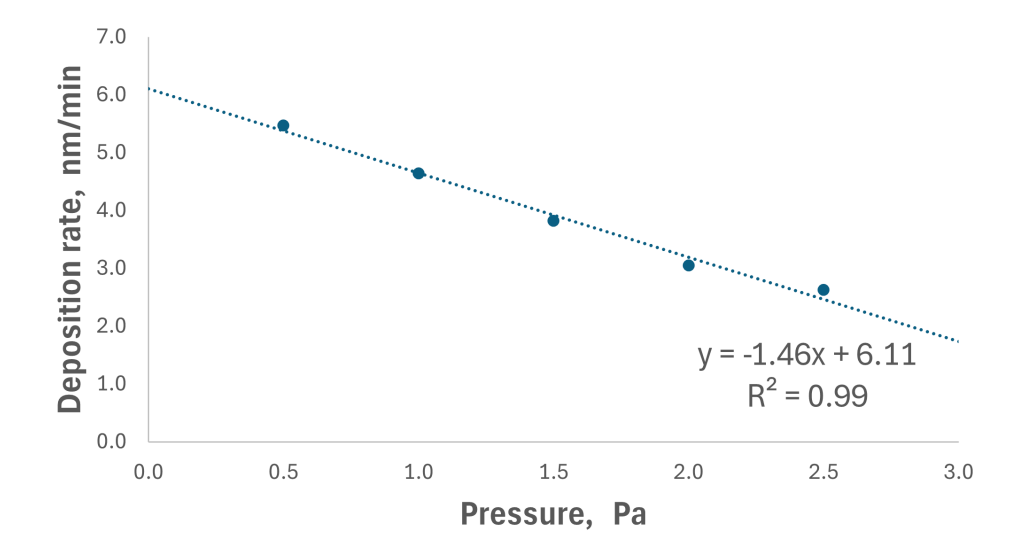


Figure 4.4: Effect of pressure deposition on deposition rate of AlN. Linear fit with corresponding \mathbb{R}^2 included.

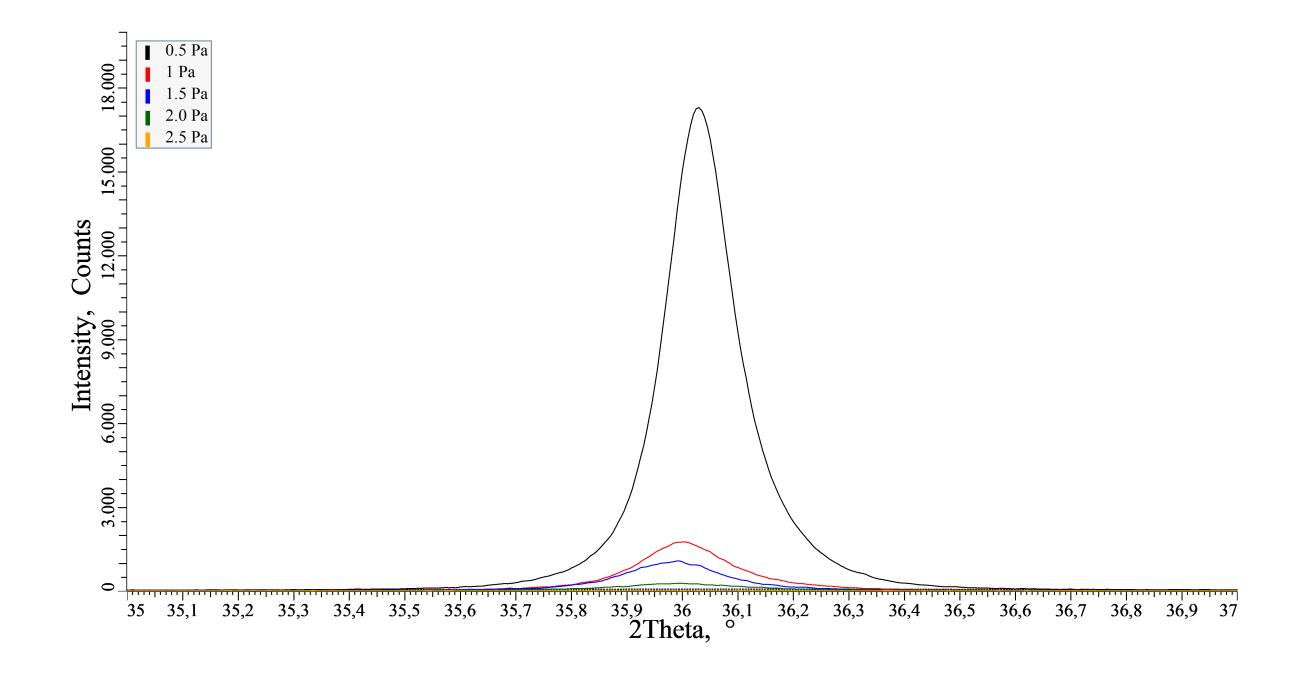


Figure 4.5: θ -2 θ scans for AlN(002) peaks of the film deposited at varying pressures.

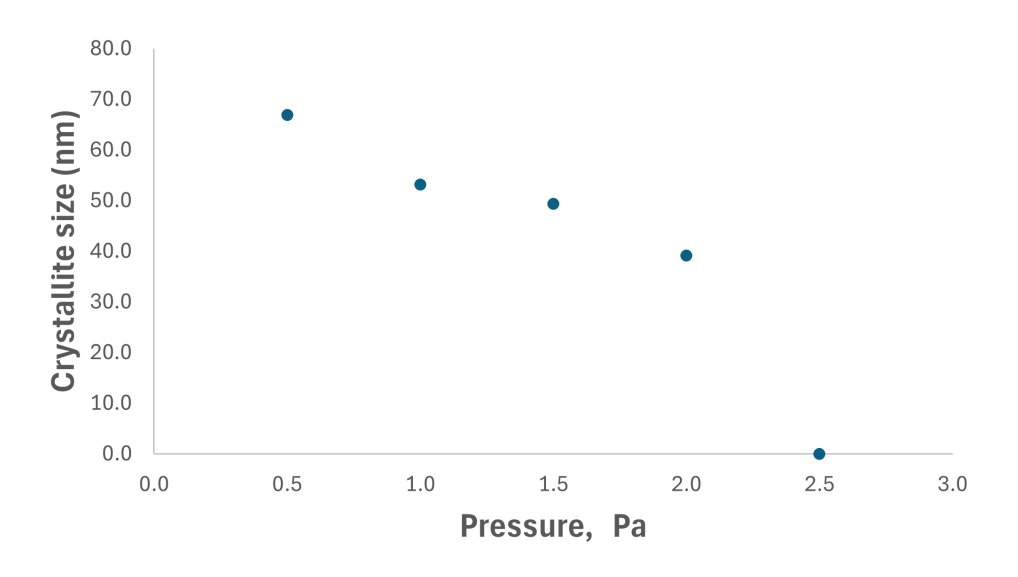


Figure 4.6: Effect of pressure deposition on average crystallite size of AlN.

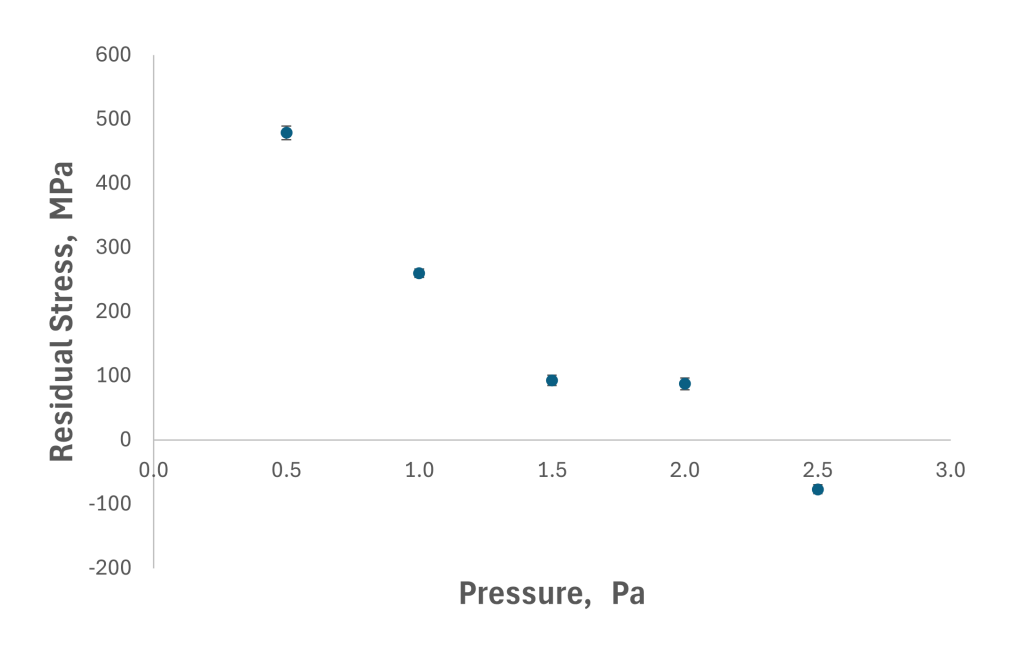


Figure 4.7: Effect of pressure deposition on average stress of AlN films.

Considering these results, it is clear that raising deposition pressure over 0.5 Pa strongly degrades the the properties of the thin films. It was then decided to test lower deposition pressures. The tool however could not regulate properly the pressure below 0.5 Pa with a total gas flux of 65 sccm. After a failed deposition at 0.3 Pa with the same deposition parameters, the pressure for the next deposition test was set to 0.5 Pa in order to maintain the same total gas flux and N_2 -to-total flux ratio. A successive deposition, done after the test on the substrate bias application revealed that the tool could maintain a deposition pressure of 0.4 Pa with a total gas flux of 65 sccm. The results of this deposition were significantly better than the previous depositions, with a slightly higher deposition rate $(5.8 \text{ nm min}^{-1})$ instead of 5.5 nm min^{-1}), lower stress $(394\pm5 \text{ MPa}$ rather than $479\pm11 \text{ MPa})$, slightly smaller crystallite size (59 nm vs 67 nm) and a significantly more oriented crystalline growth, with a rocking curve FWHM of 2.29° . However, due to the difficulty of the tool to maintain a deposition pressure below 0.5 Pa and having obtained better results with the application of a substrate bias, the value for the deposition pressure was still set to 0.5 Pa for the final recipe.

4.3 Substrate bias test

The application of a RF bias was not straightforward in the CT200. The tool would struggle to activate the substrate generator and would often detect plasma instability and interrupt the process. To solve this issues, a step was added to the deposition process to activate the substrate generator in the most suitable condition to keep it stable at lower power. This procedure required the intervention of CMi staff to change the deposition parameters for each process, so only four values of power delivered to the substrate (P_{sub}) were set: 0 W, 5 W, 10 W and 20 W. The resulting bias on the substrate were 20 V, 55 V, 86 V and 131 V. The rest of the process parameters were kept the same as the base recipe (Table 4.1). Ellipsometry measures showed that film thickness was not significantly affected by the substrate bias: the films deposited with a substrate bias were only about 10 nm thinner than the film deposited without it. Thickness uniformity was also pretty consistent, with a maximum thickness variation of about 1.75% in the film deposited at 5 W. However, XRD measures revealed that the bias greatly influenced the crystallinity of the films, as shown in Figure 4.8. The film deposited at P_{sub} = 5 W showed a great improvement of crystalline properties. The AIN (002) peak FWHM indicated an average crystallite size of 106 nm, and the rocking curve FWHM of 1.75° showed a good degree of orientation of the grains. The film deposited at P_{sub} = 10 W instead showed a significantly less strong AlN (002) peak, shifted to slightly smaller angles (35.78° rather than 35.97°) with a smaller average crystallite size of 47 nm, and a wider rocking curve FWHM at 4.41°. Finally at P_{sub} = 20 W the film did not crystallize at all, not showing any diffraction peak related to AlN. The average stress also changed significantly: the film deposited at 0W and 5W had a tensile residual stress, higher in the film deposited with a bias, while the film deposited at higher substrate powers had a compressive residual stress, higher in absolute value for the highest bias applied. This behavior can be explained considering the role that the substrate bias plays in the deposition and growth of the films and is also reported in literature [23, 30]. The substrate bias is used to provide more energy to the sputtered particles arriving on the substrate: providing more energy increases the mobility of adatoms on the surface of the forming film, assisting the growth of the crystalline grains. Over a certain value however the particles impinge on the surface of the film with too much energy, reducing the crystalline growth. If the bias is increased even further, the substrate is actually sputtered, as the impinging particles remove matter from it. When the bias is too high to promote the crystalline growth of the film, it actually densifies it, creating compressive stress. The results are summarized in Table 4.3.

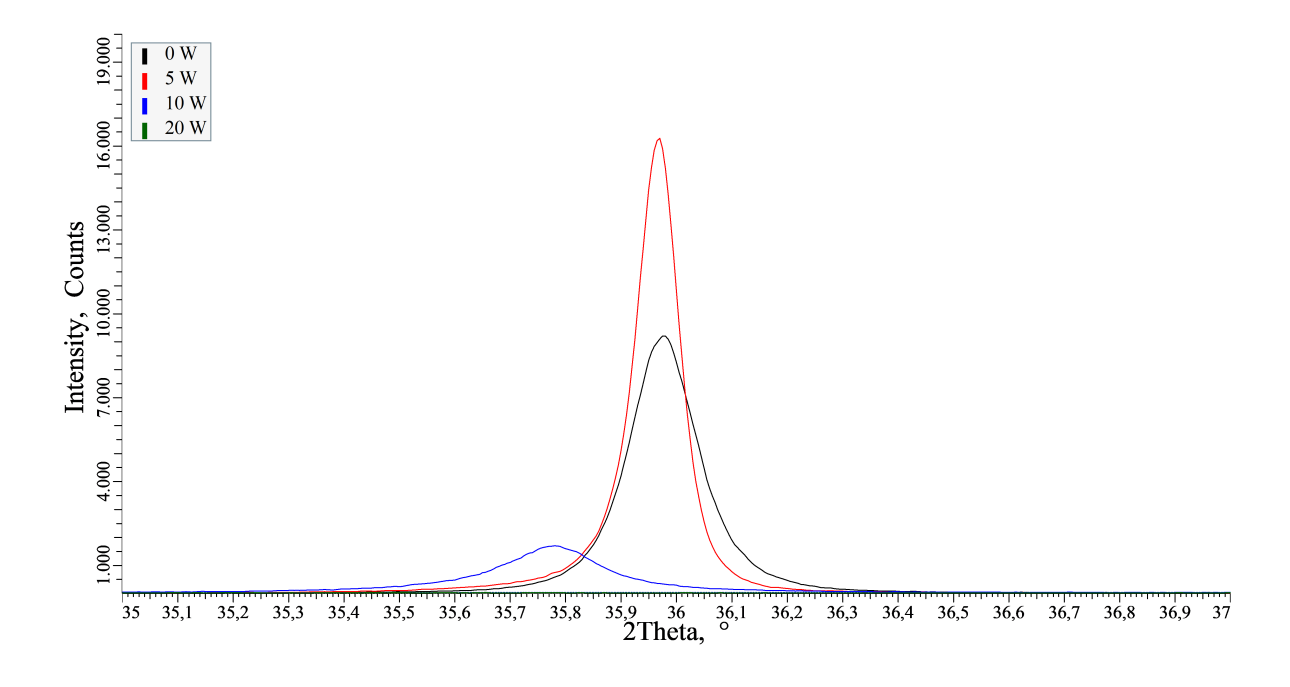


Figure 4.8: θ -2 θ scans of the AlN(002) peaks of the films deposited on the bias test.

Table 4.3: Summary of results from the bias deposition test

$P_{sub}\left(\mathrm{W} ight)$	t_f (nm)	r_{dep} (nm min $^{-1}$)	Δt_f	θ_B AlN (°)	τ (nm)	rc FWHM (°)	T _{av} (MPa)
0	412.1 ± 0.8	5.49	0.7%	35.975	68	1.89	532±7
5	399.3 ± 1.9	5.32	1.8%	35.970	106	1.75	613±5
10	393.1 ± 0.2	5.24	0.2%	35.780	47	4.41	-217 ± 1
20	399.3 ± 1.2	5.32	1.2%	-	-	-	-386 ± 4

The properties of the film deposited without an applied bias need to be addressed too. They are coherent with the previous depositions, except for significantly smaller rocking curve FWHM, as can be seen in the Figure 4.9. This discrepancy can be explained by considering the residual stress in the Pt layers before the deposition. The pressure test was conducted using Pt layers deposited by CT200, which all showed a tensile residual stress of around 600 MPa. The substrate bias test instead was conducted using Pt film produced by Spider600, which are consistent with the ones deposited by CT200, except for the first one, which a small unnoticed variation in the deposition parameters caused it to have a significant compressive residual stress of -764±38 MPa. The compressive state of the growth layer is hypothesized to be the cause for the better orientation of the film, but this effect was not further explored, as the Pt films produced by CT200 never showed a compressive residual stress, and in the moment the PM2 was still producing Pt films with poor crystallinity properties. As discussed in however the effect of the optimal substrate bias on a tensile bottom electrode proved to be still more impactful on grain orientation than the use of a compressively-stressed Pt layer. The value of 5W for the substrate power generator was set for the final recipe. In the following test a substrate bias was not used as the deposition parameters had to be changed significantly.

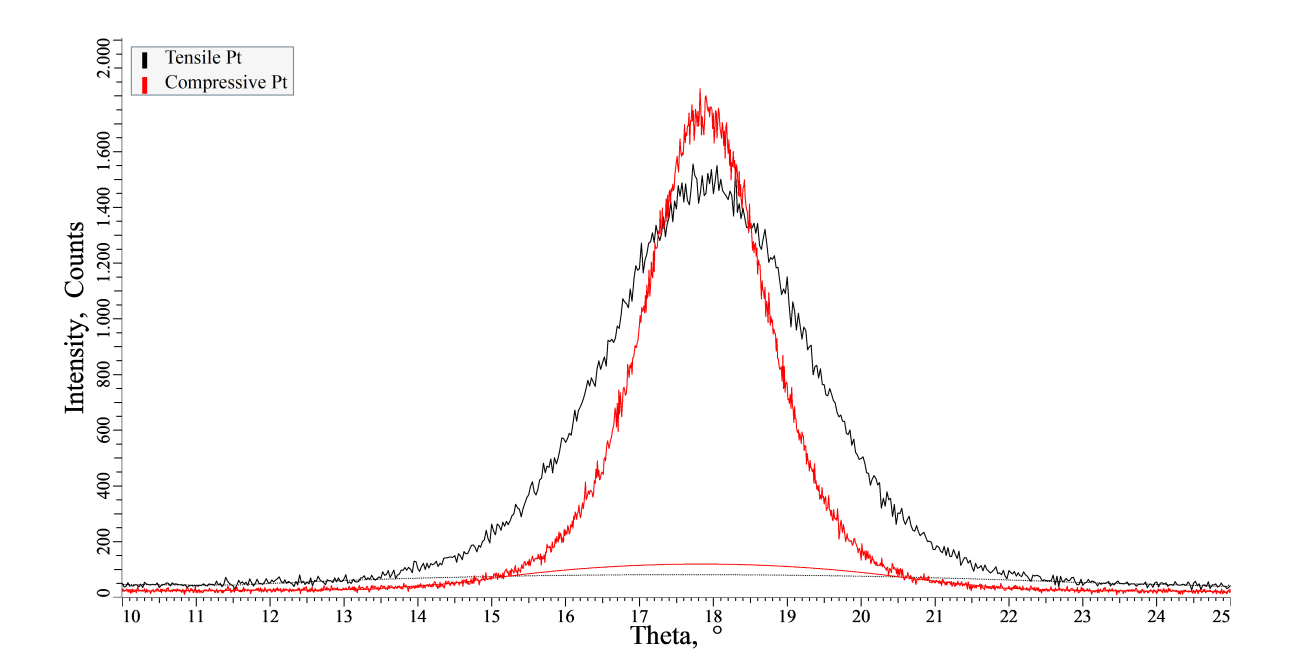


Figure 4.9: Confront of the rocking curve for AlN films deposited on tensile and compressive stressed Pt electrodes.

4.4 Gas ratio test

To test the influence of the ratio of N₂ flux to the total gas flux, a preliminary deposition was conducted. The gas flux was comprised entirely of Nitrogen, and to ensure that the tool could successfully complete the deposition with a gas flux significantly lower (25 sccm), the deposition pressure was lowered to 0.3 Pa. The rest of the process parameters were kept the same as the base recipe (Table 4.1). The main goal for this deposition was to observe the resulting crystalline orientation of the film. As the deposition pressure was lowered and the gas was entirely comprised of N₂, the deposition rate was expected to significantly decrease. Ellipsometry measures confirmed this, resulting in a film thickness of 261.6±1.4 nm and a deposition rate of 3.5 nm min⁻¹, 36% lower than the reference value of 5,5 nm min⁻¹. The film was significantly stressed, with a residual stress of 777±8 MPa. The XRD measures however indicated good crystalline qualities of the film, with and average crystallites size of 86 nm and a rocking curve FWHM of 2.06°. With these results in mind, it was deemed worth to deposit films using a higher N₂ gas flux ratio. To accommodate the tool limitation and ensure that the pressure was regulated successfully, the F_{N2} was set to 20 sccm and the F_{Ar} value reduced accordingly. The N₂ ratio values (F_{N2} / F_{tot}) considered were 0.33, 0.50 and 0.67, to be compared with a previous deposition done at 0.23. The deposition parameters are reported in Table 4.4. It is important to note that the final deposition has a total gas flux of 30 sccm, which is the limit for which the tool is capable of maintaining a pressure of 0.5 in PM6 while sputtering AlN.

Table 4.4: Deposition parameters for the gas ratio test

F_{N2} (sccm)	F_{Ar} (sccm)	F _{tot} (sccm)	N ₂ ratio	P_{Al} (W)	P (Pa)	T_{dep}	t_{dep} (s)
20	40	60	0.33	400	0.5	500	4500
20	20	40	0.50	400	0.5	500	4500
20	10	30	0.67	400	0.5	500	4500
25	0	25	1.00	400	0.3	500	4500
15	50	65	0.23	400	0.5	500	4500

As it was observed in the previous deposition, reducing the total gas flow reduces the deposition rate. Plotting the deposition rate in function of the total gas flux, it can be observed that the correlation is not linear, probably due to the varying amount of N₂, as can be seen in Figure 4.10. Nitrogen has a lower sputtering yield than Argon [23], and that reduces the deposition rate. How influent was this effect compared the total gas flux variation is not clear, but was not investigated, for the sake of not further reducing the deposition rate of AlN. Stress measures indicated that the stress increases for both low and high values of the N_2 ratio, with a more pronounced effect for higher ratios (Figure 4.11a). θ -2 θ scans (Figure 4.12) showed that the AlN(002) peak with the highest counts was the one with the lowest N₂ ratio, while for N₂ ratios above 0.50 the peak intensity was very similar. However it is to be consider that the films showed different thicknesses, so it was possible that a lower signal could still be associated with a higher density of crystalline grains in the film. Crystallite size remained pretty constant with N₂ ratio, apart for the film deposited without Ar, that showed an average crystallite size 50 % larger and the film deposited at a N₂ ratio of 0.33, that showed a small decrease in crystallite size 4.11b. Rocking curve measures (Figure 4.13) however clearly show that higher N₂ ratios improve the orientation of the crystalline grains in the film: the FWHM reached a minimum of 2.03° for F_{N2} / F_{tot} = 0.67, only slightly better than the film deposited in pure N₂. The results of these depositions are reported in Table 4.5.

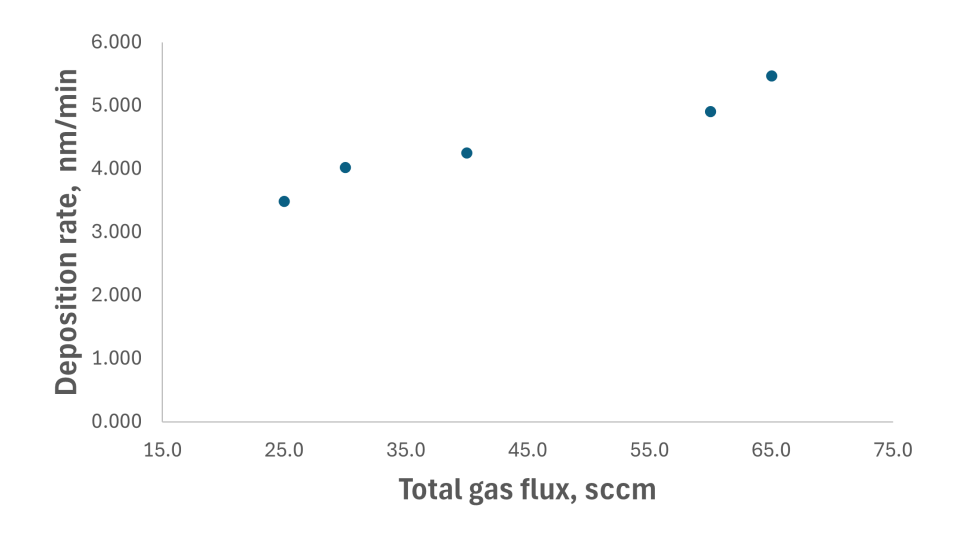


Figure 4.10: Effect of total gas flux on the deposition rate for the films deposited at different N_2 ratios.

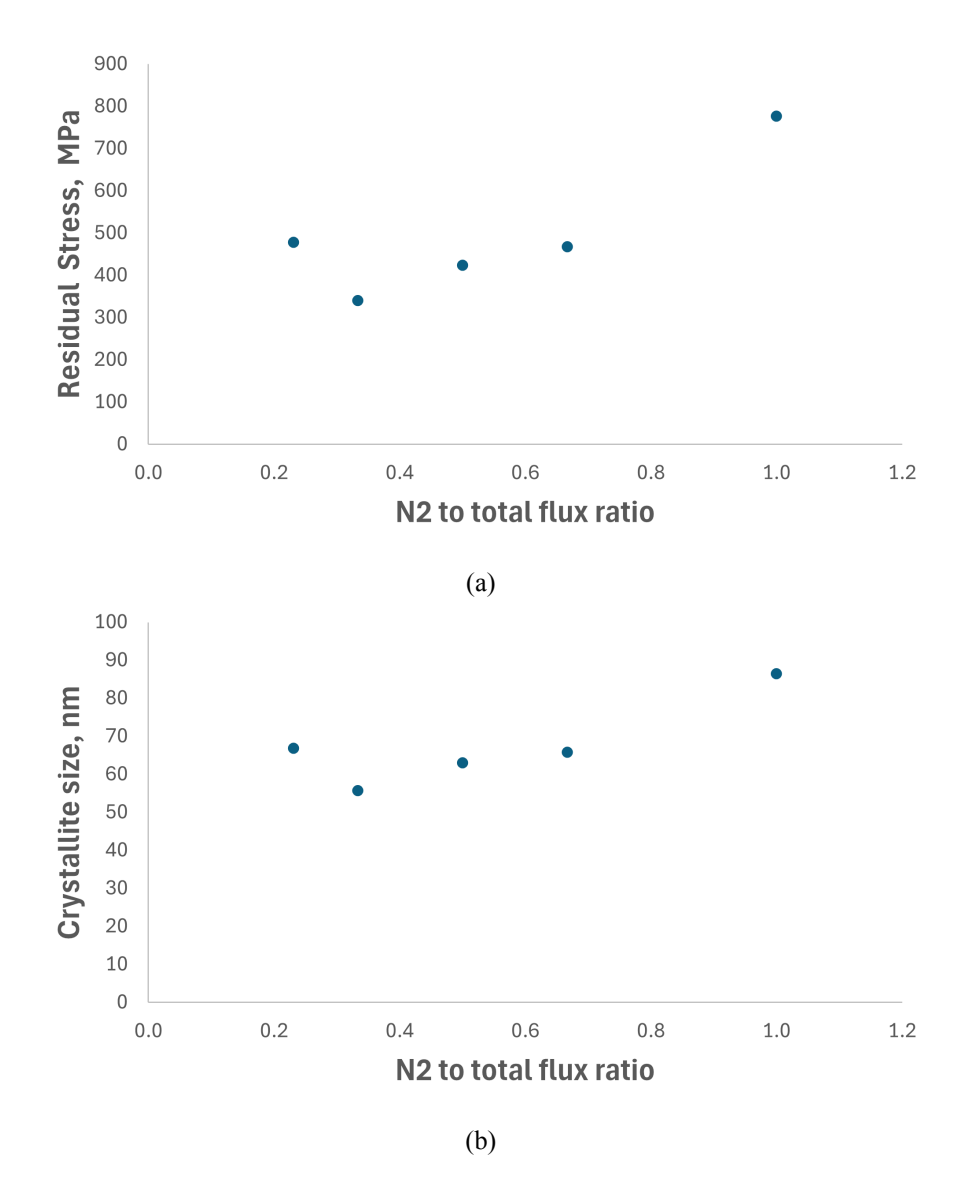


Figure 4.11: Effect of N_2 ratio on the residual stress of the films (a) and the crystallite size (b).

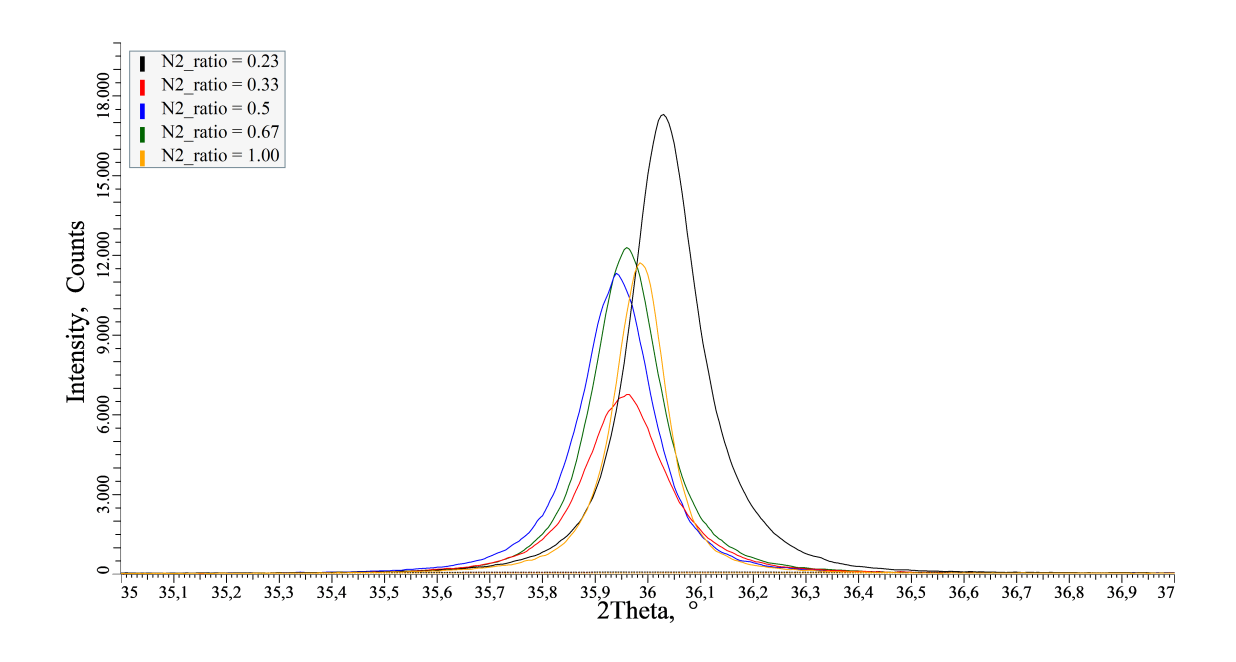


Figure 4.12: θ -2 θ scans of the AlN (002) peak for films deposited at different N_2 ratios.

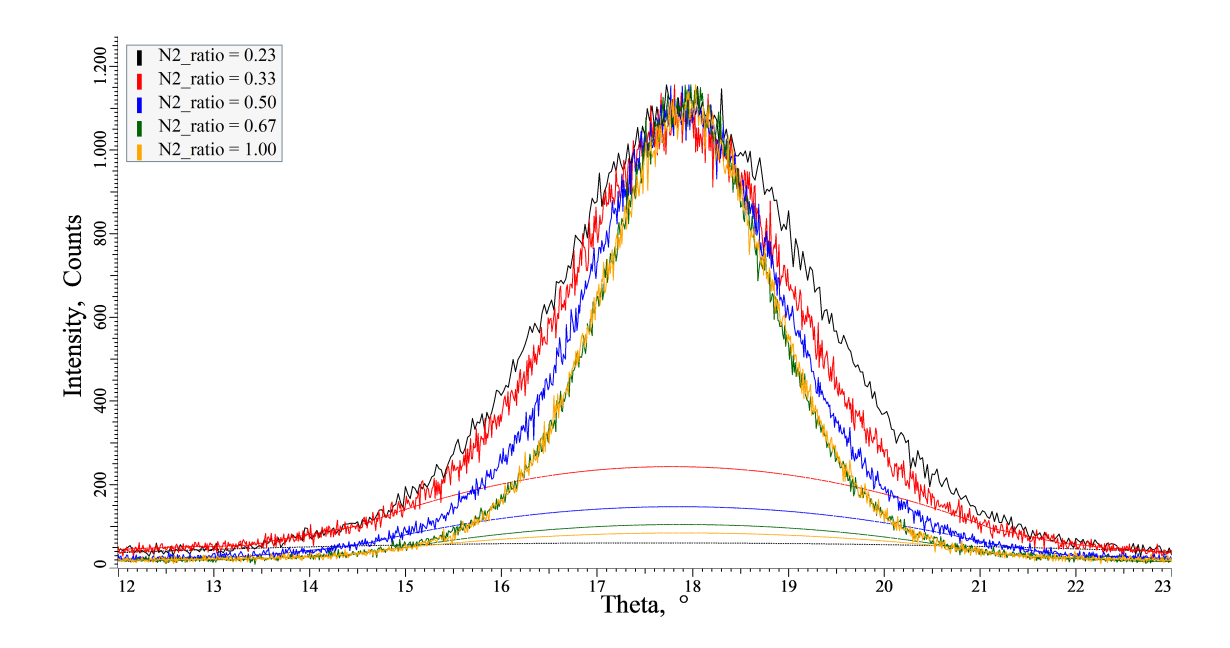


Figure 4.13: Rocking curves of the AlN (002) peak for films deposited at different N₂ ratios.

Table 4.5: Summary of results from the gas ratio deposition test

N ₂ ratio	t_f (nm)	$r_{dep}~({ m nm~min}^{-1})$	Δt_f	θ _B AlN (°)	τ (nm)	rc FWHM (°)	T _{av} (MPa)
0.23	410.38 ± 2.33	3.28%	5.47	36.030	67	3.09	479±11
0.33	368.09 ± 2.11	2.48%	4.91	35.960	56	2.69	341 ± 5
0.50	319.00 ± 0.68	0.87%	4.25	35.940	63	2.32	424 ± 5
0.67	301.81 ± 0.82	0.93%	4.02	35.960	66	2.03	468 ± 6
1.00	261.62 ± 1.38	1.62%	3.49	35.985	86	2.06	777 ± 8

These results proved that a higher concentration of N_2 in the processing gas do improve the orientation of crystalline grains in AlN films. However, due to the tool's limitations, a higher N_2 ratio could only be obtained lowering the Ar flux, so at the expense of an already low deposition rate. The substrate bias also proved to be more effective at orienting the crystalline grains and promote their growth. In light of these consideration, the final gas flux ratio was kept the same as the basic recipe (Table 4.1).

4.5 Optimized recipe and deposition on patterned electrode

In light of the information gathered with the previous test, an optimized recipe was defined. The goal of this recipe was to deposit AlN films that would be integrated in FBAR devices, to test their piezoelectric properties. The recipe optimization stopped at this point also because the CT200 tool underwent a month of maintenance, making it necessary to dedicate the remaining time to the characterization of the piezoelectric properties of the films. The first version of this optimized parameters are reported in Table 4.6

Table 4.6: Parameters for the first optimized recipe

P_{Al} (W)	$P_{sub}\left(\mathbf{W}\right)$	P (Pa)	F_{Ar} (sccm)	F_{N2} (sccm)	N ₂ ratio	T _{dep} (°C)	t_{dep} (s)
400	150	0.5	50	15	0.23	500	4500

However before starting the realization of FBAR, it was necessary to test whether the films would show different properties if deposited on a patterned bottom electrode. To do so a test film of AlN was deposited on a patterned bottom electrode, whose realization is discussed in Chapter 5. The properties of this film were consistent with the results of the previous tests, showing that the deposition on patterned metal did not influence the quality of the AlN film. Table 4.7 reports the confront between the two films.

Table 4.7: Confront of film properties between film deposited on patterned and non-patterned growth layers

Pt film	t_f (nm)	Δt_f	$r_{dep} ({nm} {min}^{-1})$	θ_B AlN (°)	τ (nm)	rc FWHM (°)	T _{av} (MPa)
Smooth	399.3±1.9	1.75%	5.32	35.970	106	1.75	613±5
Patterned	444.8 ± 6.3	4.25%	5.93	36.040	105	1.72	613 ± 8

The only evident discrepancy was the thickness of the films, which was 11 % higher than the previous result. This was motivated by the maintenance interventions that occurred, and a quick test deposition on a non patterned Pt layer confirmed that the deposition rate had slightly increased from 5.3 nm min⁻¹ to 5.9 nm min⁻¹ after the maintenance, and the effect was not limited to patterned electrodes. The thickness uniformity of the film was also slightly lower, as an obvious consequence of the patterning of the bottom electrode. The surface roughness of the film was also quickly assessed with an AFM measure, reported in Figure 4.14 and 4.15. The R_q measured was of 10.5 nm, with a surface characterized by small triangular shaped grains evenly distributed on the surface, with a characteristic size of about 100 nm, coherent with the XRD observations.

Considering the increase of the AlN deposition rate after maintenance, the deposition time was reduce to 4250 s, to obtain a goal thickness of 425 nm, slightly higher than the previous target to leave some room in case the deposition rate decreased again after some time. The piezoelectric layer and the top electrode are deposited in sequence without breaking the vacuum, so the only characterization possible for the AlN layer deposited this way is the analysis of the frequency response of the microdevices. Table 4.8 reports the deposition parameters used for the AlN films employed in the FBAR production.

Table 4.8: Parameters for the second optimized recipe, used for FBAR production

P_{Al} (W)	$P_{sub}\left(\mathbf{W}\right)$	P (Pa)	F_{Ar} (sccm)	F_{N2} (sccm)	N_2 ratio	T_{dep} (°C)	t_{dep} (s)
400	150	0.5	50	15	0.23	500	4250

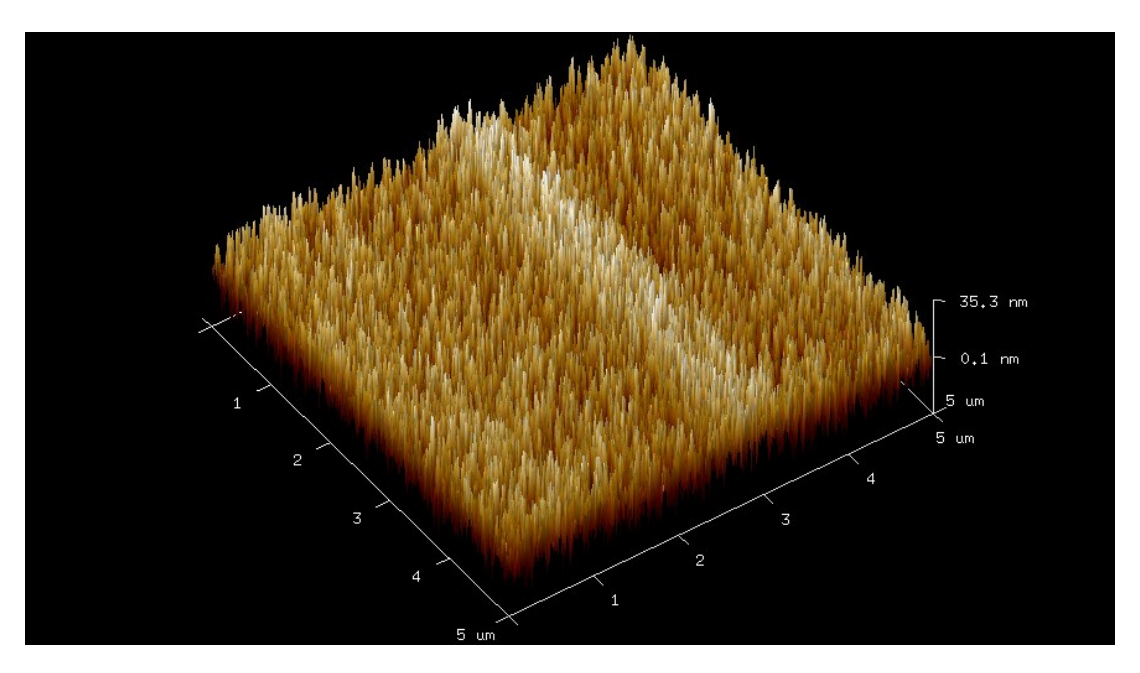


Figure 4.14: 3D visualization of AFM measures of the surface of the film deposited on patterned platinum

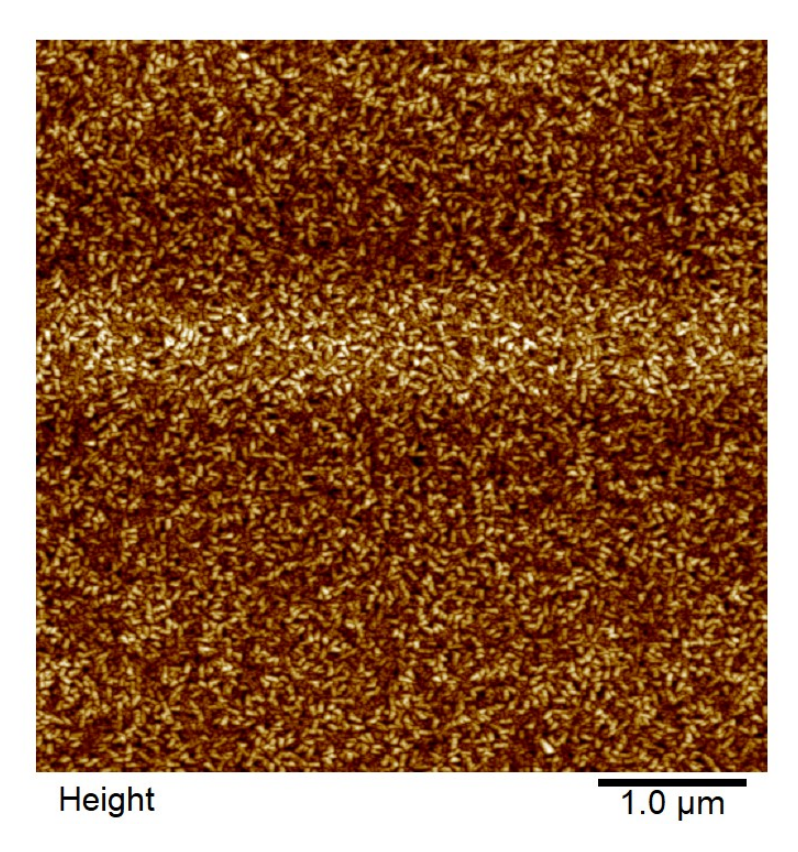


Figure 4.15: 2D visualization of AFM measures of the surface of the film deposited on patterned platinum

4.6 Sc alloying calibration test

Due to the limited time available with the CT200 tool and some setback in the development, the process optimization was limited to AlN films. This however meant that one of the main features of the film, the possibility to co-sputter different materials at once, was being left out. To make up for it, a brief investigation on the potentiality of the CT200 tool to deposit AlScN film with controlled Sc concentration. The films were deposited directly on top of p-doped Si wafers, in order to reduce the time needed for setup. As the main characteristic to be determined of these films was going to be the concentration and not their crystalline properties, the use of a different substrate was not an issue. To regulate the composition, the power provided to the Sc cathode P_{Sc} was varied. To have a first estimation on how to correlate the Sc sputtering power to the Sc concentration in the film, the data from Beaucejour [37] was used to create a linear regression, shown in Figure 4.16. As the source material used a different tool with targets capable of withstanding significantly higher sputtering power, the values fitted and used in the following discussion are the ratio of Sc atomic percentage to the sum of Sc and Al atomic percentage $(x_{Sc} = \%Sc/(\%Sc + \%Al))$ and the ratio of Sc sputtering power to total sputtering power $(r_{P,Sc} =$ $P_{Sc}/(P_{Al}+P_{Sc})$). While the maximum value of power deliverable to the Al target was 400 W, the Sc cathode could only tolerate sputtering power up to 300 W, due to a different mounting configuration. The N₂ gas flow was slightly increased to 20 sccm to ensure that the poisoning step was completed on both targets. The Ar flow was initially set to 50 sccm, but with a combined gas flux of 70 sccm and two cathodes being sputtered, the tool could not regulate properly the pressure to the set point of 0.5 Pa. Instead, the pressure inside PM 6 during the deposition was actually slightly higher, and the end of the sputtering step the tool was not able to reduce the pressure correctly, and the process was interrupted. To avoid this error from repeating, the Ar flux was set to 40 sccm. The deposition time was set to 1800 s, as there was not requirement on the film thickness to meet and the deposition rate was expected to be higher than the one used measured for AlN. The deposition were carried out with a deposition Temperature of 500°C, to remain coherent with the AlN depositions. No bias was applied on the substrate, as the crystallinity was not the main target for this procedure. The deposition parameters are reported in Table 4.9, together with the target Sc concentration set for each deposition.

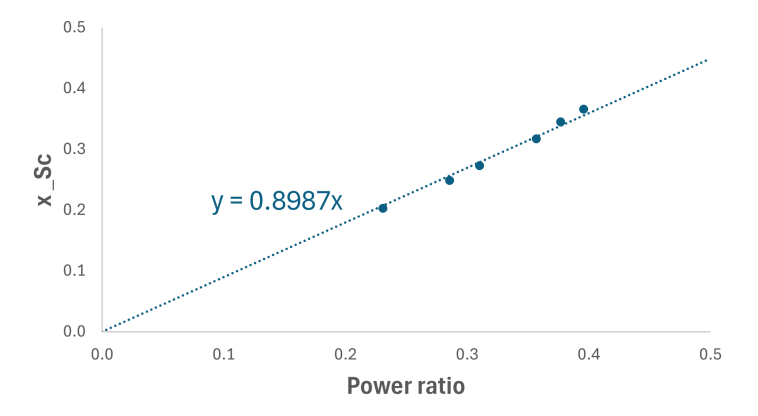


Figure 4.16: Linear fitting of the Sc concentration against the Sc sputtering power ratio from [37], used to determine the deposition parameters.

Table 4.9: Deposition parameters for the Sc concentration test

P_{Al} (W)	$P_{Sc}\left(\mathbf{W}\right)$	$r_{P,Sc}$	P (Pa)	F_{Ar} (sccm)	F_{N2} (sccm)	T_{dep} (°C)	t_{dep} (s)	target x_{Sc}
400	300	0.43	0.5	50	20	500	1800	0.385
400	200	0.33	0.5	40	20	500	1800	0.300
400	150	0.27	0.5	40	20	500	1800	0.245
400	100	0.20	0.5	40	20	500	1800	0.180
400	50	0.11	0.5	40	20	500	1800	0.100

The thickness and curvature radius of these films were measured before depositing 30 nm of Cr on top of the films to measure their composition with EDX. Ellipsometry measures revealed that the deposition rates increased significantly compared to those of pure AlN, thanks to the significantly higher total sputtering power considered. The dependency between deposition rate and total sputtering power is clearly linear, as shown in Figure 4.17. The deposition rate for the sputtering run at the highest total sputtering power (700 W) is slightly higher than the prediction, as it was the deposition for which the total gas flux was not compatible with the process pressure set. The residual stress decreased with growing total sputtering power, as showed in Figure 4.18. This trend can be explained by the different thicknesses of the films, but the influence of other parameters, such as crystallinity can not be ruled out.

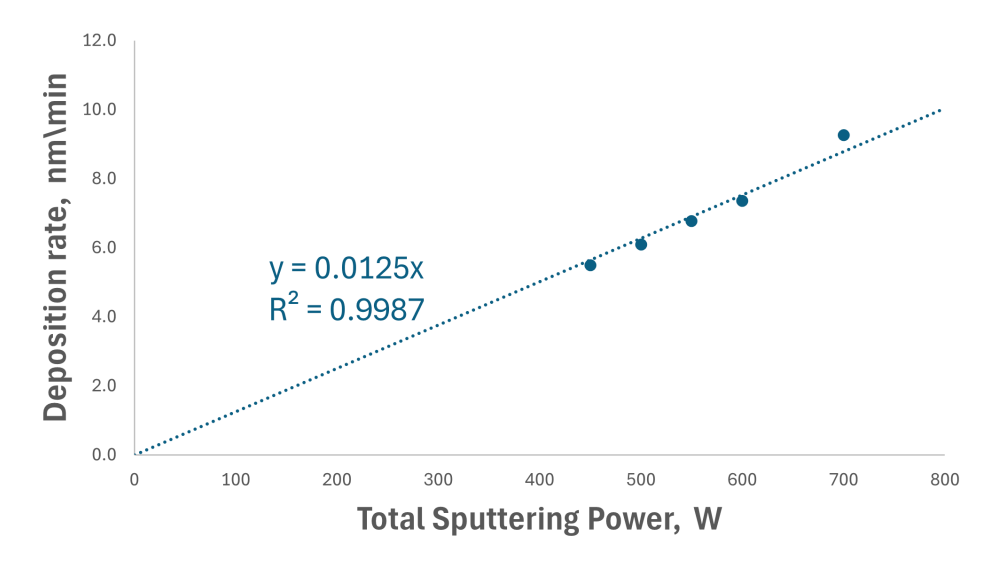


Figure 4.17: Effect of total sputtering power on deposition rate of AlScN. Linear fit results with corresponding R² value included.

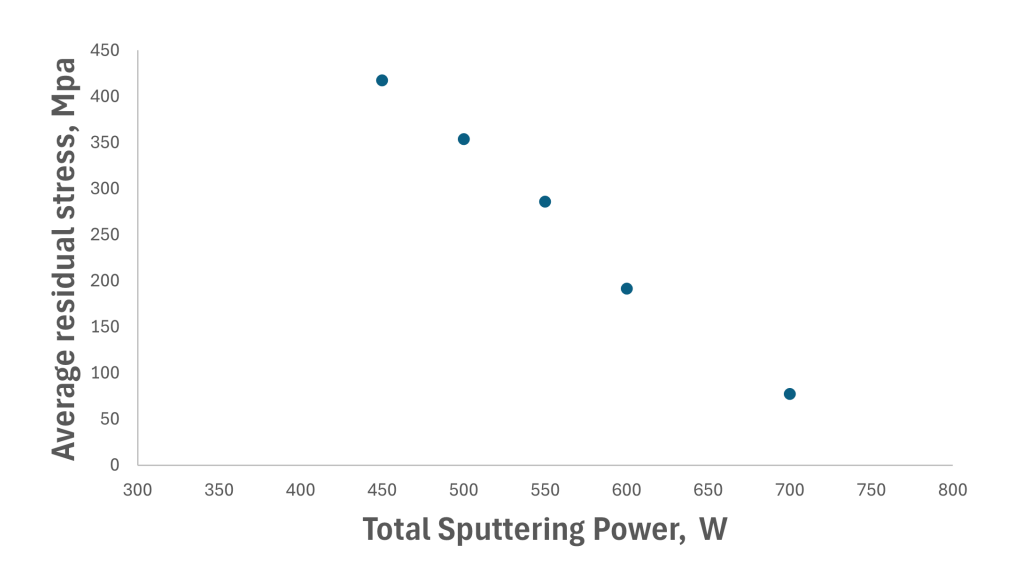


Figure 4.18: Effect of total sputtering power on residual stress values of AlScN thin films.

Finally, the EDX measures revealed a clear correlation between the concentration of Sc and the Sc sputtering power. The measures were conducted with electron accelerating voltages of 8kV and 10kV. The atomic concentrations of N, Al and Sc and x_{Sc} measured for both accelerating voltages are reported in Table 4.10. The results showed a clear correlation between the Sc Sputtering Power Ratio and the Sc concentration detected in the films. The x_{Sc} values obtained are slightly higher than predicted, and

are coherent between the two accelerating voltages, with the exception of the film with the highest Sc concentration. For this film the two measures showed a discrepancy of 0.03, with the 10 kV measurement showing a lower concentration of Sc in the film. The N atomic concentration is also significantly higher than the sum of the metals concentrations, indicating a wrong stoichiometry of the films. However this discrepancy can be motivated as the Characteristic K α 1 X-Ray line of nitrogen is very close to the L α 1 line of Sc, (392.4 eV against 395.4 eV) [92]. Further measuring of the concentration, for instance X-Ray Photon Spectroscopy (XPS) would clarify the actual stoichiometry of the film and provide more accurate concentration measures, but that goes beyond the scope of this test. In Figure 4.19 are reported the values of x_{Sc} in function of the Sc Sputtering Power ratio, together with the values extrapolated from the linear fitting reported in Figure 4.16 and their linear fit. The results summary of this test is reported in Table 4.11.

Table 4.10: Atomic concentration of N, Al and Sc measured by EDX for AlScN thin films on Si at 8 kV and 10 kV electrons accelerating voltages.

$r_{P,Sc}$	N %at (8 kV/10 kV)	Al %at (8 kV/10 kV)	Sc %at (8 kV/10 kV)	x_{Sc} (8 kV/10 kV)
0.43	37.87 / 32.9	14.73 / 18.88	11.21 / 12.52	0.432 / 0.399
0.33	35.47 / 34.67	13.78 / 19.11	6.74 / 9.26	0.328 / 0.326
0.27	33.99 / 32.48	13.91 / 19.78	5.46 / 7.65	0.282 / 0.279
0.20	33.89 / 43.54	14.11 / 16.36	3.79 / 4.27	0.212 / 0.207
0.11	30.55 / 30.23	14.13 / 20.84	1.89 / 2.73	0.118 / 0.116

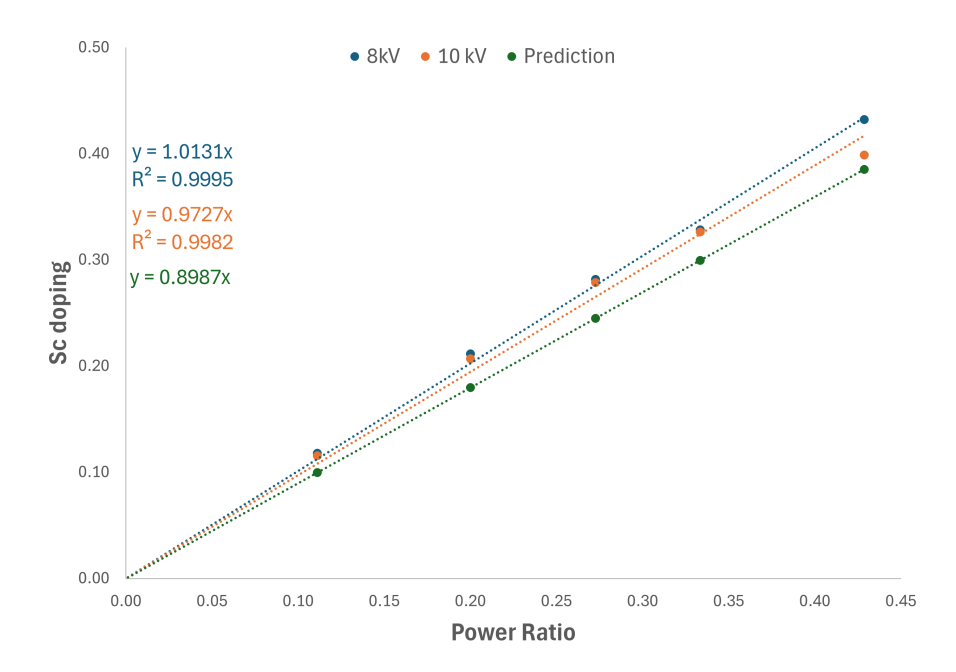


Figure 4.19: Correlation between Sc concentration in film and Sc sputtering power ratio. Linear fit results with corresponding \mathbb{R}^2 included.

Table 4.11: Results summary for the Sc doping test

P_{tot} (W)	$r_{P,Sc}$	t_f (nm)	Δt_f	r_{dep} (nm min $^{-1}$)	$\overline{T_{av}}$
700	0.43	277.8 ± 3.2	6.89%	9.3	77±1
600	0.33	220.5 ± 2.1	2.97%	7.4	192 ± 3
550	0.27	203.3 ± 0.6	0.96%	6.8	286 ± 3
500	0.20	182.7 ± 0.0	0.06%	6.1	354 ± 3
450	0.11	164.6 ± 0.1	0.23%	5.5	417±3

5. Microdevices realization

5.1 FBAR design

The main purpose for the realization of these microdevices was the analysis of the piezoelectric properties of the AlN thin films deposited with the optimized parameters. To do so a Free-Standing Bulk Acoustic Resonator was selected as a relatively simple kind of microdevices which behavior is strongly dependent on the properties of the piezoelectric layer included in it. An FBAR is composed of three layer: a bottom electrode (developed in Chapter 3), a piezoelectric layer (developed in Chapter 4) and a top electrode. These layers form a membrane that is anchored at the edges to the substrate. The area where the bottom electrode and the top electrode overlap over the piezoelectric layer is the active area of the resonator. Here the piezoelectric film is excited by the oscillating electric field and generates an acoustic wave in the thickness direction of the film. The FBAR systems are characterized by a resonance frequency, for which the piezoelectric film produces an acoustic standing wave confined in it, which in turns modifies the electric field distribution and the impedance of the system [93]. To generate a standing acoustic wave the thickness of the thin film must be an integer multiple of half the wavelength. The basic resonance frequency can then be derived knowing the velocity of the acoustic wave in the film (Eq. 5.1)

$$f_r = \frac{v_a}{2t_f} \tag{5.1}$$

For a [001] oriented AlN film, the bulk acoustic velocity is derived as follows: (5.2)

$$v_a = \sqrt{\frac{c_{33}}{\rho}} \tag{5.2}$$

where c_{33} is the stiffness coefficient of AlN in the [001] direction. At the resonance frequency f_r the measured admittance of the system is maximum. FBAR devices are also characterized by an anti-resonance frequency f_a , where the measured impedance is maximum. The FBAR's effectiveness for converting the electrical power into mechanical power is defined as the Effective Coupling Coefficient, k_{eff}^2 . According to the IEEE Standard of piezoelectricity [14] the Effective Coupling Coefficient is defined on the base of the frequency distance between the resonance frequency and the anti-resonance frequency (Eq 5.3)

$$k_{eff}^2 = \frac{f_a^2 - f_r^2}{f_a^2} \tag{5.3}$$

This parameter can then be correlated to the coupling coefficient for an AlN piezoelectric film excited by an electrical field perpendicular to its thickness (Eq 5.4)

$$k_{33}^2 = \frac{d_{33}^2}{s_{33}^E \varepsilon_{33}^T} \tag{5.4}$$

In which d_{33} is the piezoelectric strain coefficient, the strain generated per unit of electric field applied, s_{33}^E is the elastic compliance at constant electric field and ε_{33}^T is the dielectric constant at constant stress. The 33 subscripts denotes that the strain, electrical field, polarization and stress are along the 3 direction, which for wurtzite crystalline lattices is defined as the c-direction, the one the AlN film produced in this work are oriented. By measuring the FBAR coupling coefficient is then possible to estimate the piezoelectric properties of the AlN. As k_{eff}^2 still depends on the configuration of the device, (e.g. the mass loading of the resonators, the losses in the electrodes ...) and k_{33} is defined by three terms that can all vary depending on the properties of the film, the assessment of piezoelectric quality of the film is limited to the confront of the measured k_{eff}^2 to the theoretical value obtained by an ideal AlN layer. From the values measured by Kurz et al. [35] the k_{33} theoretical value of 7.46 % is calculated according to Eq 5.4.

To realize the FBAR devices following the process flow reported in Table 2.1, two photolithography steps are required, one for patterning each electrode. For each step a 2D layout must be designed to instruct the direct laser writing tool were to expose the photoresist mask. As the PR used are positive, the exposure directly translates the designed pattern on the PR. The mask are however are used to protect the layer from the Ion Beam Etching, so the definition of the pattern is actually the negative of the layout. The bottom electrode was designed starting from the shape of the active area of the resonator, set as a circle or a irregular pentagon of varying sizes. The bottom electrode is then connected by traces to two 100 μm x 100 µm pads spaced 300 µm where the signal electrodes of the testing probes will land. The length of the traces is determined considering that the devices will be suspended by isotropic etching of the Si substrate, so they must be long enough to ensure that the devices are still anchored to the wafer. An array of five geometries was produced, composed of three circular active areas with diameters of 200 µm, 400 μm and 600 μm and two pentagonal active areas of characteristic size of 350 μm and 550 μm. The traces were set to leave at least 300 µm of distance between the area to be suspended and the contact pads. To realize the layout for the bottom electrode etching mask, 50 μm were added to the perimeter of the pattern, the shapes were aligned at the contact pad and distanced 400 µm from each other. This array was then repeated on a grid of 4 columns spaced 8 mm and 6 rows spaced 4 mm. At the end four grids were fitted on the wafer together with alignment marks for succesive photolithographies. The resulting layout for the PR mask is reported in Figure 5.1 The next photolithography step was used to define the PR mask for the top electrode mask. The Top electrode was simply composed of the active area connected by a trace to the contact pad for the ground electrode of the probe, put in the middle of the two other pads. The layout was then created by removing this shape from the outline of the previous layout. The result is reported in Figure 5.2.

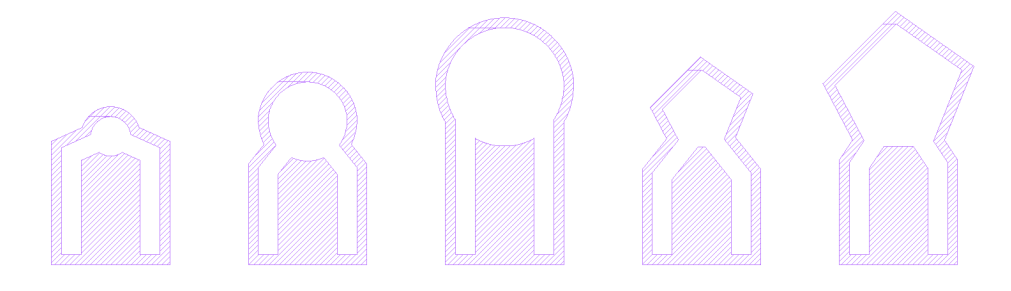


Figure 5.1: Layout for the bottom electrode etching mask.

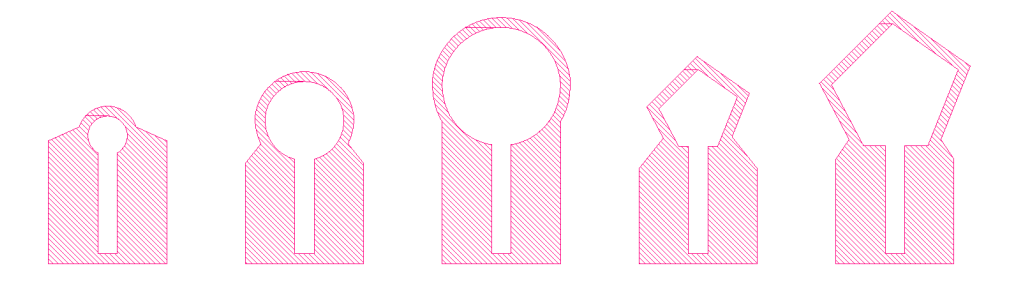


Figure 5.2: Layout for the top electrode etching mask.

With this design the top electrode is used as the mask for the wet etching of AlN. This comports

that the bottom electrode is easily accessed, but a large area of the substrate is exposed. To address this problem another PR mask was developed to limit the area attacked by XeF_2 . This mask was designed to create openings 25 μm wide of the side of the active area, with a margin of 5 μm from the edge of the active area. However an important flaw in the design, which was identified only after the patterning of the top electrode, caused the redesign of this mask and the necessity of cleaving the wafer in two parts. If all the devices would have been released at the same, the etched areas of the substrate would have connected, as the spacing between devices was not large enough. This in turn would have created a large and thin membrane between the devices, which would very likely break off, damaging the devices. To avoid that, one half of the wafer was patterned for the release of the three smallest devices, and the other half for the release of the larger devices. The opening were then randomly distributed over the device to minimize the risk of creating a large membrane.

The FBAR design was realized at the same time of the optimization of the AlN deposition. Maintenance intervention on the CT200's Process Module 6 halted the depositions of AlN for some time, which was instead exploited to realize another kind of device, High-Overtone Bulk Acoustic Resonators (HBAR). This allowed to test some steps of the realization of the FBAR and possibly characterize the piezoelectric properties of AlN films already deposited.

5.2 HBAR development

HBAR were selected mostly because they potentially required only one step of photolithography for the patterning of the top electrode. This device is composed of the same layers of an FBAR, but they are not separated to the substrate. The device works by exciting the piezoelectric layer with an electric filed perpendicular to it. The acoustic waves produced in this way travel in the substrate and are reflected at the bottom of it. The response obtained is then the overlap of the response of the FBAR-like stack to the resonance modes of the substrate. As the substrate thickness is way larger than the one of the piezoelectric layer, its resonant frequency is way smaller than the one of the piezoelectric layer. The expected frequency response would then show oscillations of the signal with spacing equal to the basic resonant frequency of the substrate (overtones), and a global maximum and minimum related to the resonance and anti-resonance frequency of the piezoelectric layer, allowing for the determination of the piezoelectric properties of the film [94].

5.2.1 First HBAR design

The first design for these devices was the one port configuration, in which only the top electrode is patterned, and the device is contacted on the active zone and the rest of the top electrode id grounded. Two wafers were chosen to realize the HBAR devices. Their AlN films were the one with the best crystalline properties at the time, and were the results of the substrate bias test (Section 4.3). A simple layout was created, using three active areas geometries, with their characteristic size varied between five values. Each geometry was then repeated in a 3 by 4 grid. The geometry chosen were a circle, a circle with a 50 μm x 100 μm contact pad added, and a regular pentagon; the diameter of the first two shapes was varied between 100 μm and 1600 μm, while the size of the pentagon was varied between 60 μm and 940 µm. Finally the mask layout was obtained by extending the perimeter of the active areas by 100 μm. The top electrodes were deposited by sputtering in the CT200 tool (PM 2 was still available), following the optimized recipe for Pt deposition reported in Table 3.9. The sheet resistance of both films was measured, resulting in an average value of $2.45\pm0.02~\Omega/\text{sq}$ and $2.49\pm0.02~\Omega/\text{sq}$, slightly higher than the value measured for the bottom electrode, but still acceptable. The wafers were then coated with PR, the layout was exposed on the PR with the laser writing machine and then developed. A reflow step was done to ensure that the ion beam etching was not going to generate metallic fences. The etching tool was set to the medium power configuration, with an incidence angle of -10°. The film were etched for 60 s. After stripping the PR with an O₂ plasma ashing tool, the result of the etching were quickly tested on the etched side with a multimeter, to prove that the bottom electrode had been completely removed were the mask was open. The results were then observed with SEM, which confirmed that the patterning was successful and that the geometries were respected (Figure 5.3).

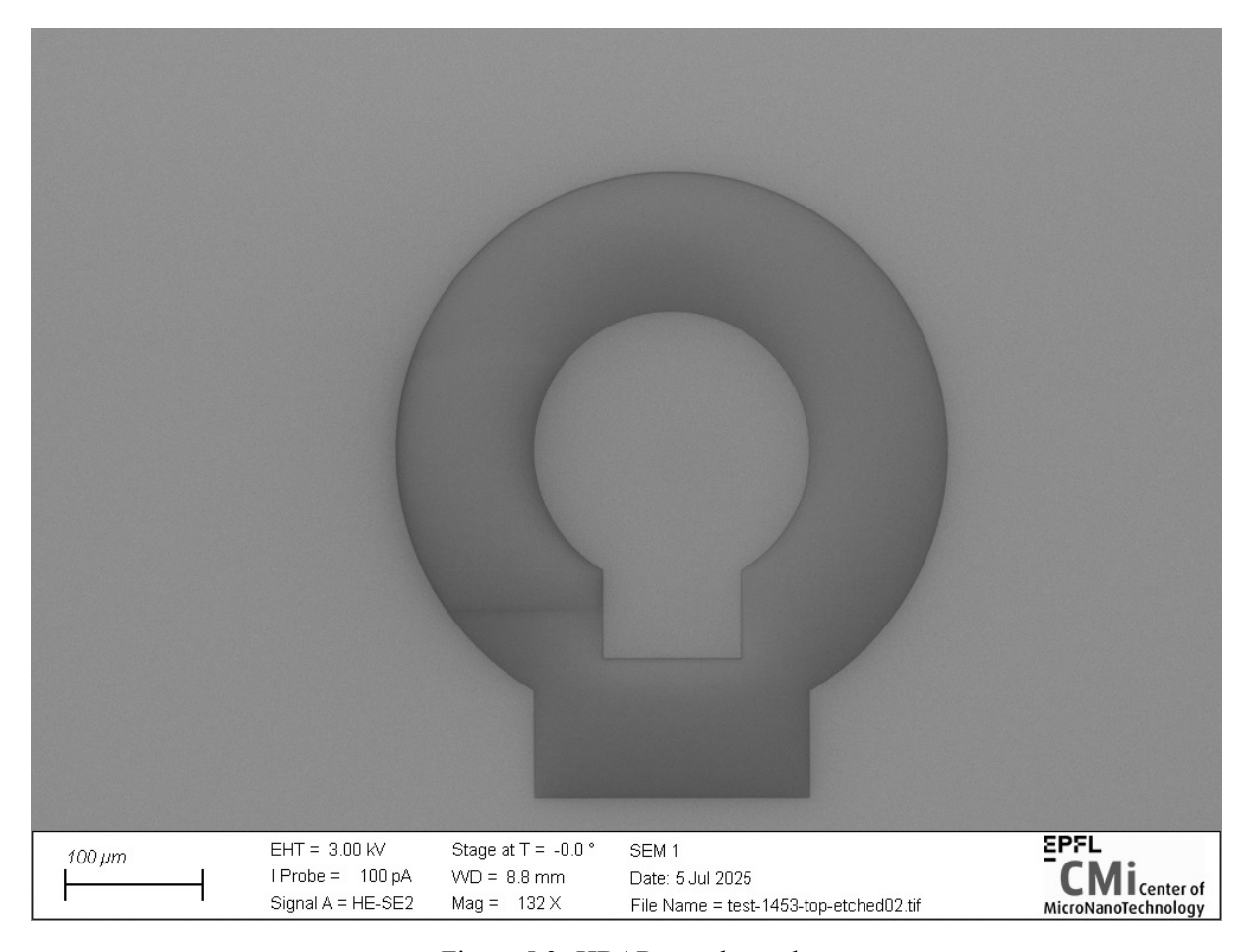


Figure 5.3: HBAR top electrode

The frequency response of these HBAR was then measured, but the results were inconclusive, as the measurement did not show any ordered response. This failure was attributed to two factors: the substrate and the device design. The substrates used for the deposition of the films were test wafers acquired by CMi, that were polished on only one side. The backside of the wafer was then too rough to reflect the acoustic waves, and it was scattering them instead. The surface roughness of the backside was estimated to have a R_q value higher than 1 μ m, as it was not measurable with the AFM. The devices design instead degraded the response as the bottom electrode potential was not controlled, and the active area of the piezoelectric film was not clearly defined, as it was possible that the rest of the top electrode was extending the area were the piezoelectric film was being actuated.

5.2.2 Second HBAR design

To tackle these issues, one of the wafer was ground down to 400 µm to reduce its roughness, which resulted in an average roughness of 32.3 nm. The design was then updated to a two-port HBAR. The top electrode would have remained only on top of the piezoelectric layer, which in turn would have been etched completely to reveal the bottom electrode. In this way the probe would have been able to land on the bottom electrode, and control precisely its potential. The removal of the piezoelectric layer around the active area would have also been beneficial for reducing the dampening of the film oscillations. To realize this design the top electrode was etched following the same procedure described above, only by updating the layout to increase the area exposed to the ion beam. After that the AlN films were etched with submersion in AZ 726 MIF developer for 390 s, after which they were submerged in water for 60 s seconds and the rinsed again. This etching procedure resulted in the bottom electrode covered with a thin opaque layer, that anyways allowed the conduction of electricity. SEM imaging revealed the bottom electrode being covered in small barnacle-like structures, as shown in Figure 5.4. These structures were formed due to the incomplete etching of the AlN layer, and were around 150 nm tall and 200 nm wide.

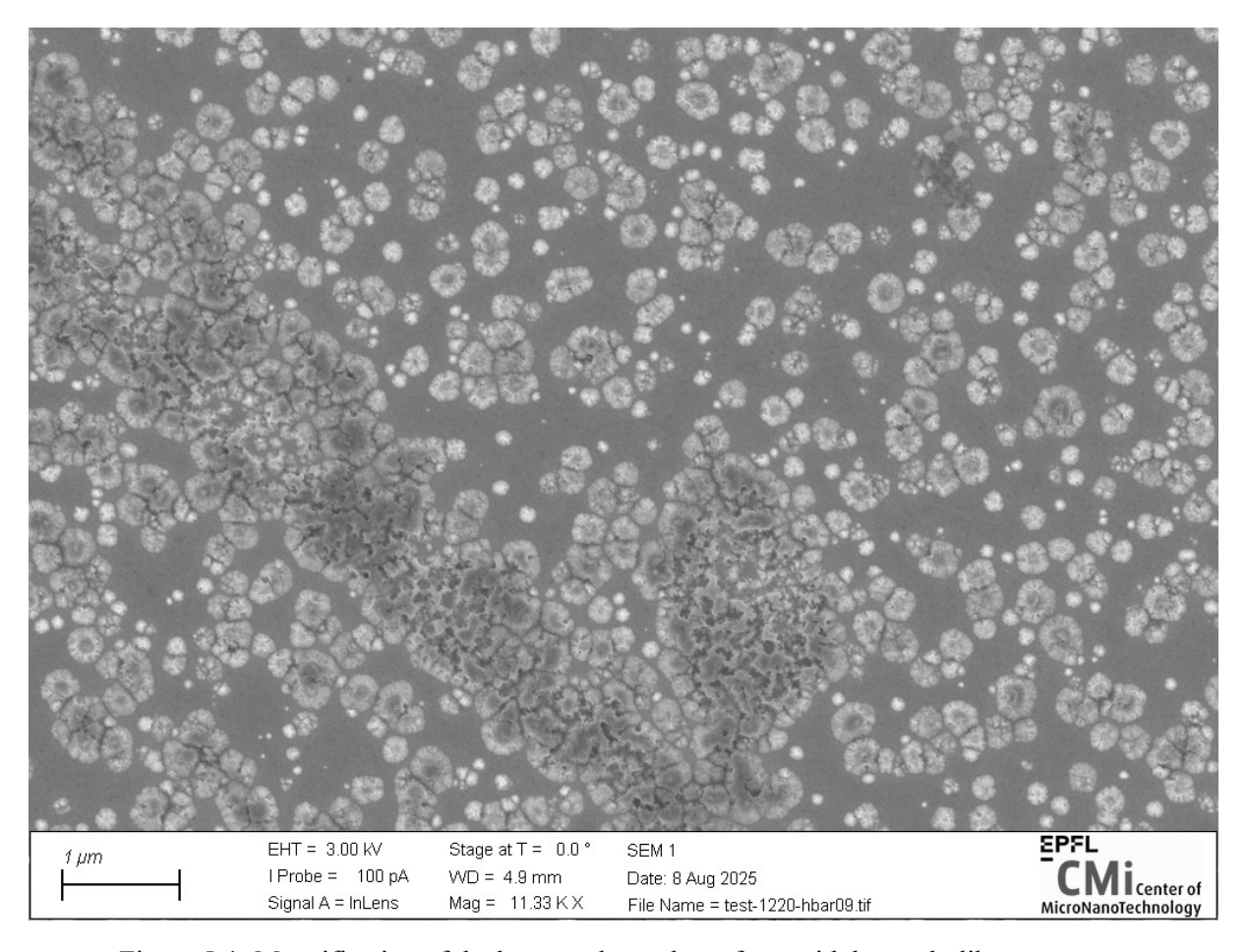


Figure 5.4: Magnification of the bottom electrode surface, with barnacle-like structures.

EDX measured confirmed that those structures were residuals of the AlN layer, with a non stoichiometric composition, richer in N. To remove those residuals, a further 150 s etching in the TMAH developer was done. The frequency response of these devices was measured again. The frequency of the signal was firstly varied between 500 MHz and 12 GHz, with a frequency step of 287,5 kHz, obtaining 40000 measures. The magnitude of the admittance as function of the frequency is reported in Figure ??. From this measure no clear resonance or anti-resonance peak is identifiable, but it is possible to observe a local minimum around 5.25 GHz and a periodical oscillation of the impedance magnitude with a period of around 10 MHz. This value is close to the predicted spacing of the Si overtones, equal to its basic resonance frequency, 10.54 MHz. This value was calculated using the data reported by Hopcroft et al. [95] and Equation 5.1 and Equation 5.2 with the parameter c_{33} substituted by c_{11} as the Silicon wafer is [100] oriented. To measure the spacing of this peaks more accurately, another measure, spanning from 4.75 GHz to 5.75 GHz, with a spacing of 25 kHz was conducted. In the end an average frequency spacing of 10.97 MHz was calculated by averaging 10 inter-peak distance measured between 4.75 GHz and 4.9 GHz. This result proved that the film was in fact piezoelectric, as the substrate was producing overtone modulations of the signal due to the mechanical actuation caused by the AlN film. However no further characterization of the piezoelectric properties was possible with these devices, and when the PM 6 was again available, the FBAR development was started.

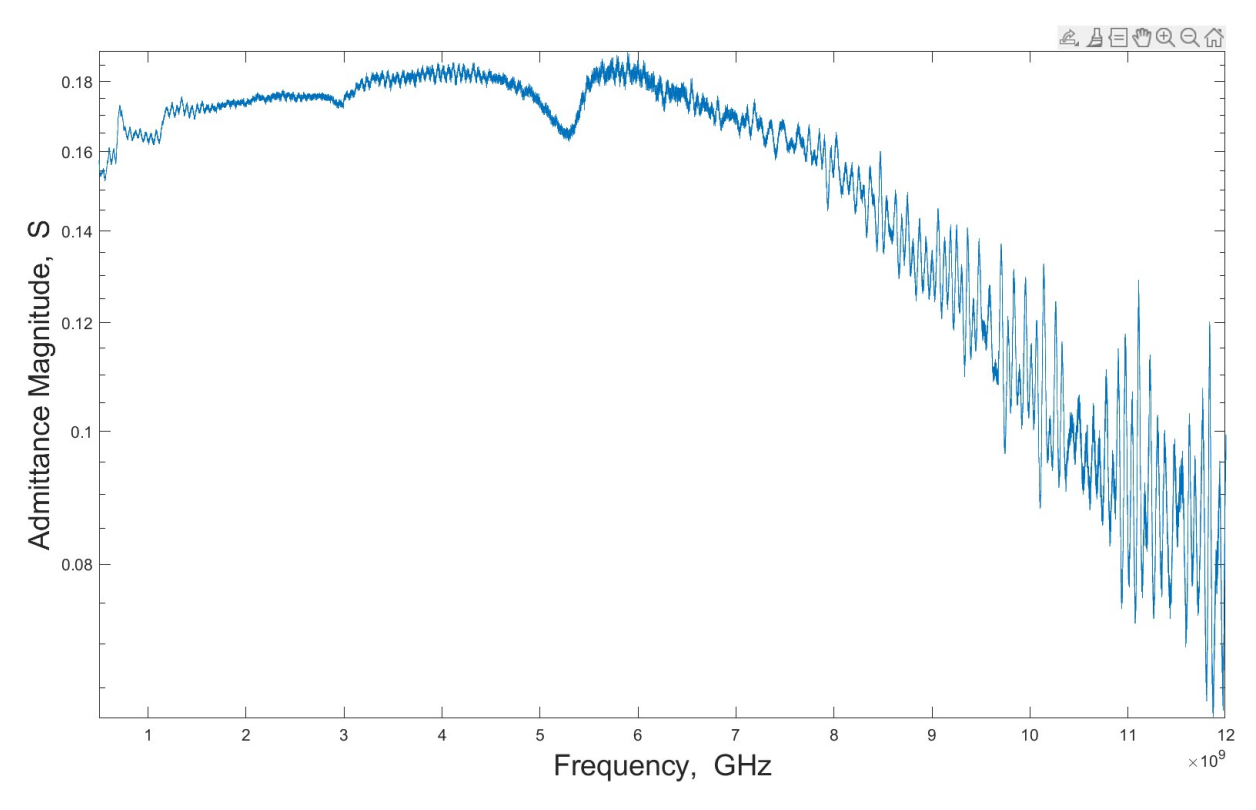


Figure 5.5: Admittance frequency response of a circular HBAR with diameter of 1600 μm excited between 0.5 and 12 GHz.

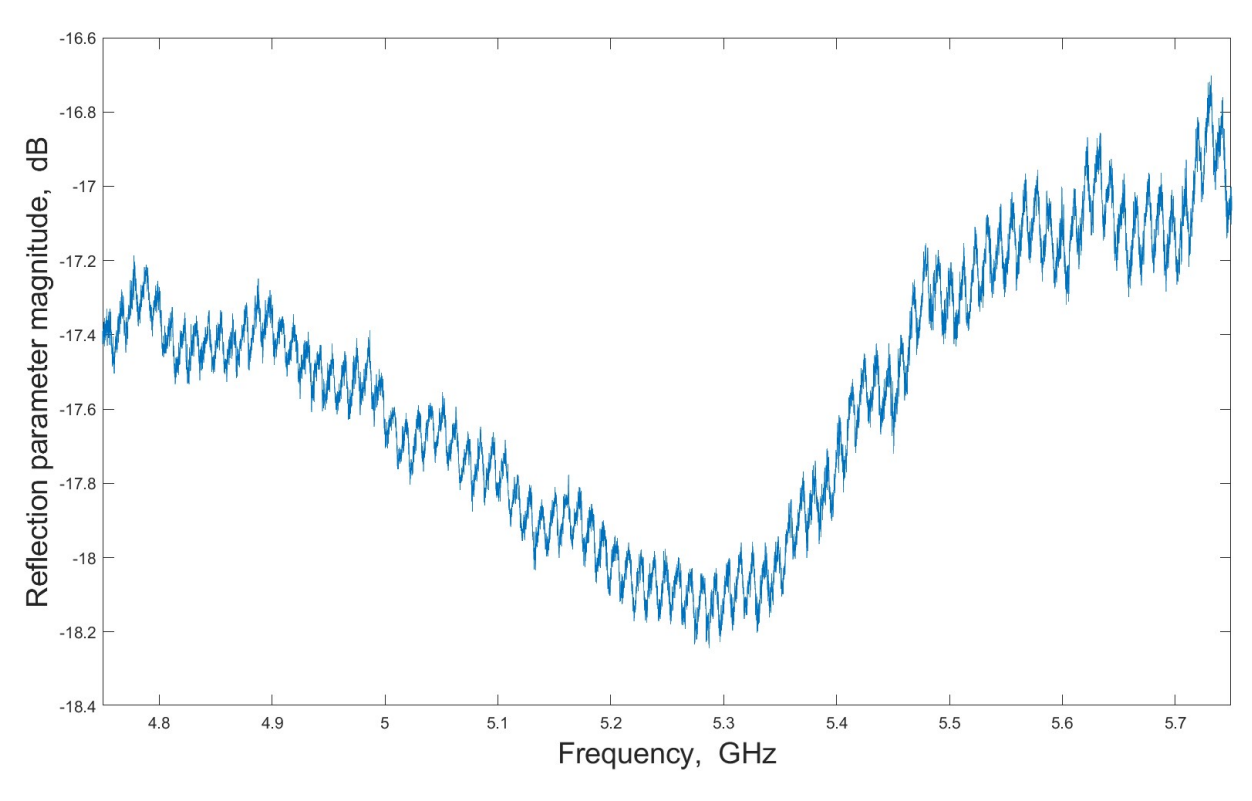


Figure 5.6: Admittance frequency response of a circular HBAR with diameter of 1600 μm excited between 4.75 and 5.75 GHz.

5.3 FBAR realization

To produce the FBAR, High resistivity wafers were used, to isolate electrically the devices from the substrate. The last step before starting the production was to test the bottom electrode etching, and then measure the properties of the AlN film deposited on top of it (discussed in Section 4.5). The patterning was done on a 50 nm Pt layer deposited with Spider600. The etching parameters were kept the same, with a medium power setting, for 60 s at -10° incidence angle. The bottom electrode was etched effectively, and the resist reflow proved to be effective to avoid the formation of metal fences on the side of the photoresist mask, that could potentially short the top and bottom electrodes (Figure 5.7). Due to the angle of incidence, a thin layer of not completely etched Pt was present at the edges of the bottom electrodes.

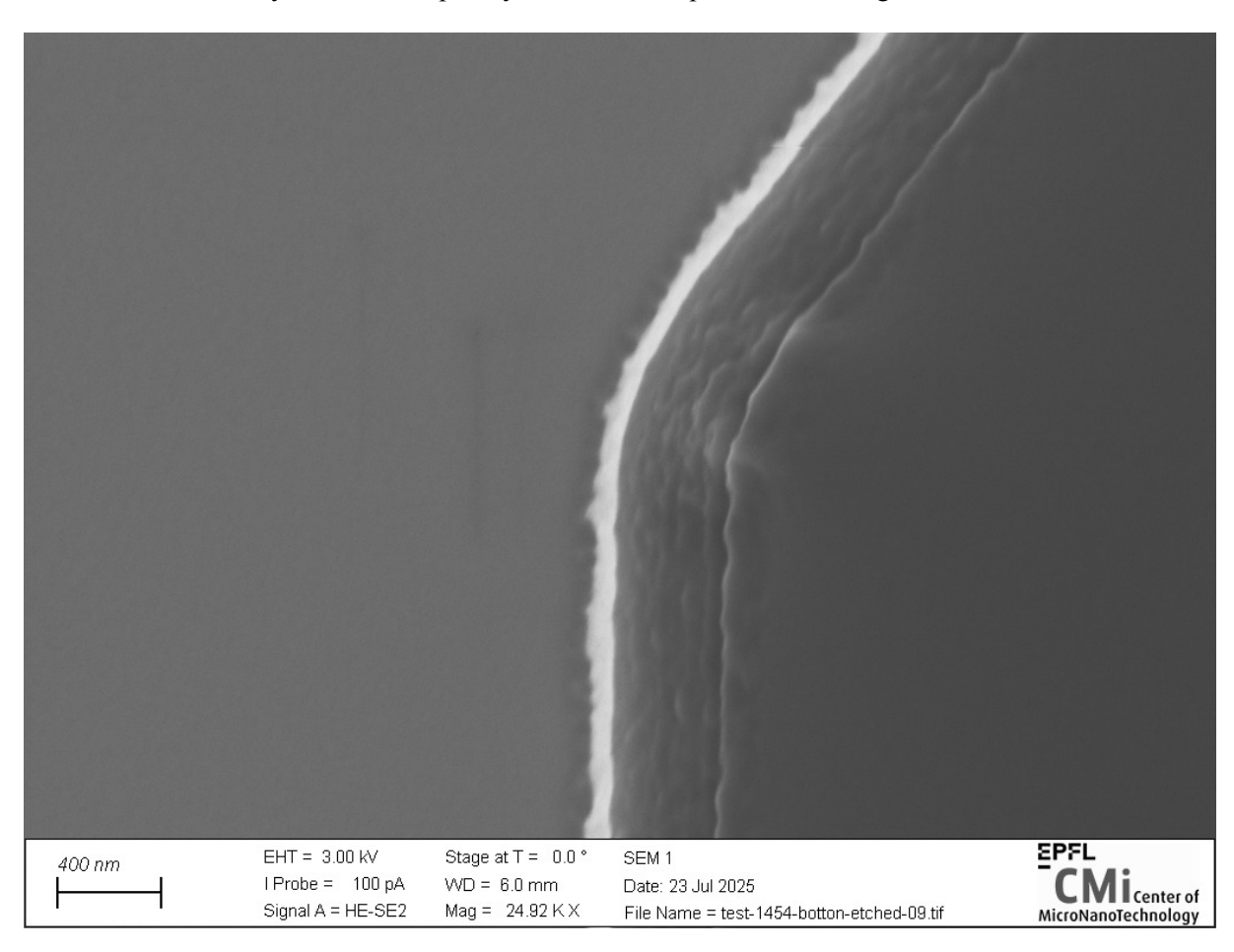


Figure 5.7: SEM image of an edge of one of the FBAR's bottom electrodes.

To ensure that no organic contamination remained on the bottom electrodes, the PR mask used for the Pt etching was removed in three steps, with an high intensity O_2 plasma for 30 s, two 5 minutes baths in SVC-14 PR solvent at 70° C, and a final plasma ashing at low intensity for 3 minutes. After the deposition test confirmed that the crystalline properties of the AlN film remained the same even when the film was deposited on a patterned electrode, two HR wafer were selected for the realization of FBAR. On one of these wafer the bottom electrode was deposited in the CT200, with the optimized recipe reported in Table 3.9. The other bottom electrode was deposited in the Spider600, with a final thickness of 30 nm. The etching was done with the same parameters described above, only halving the process time for the electrode deposited in the Spider600. The AlN piezoelectric layers were deposited following the optimized recipe reported in Table 4.8. The top electrodes were deposited immediately after, without breaking the vacuum. The sheet resistance of the top electrodes was measured, and resulted in an average value of 2.91 Ω /sq, higher than predicted. The top electrode was then patterned with the same parameters as the bottom electrode, and the resist was stripped only using the plasma asher. To etch the AlN layer, the wafer were submerged in two baths of AZ 726 MIF developer, for 5 and 3 minutes respectively, and

then submerged in deionized water for 2 minutes and rinsed three times before being dried. Even in this case some residuals of the AlN film remained, and it was noted that their distribution was denser on the areas with Pt than on the areas with Si (Figure 5.8). This was probably due to the fact that also Si is etched by TMAH, and some of the AlN aggregates could have been removed by etching their anchorage to the substrate.

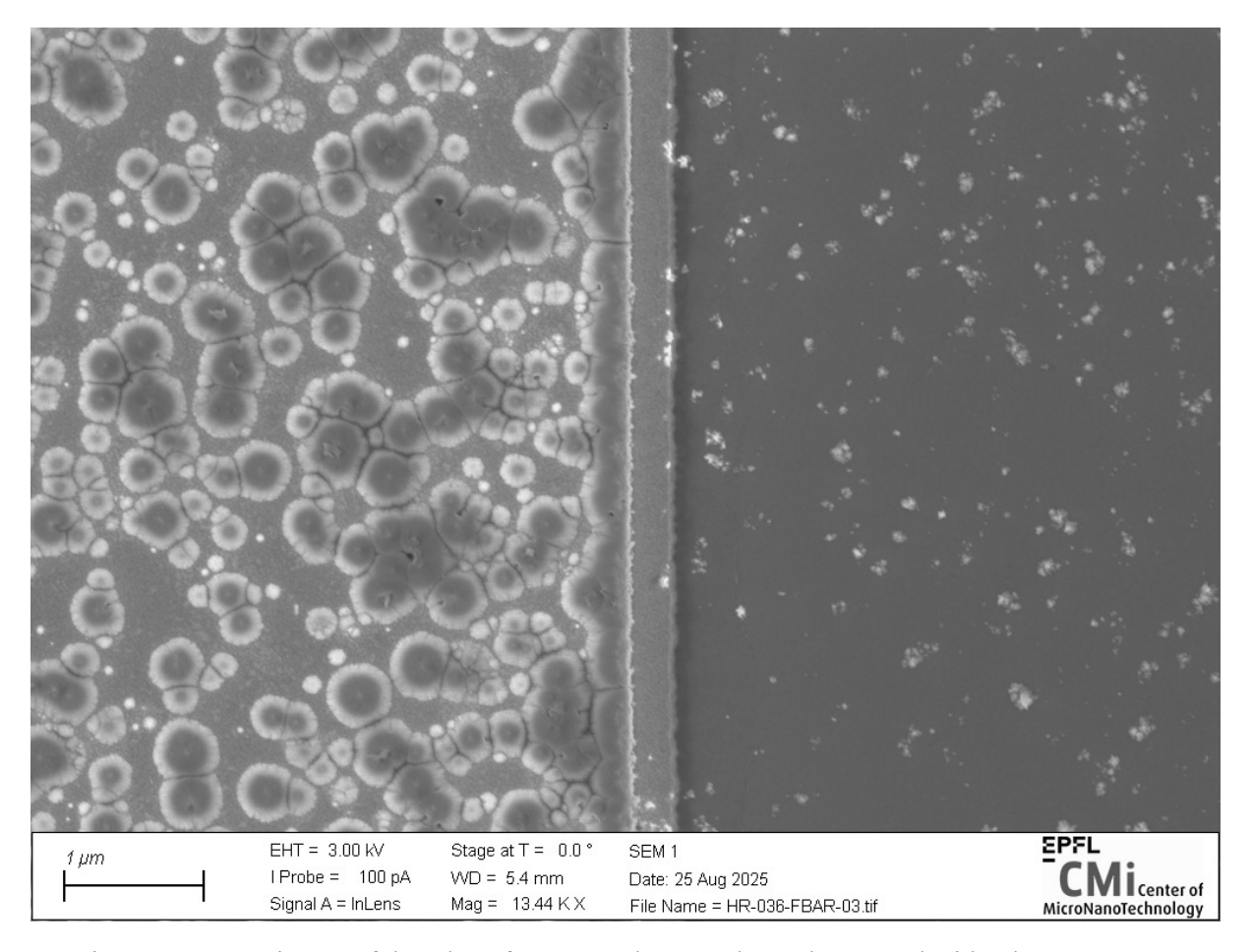


Figure 5.8: SEM image of the edge of an FBAR bottom electrode covered with AlN aggregates.

However these aggregates did not stop the bottom electrode from conducting electricity, and they would have probably been scraped off by the measuring probes, so the production process continued to the last step, the release of the devices from the substrate. As anticipated before, the layout design could have not been used to release all the devices together, so and additional PR mask was realized on top of the wafers, and the wafers were cleaved in half. Due to limited time, the release was done on only one of the half-wafers, the one with the bottom electrode deposited in the Spider600, with the mask patterned for the release of the three smaller devices. To release the devices initially 45 etching cycles of 45s were done, but controlling the results with an optical microscope different from the one integrated in the etching tool the devices were not released, as can be seen in Figure 5.9. To solve this issue, 20 additional etching cycles were done, resulting in the release of most of the devices. However, due to the tensile residual stress in the films the devices raised from the plane of the wafer, as can be seen in Figure 5.10. In this context the selection of Pt as the electrodes material proved to be appropriate: Pt is highly ductile, and can reach values of elongation at break up to 35% [96]. Metals more brittle than Pt would have probably broken due to the large deformation. Despite this non ideal configuration, the FBARs were ready for measurement.

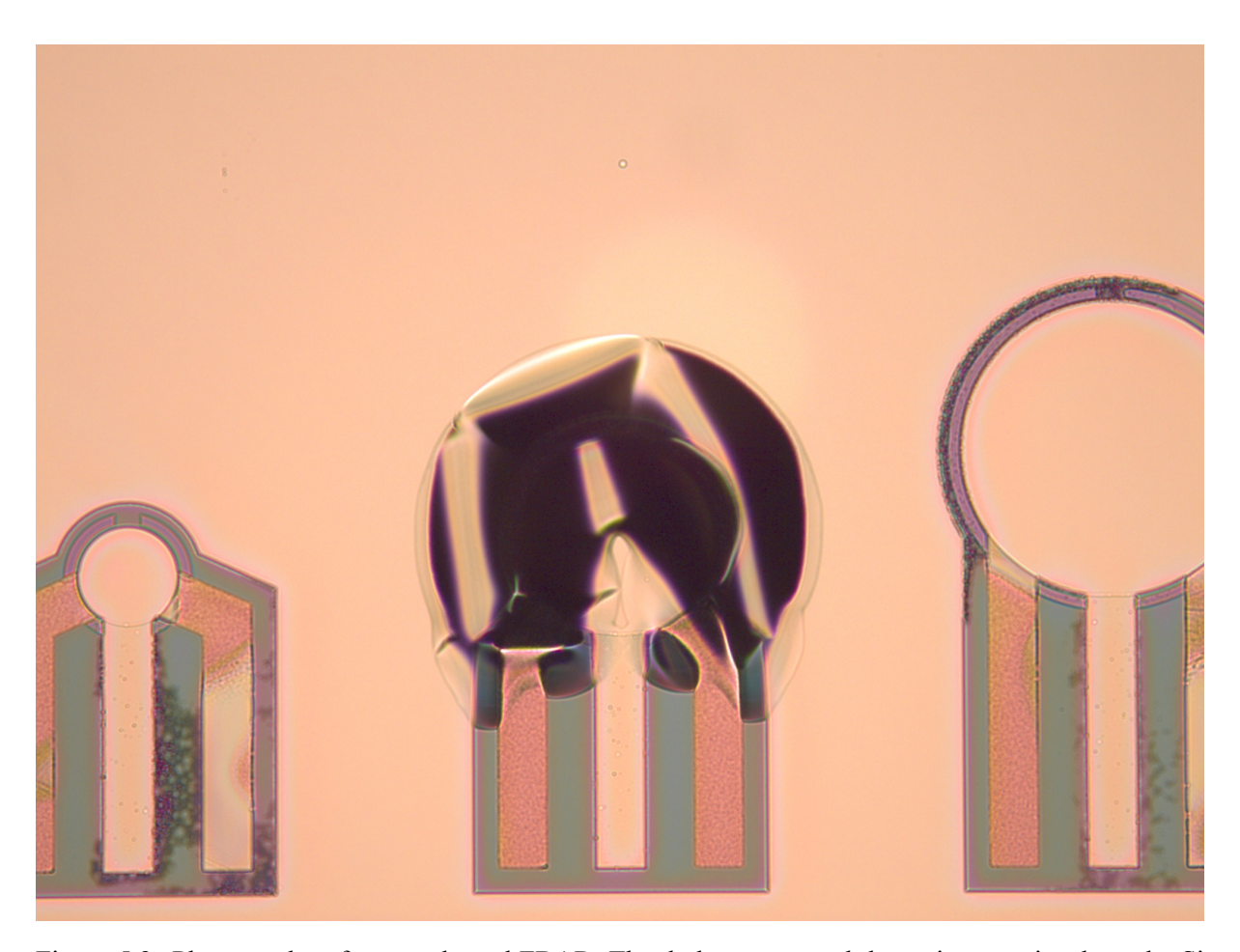


Figure 5.9: Photography of an unreleased FBAR. The dark area around the active area is where the Si has been etched.

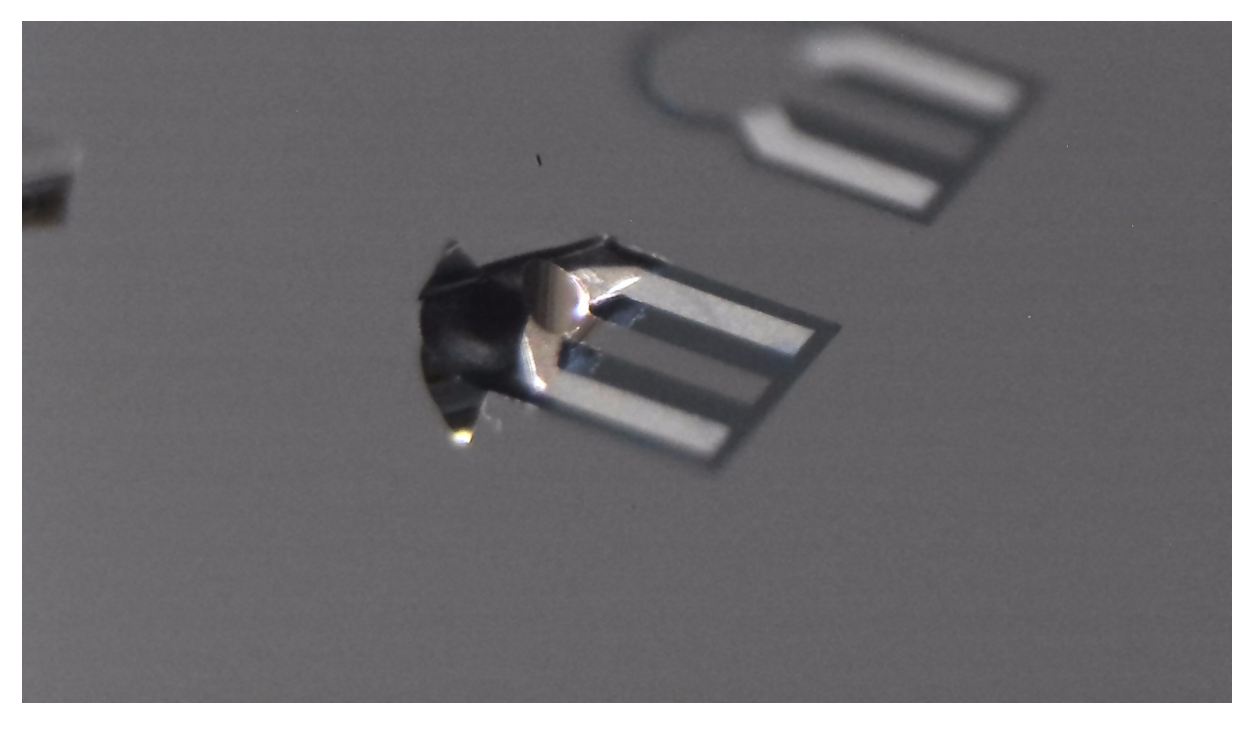


Figure 5.10: Side view of a released FBAR.

5.4 FBAR frequency response

The frequency responses of the FBAR devices were measured from 0.5 GHz to 12 GHz, with a frequency step of 287.5 kHz (40001 values measured). The admittance measures showed the minimum value associated to the anti-resonance frequency, but no clear maximum value associated to the resonance frequency. For the FBAR whose frequency response is reported in Figure 5.11, f_a was estimated at 6.44 GHz. This is caused by the low resonance quality factor, that express the ratio of energy conserved in the FBAR to the energy dissipated at the resonance frequency. One way of calculating it is by the 3 dB bandwidth method, reported in Eq. 5.5:

$$Q_r = \frac{f_r}{|f_1 - f_2|} \tag{5.5}$$

where f_1 and f_2 are the frequencies for which the admittance is 3 dB lower than the maximum value at resonance. Q_s is mostly related to resistive losses in the electrodes [97], meaning that the electrodes are not optimized for an FBAR device. On the other hand the anti-resonance peak is visible, showing an higher quality factor for the piezoelectric layer, calculated in the same fashion as Eq. 5.5 to be $Q_a = 252$.

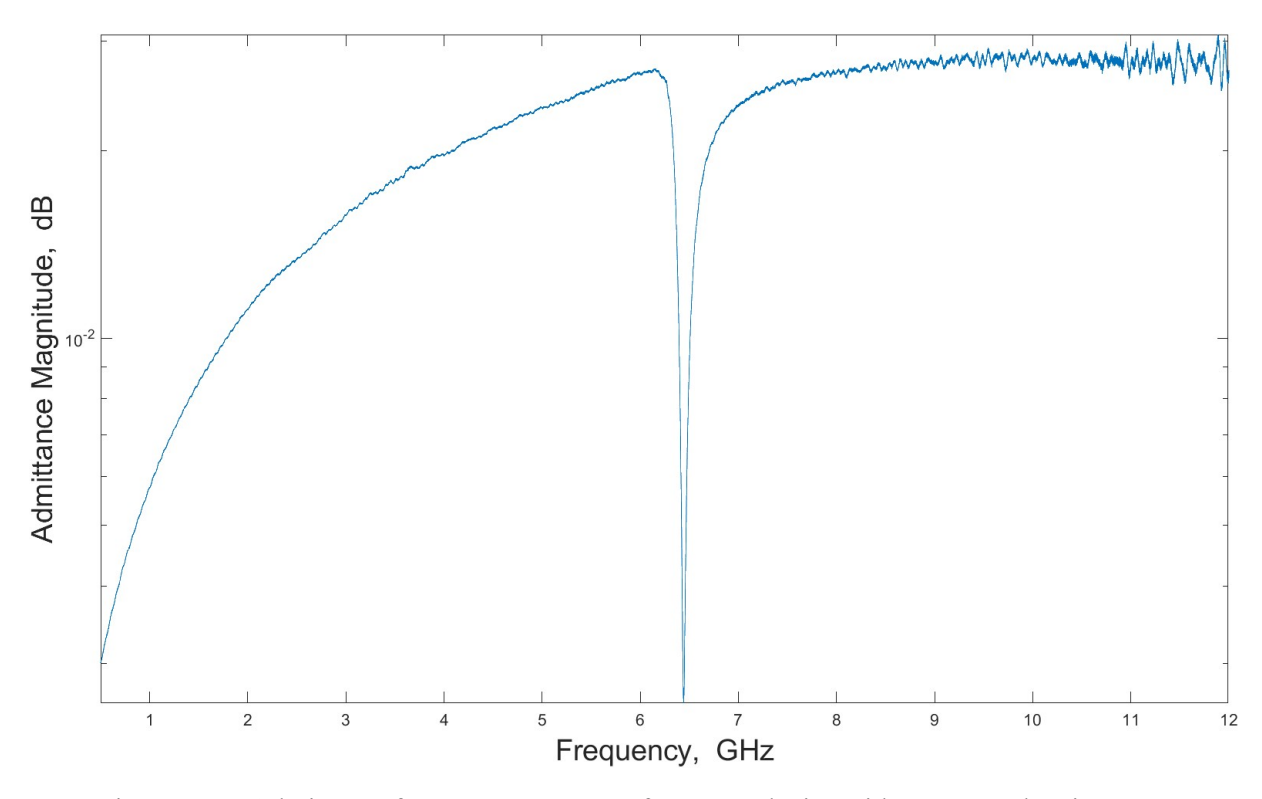


Figure 5.11: Admittance frequency response of a FBAR device with pentagonal active area.

This measure proved that the film was piezoelectric and the FBAR was working, meaning that the system still possessed a resonance frequency, needed to determine the effective coupling coefficient. To do so, the reflection coefficient S_{11} of the FBAR was used instead of the admittance. S_{11} measures of much the electrical signal is reflected from the resonator and can be calculated by Eq. 5.6 [98]:

$$S_{11} = \frac{Z_L - Z}{Z_L + Z} \tag{5.6}$$

in which Z_L is the line impedance (in this case 50Ω) and Z is the impedance of the system. S_{11} is then minimum at resonance frequency and maximum at anti-resonance frequency. Ideally the reflection coefficient should be null at resonant frequency, as the energy should be completely stored inside the resonator, but in lossy systems that is not the case. The measures of S_{11} showed two clear peaks related to f_r and f_a . For the FBAR whose response is reported in Figure 5.12 those two values are 6.25 GHz

and 6.46 GHz respectively, from which a k_{eff}^2 value of 6.20 % can be calculated from Eq 5.3. This value is comparable with the theoretical value of k_{33}^2 calculated for AlN, 7.46 %, indicating that despite the poor performance of the FBAR, the AlN film produced in the CT200 showed satisfying piezoelectric properties.

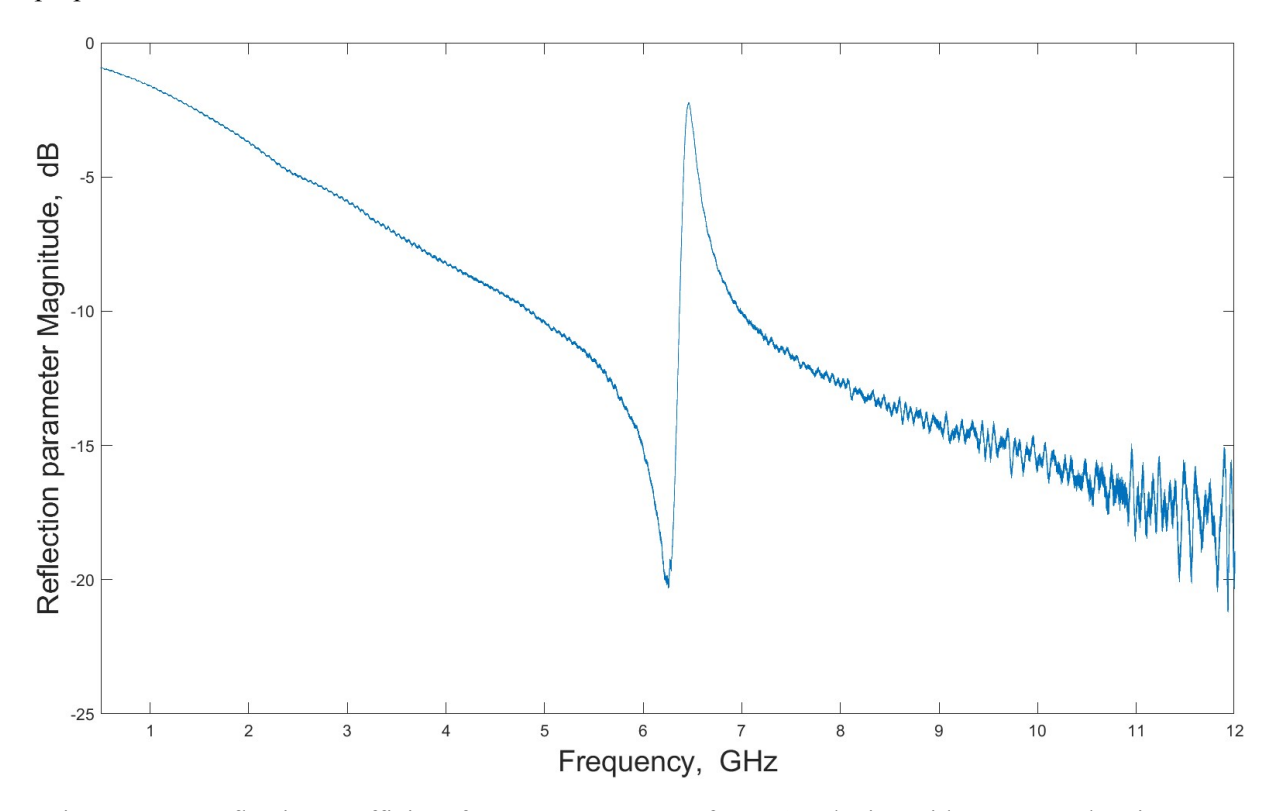


Figure 5.12: Reflection coefficient frequency response of a FBAR device with pentagonal active area.

6. Conclusions

In this work, the CT200 sputtering tool was assessed as an effective tool for the deposition of thin films used to realize functioning microdevices. Pt thin films, with a thickness of 50 nm were deposited and characterized, showing a resistivity only 11% higher than the bulk material and a good degree of orientation in the [111] direction. Their crystalline properties showed a strong dependency to the deposition pressure, and this turned the process highly sensitive to the contamination of the deposition chamber by outgassing oxides. While this issue was resolved by cleaning the dedicated deposition chamber, this solution is not applicable in the long run for a laboratory facility that counts hundreds of users such as CMi. Either the moving of the Pt target to another process module of the chamber or the development of a pre-deposition treatment of the chamber is an applicable solution to ensure consistent results for the Pt films. The optimized Pt bottom electrodes proved to work as an effective growth layer for the deposition of ordered AlN film.

These films showed a preferential [001] growing direction, associated with the highest piezoelectric response of the material. The films were polycrystalline and the optimization of the deposition process resulted in films showing an average crystallite size of 105 nm and a FWHM of the rocking curve of 1.72°, values compatible with the application in piezoelectric MEMS. The main parameter for improving the crystalline orientation of these film was the application of a RF power of 5 W on the substrate during deposition. The increase of N₂ in the sputtering gas mixture showed promising effects for the enhancement of AlN grains orientation, with rocking curves FWHM of 2.03°, but at the cost of a significant decrease of the deposition rate, from 5.5 nm min⁻1 to 3.5 nm min⁻1. This was due to the tool limitations, as the maximum value for the nitrogen flux was limited to 25 sccm, rendering necessary to drop the total gas flow or deposition pressure in order to achieve higher concentration of Nitrogen in the sputtering gas. The tool also proved to be able of depositing AlScN with controlled Sc concentration by varying the ratio of power delivered on the Sc target. The implementation of a N₂ flow line with higher volume would be the next step for a further optimization of AlN deposition in the CT200, while omptimizing the deposition of AlScN could open the way for significant developments, such as the deposition of ferroelectric layers, or films with a concentration gradient of Sc.

Finally, HBAR and FBAR devices were realized and characterized. HBARs were realized using films obtained during the optimization tests of the AlN deposition, and their frequency response confirmed the presence of piezoelectricity in the films deposited. FBAR devices were realized and from their frequency response an effective coupling coefficient of 6.20 % was determined, compared to a theoretical limit for AlN of 7.46%, proving that the AlN film deposited with the optimized recipe exhibited good piezoelectric properties. The FBAR themselves however showed several problematic, as the quality factor for the resonance frequency was extremely low, indicating high resistive losses in the electrodes, and the tensile residual stress caused the devices to raise out of the wafer plane once released from the surface. The optimization of the devices was not in the scope of this thesis, but it is evident that the improvement of the device design and realization would allow for a better characterization of the thin films.

List of Figures

1.1	AlN wurtzite crystalline lattice, view from a plane parallel (a) and perpendicular (b) to c direction [4, 13]	2
2.1	Front view of CT200 cluster, showing the loadlock open and the control screens	9
2.2	Back view of CT200 cluster, with all the modules open.	10
2.3 2.4	Schematics of IBE350. The loadlock is not represented	12 14
3.1	θ -2 θ scan for the sputtering power test	21
3.2	θ -2 θ scan for the second test batch, with a magnification of the Pt (111) peak	22
3.3	θ -2 θ scan of the Pt(111) peaks fo the films deposited in the pressure test	23
3.4	Influence of deposition pressure on average crystallite size (a), deposition rate (b)	24
3.4	(continued) Influence of deposition pressure on resistivity (c), roughness (d) and average residual stress (e)	25
3.5	θ -2 θ scan of the Pt(111) peaks of the two batches of films deposited with the combined	
3.6	recipe for adhesion layer and bottom electrode. θ -2 θ scans of the Pt(111) peaks of film deposited before PM2 contamination, with PM2	26
	contaminated and after PM2 cleaning.	27
4.1	θ -2 θ scan of the first AlN film deposited, with peaks indexed	30
4.2	SEM image of a defect in the first AlN film deposited	30
4.3	θ -2 θ scan of the second AlN film deposited	31
4.4	Effect of pressure deposition on deposition rate of AlN. Linear fit with corresponding R ² included	32
4.5	θ -2 θ scans for AlN(002) peaks of the film deposited at varying pressures	32
4.6	Effect of pressure deposition on average crystallite size of AlN	33
4.7	Effect of pressure deposition on average stress of AlN films	33
4.8	θ -2 θ scans of the AlN(002) peaks of the films deposited on the bias test	34
4.9	Confront of the rocking curve for AlN films deposited on tensile and compressive stressed	
	Pt electrodes	35
	Effect of total gas flux on the deposition rate for the films deposited at different N_2 ratios.	37
	Effect of N_2 ratio on the residual stress of the films (a) and the crystallite size (b)	37
	θ -2 θ scans of the AlN (002) peak for films deposited at different N ₂ ratios	38
	-	
	3D visualization of AFM measures of the surface of the film deposited on patterned platinum	
	2D visualization of AFM measures of the surface of the film deposited on patterned platinum	40
4.16	Linear fitting of the Sc concentration against the Sc sputtering power ratio from [37], used to determine the deposition parameters	41
4.17	Effect of total sputtering power on deposition rate of AlScN. Linear fit results with cor-	
	responding R ² value included	42
4.18	Effect of total sputtering power on residual stress values of AlScN thin films	42
4.19	Correlation between Sc concentration in film and Sc sputtering power ratio. Linear fit	
	results with corresponding R^2 included	43
5.1	Layout for the bottom electrode etching mask	46
5.2	Layout for the top electrode etching mask	46
5.3	HBAR top electrode	48

5.4	Magnification of the bottom electrode surface, with barnacle-like structures	49
5.5	Admittance frequency response of a circular HBAR with diameter of 1600 µm excited	
	between 0.5 and 12 GHz	50
5.6	Admittance frequency response of a circular HBAR with diameter of 1600 µm excited	
	between 4.75 and 5.75 GHz	50
5.7	SEM image of an edge of one of the FBAR's bottom electrodes	51
5.8	SEM image of the edge of an FBAR bottom electrode covered with AlN aggregates	52
5.9	Photography of an unreleased FBAR. The dark area around the active area is where the	
	Si has been etched.	53
5.10	Side view of a released FBAR	53
5.11	Admittance frequency response of a FBAR device with pentagonal active area	54
5.12	Reflection coefficient frequency response of a FBAR device with pentagonal active area.	55

List of Tables

2.1	Preliminary process flow	1
2.1	(continued) Preliminary process flow	8
3.1	Summary of metal properties. AlN properties reported too at the end. The mismatch	
	refers to the in-plane lattice parameter [79–85]	19
3.2	Deposition parameters for the adhesion layer test	20
3.3	Results summary for the adhesion layer test	20
3.4	Deposition parameters for the sputtering power test	20
3.5	Deposition parameters for the second test batch	21
3.6	Deposition parameters for the pressure test	23
3.7	Summary of results from the pressure deposition test	24
3.8	Results summary for the combined recipe result	26
3.9	Optimized parameters for Pt sputtering.	27
3.10	Confront between 50 nm Pt electrodes deposited with different sputtering tools	28
4.1	Basic recipe for the deposition of AlN in CT200	29
4.2	Summary of results from the pressure deposition test	32
4.3	Summary of results from the bias deposition test	35
4.4	Deposition parameters for the gas ratio test	36
4.5	Summary of results from the gas ratio deposition test	38
4.6	Parameters for the first optimized recipe	39
4.7	Confront of film properties between film deposited on patterned and non-patterned growth	
	layers	39
4.8	Parameters for the second optimized recipe, used for FBAR production	39
4.9	Deposition parameters for the Sc concentration test	41
4.10	Atomic concentration of N, Al and Sc measured by EDX for AlScN thin films on Si at 8	
	kV and 10 kV electrons accelerating voltages	43
4.11	Results summary for the Sc doping test	43

Abbreviation and symbol list

6.1 Symbols

 P_{sub}

 R_0

 $R_p \\ R_q$

α	Thermal expansion coefficient (K^{-1})
β	FWHM of θ -2 θ scans peaks (°)
Δ	Ellipsometry parameter, polarization difference between incident and reflected light (°)
Δt_f	Maximum variation between thickness values of the film, in percentual
$oldsymbol{arepsilon^{S}}$	Permittivity matrix at constant strain (F m ⁻¹)
$egin{array}{c} \Delta t_f \ arepsilon^S \ arepsilon^S \end{array}$	Permittivity matrix at constant stress (F m ⁻¹)
$ heta_B$	Bragg angle, for which a diffraction peak is measured (°)
λ	X-Ray wavelength (nm)
u	Poisson Module
ho	Density (kg m $^{-3}$)
$ ho_e$	Electrical resistivity (Ω m)
au	Average crystallite size (nm)
Ψ	Ellipsometry parameter, angle whose tangent is the ratio between the module of R_p and R_s (°)
a	Crystalline lattice parameter (pm)
c	Crystalline lattice parameter (pm)
c^E	Stiffness matrix measured at constant electric field (GPa)
D	Electric displacement ($C m^{-2}$)
D_{TS}	Target-Substrate Distance in a sputtering tool (mm)
d_{ij}	Piezoelectric strain coefficient, i direction of the field, j of the strain (pC N ⁻ 1)
E	Isotropic Young Modulus (Pa)
$oldsymbol{E}$	Electric Field (V m ⁻ 1)
e_{ij}	Piezoelectric stress coefficient, i direction of the field, j of the stress (C m^{-2})
f_a	Anti-resonance frequency (Hz)
f_r	Resonance frequency (Hz)
F_{Ar}	Flux of Ar in the deposition chamber (sccm)
F_{N2}	Flux of N_2 in the deposition chamber (sccm)
F_{tot}	Total Gas Flux in the deposition chamber (sccm)
h	Substrate thickness (µm)
K	Scherrer Shape Factor
k_b	Boltzmann constant
$\begin{array}{c} k_b \\ k_{eff}^2 \\ k_{33}^2 \end{array}$	Effective piezoelectric coupling coefficient
k_{33}^2	Piezoelectric coupling coefficient for a wurtzite lattice along the c-axis
L_{mean}	Mean Free Path (m)
P	Pressure (Pa)
P_{Al}	Power delivered to the Al cathode (W)
P_{Sc}	Power delivered to the Sc cathode (W)
P_{Sub}	Power delivered to the substrate (W)
P_{tot}	Total Sputtering power (W)
Q_a	FBAR anti-resonance frequency Quality Factor
Q_{hit}	Collision probability
Q_r	FBAR resonance frequency Quality Factor
1)	Darron dalarrona di ta the a grale atrocta (W/)

Power delivered to the substrate (W)

Root Mean Squared roughness (nm)

Curvature radius of wafer before film deposition (m)

Total reflection coefficient (complex) along the direction perpendicular to the film surface

 R_s Total reflection coefficient (complex) along the direction parallel to the film surface

 R_{sh} Sheet resistance (Ω/sq)

 R_t Curvature radius of wafer after film deposition (m)

 r_{dep} Deposition rate (nm min⁻¹)

 $r_{P,Sc}$ Ratio of Sc sputtering power to total sputtering power

 r_{mean} Mean radius of particles in a plasma

S Strain

 S_{11} FBAR Reflection coefficient (dB) s^E Elastic Compliance Matrix (m N⁻¹)

T Stress (MPa)

 T_{av} Average residual stress in films, positive values for tensile stresses (MPa)

 T_{dep} Deposition temperature (°C)

 t_f Film thickness (nm) v_a Acoustic velocity (m s⁻¹)

 x_{Sc} Ratio of Scandium atomic concentration to total metal atomic concentration in AlScN

6.2 Abbreviations

AFM Atomic Force Microscopy/Microscope

AIN Aluminium Nitride

AlScN Scandium Aluminium Nitride alloy AOG Abnormally Oriented Grains

BAW Bulk Acoustic Wave

CMOS Complementary Metal-Oxide-Semiconductor

DC Direct Current

EDX Energy Dispersive X-Ray Spectroscopy
FBAR Free-standing Bulk Acoustic wave Resonator

FWHM Full-Width Half Maximum **GSG** Ground Signal Ground (Probe)

HBAR High-overtone Bulk Acoustic wave Resonator

HR High Resistivity

HiPIMS High-Power Impulse Magnetron Sputtering

ICP Inductively Coupled Plasma

IR Infrared radiation

MEMS Micro Electro Mechanical Systems

MLA MaskLess Aligner
p-DC pulsed Direct Current
PM Process Module
PR Photoresist

PVD Physical Vapour Deposition

RF Radio-Frequency
RT Room Temperature
SAW Surface Acoustic Wave

SEM Scanning Electron Microscopy
SIMS Secondary Ions Mass Spectroscopy

SiO₂ Silicon Oxide

TMAH Tetramethylammonium Hydroxide

UV Ultraviolet radiation
VNA Vector Network Analyzer

XeF₂ XPS Xenon Difluoride

X-Ray Photon Spectroscopy X-Ray Diffractometry X-Ray Reflectometry XRD XRR

References

- [1] Zhe Cheng. "Experimental Observation of High Intrinsic Thermal Conductivity of AlN". In: *Physical Review Materials* 4.4 (2020). DOI: 10.1103/PhysRevMaterials.4.044602.
- [2] Martin Feneberg et al. "High-Excitation and High-Resolution Photoluminescence Spectra of Bulk AlN". In: *Physical Review B* 82.7 (Aug. 16, 2010), p. 075208. DOI: 10.1103/PhysRevB.82.075208. URL: https://link.aps.org/doi/10.1103/PhysRevB.82.075208 (visited on 09/28/2025).
- [3] M. Kazan et al. "Elastic Constants of Aluminum Nitride". In: *physica status solidi c* 4.1 (2007), pp. 204–207. ISSN: 1610-1642. DOI: 10.1002/pssc.200673503. URL: https://onlinelibrary.wiley.com/doi/abs/10.1002/pssc.200673503 (visited on 09/28/2025).
- [4] Heinz Schulz and K. H. Thiemann. "Crystal Structure Refinement of AlN and GaN". In: Solid State Communications 23.11 (Sept. 1, 1977), pp. 815-819. ISSN: 0038-1098. DOI: 10.1016/0038-1098(77)90959-0. URL: https://www.sciencedirect.com/science/article/pii/0038109877909590 (visited on 09/28/2025).
- [5] Chengjie Zuo, Nipun Sinha, and Gianluca Piazza. "Very High Frequency Channel-Select MEMS Filters Based on Self-Coupled Piezoelectric AlN Contour-Mode Resonators". In: Sensors and Actuators A: Physical 160.1 (May 1, 2010), pp. 132–140. ISSN: 0924-4247. DOI: 10.1016/j.sna.2010.04.011. URL: https://www.sciencedirect.com/science/article/pii/S0924424710001731 (visited on 09/28/2025).
- [6] Hongliang Zu et al. "Optimal Preparation of AlN Thin Films on Sapphire Substrate and Its Effective Validation in SAW Resonators". In: *Vacuum* 237 (July 1, 2025), p. 114182. ISSN: 0042-207X. DOI: 10.1016/j.vacuum.2025.114182. URL: https://www.sciencedirect.com/science/article/pii/S0042207X25001721 (visited on 09/28/2025).
- [7] Vladimir N. Popok et al. "Magnetron Sputter Grown AlN Nanostructures with Giant Piezoelectric Response toward Energy Generation". In: ACS Applied Nano Materials 6.10 (May 26, 2023), pp. 8849–8856. DOI: 10.1021/acsanm.3c01250. URL: https://doi.org/10.1021/acsanm.3c01250 (visited on 09/28/2025).
- [8] Gwiy-Sang Chung and Byung-Chul Lee. "Fabrication and Characterization of Vibration-Driven AlN Piezoelectric Micropower Generator Compatible with Complementary Metal-Oxide Semiconductor Process". In: *Journal of Intelligent Material Systems and Structures* 26.15 (Oct. 1, 2015), pp. 1971–1979. ISSN: 1045-389X. DOI: 10.1177/1045389X14546649. URL: https://doi.org/10.1177/1045389X14546649 (visited on 09/28/2025).
- [9] Ting-Ta Yen et al. "Corrugated Aluminum Nitride Energy Harvesters for High Energy Conversion Effectiveness". In: *Journal of Micromechanics and Microengineering* 21.8 (July 2011), p. 085037. ISSN: 0960-1317. DOI: 10.1088/0960-1317/21/8/085037 (visited on 09/28/2025).
- [10] Yuanhang Qu et al. "Novel AlN/ScAlN Composite Film SAW for Achieving Highly Sensitive Temperature Sensors". In: Sensors and Actuators A: Physical 381 (Jan. 1, 2025), p. 116079. ISSN: 0924-4247. DOI: 10.1016/j.sna.2024.116079. URL: https://www.sciencedirect.com/science/article/pii/S0924424724010732 (visited on 09/28/2025).
- [11] Hui Wang et al. "Temperature Performance Study of SAW Sensors Based on AlN and AlScN". In: *Micromachines* 14.5 (5 May 2023), p. 1065. ISSN: 2072-666X. DOI: 10.3390/mi14051065. URL: https://www.mdpi.com/2072-666X/14/5/1065 (visited on 04/14/2025).
- [12] Benpeng Zhu et al. "Self-Focused AlScN Film Ultrasound Transducer for Individual Cell Manipulation". In: ACS Sensors 2.1 (Jan. 27, 2017), pp. 172-177. DOI: 10.1021/acssensors.6b00713. URL: https://doi.org/10.1021/acssensors.6b00713 (visited on 09/28/2025).
- [13] K. Momma and F. Izumi. "VESTA 3 for Three-Dimensional Visualization of Crystal, Volumetric and Morphology Data". In: *Journal of Applied Crystallography* 44.6 (Dec. 1, 2011), pp. 1272–1276. ISSN: 0021-8898. DOI: 10.1107/S0021889811038970. URL: https://journals.iucr.org/j/issues/2011/06/00/db5098/ (visited on 09/28/2025).
- [14] "IEEE Standard on Piezoelectricity". In: ANSI/IEEE Std 176-1987 (1988), 0_1-. DOI: 10.1109/IEEESTD. 1988.79638. URL: https://ieeexplore.ieee.org/document/26560 (visited on 09/26/2025).

- [15] Morito Akiyama et al. "Enhancement of Piezoelectric Response in Scandium Aluminum Nitride Alloy Thin Films Prepared by Dual Reactive Cosputtering". In: *Advanced Materials* 21.5 (2009), pp. 593-596. ISSN: 1521-4095. DOI: 10.1002/adma.200802611. URL: https://onlinelibrary.wiley.com/doi/abs/10.1002/adma.200802611 (visited on 04/11/2025).
- [16] Bhadri Narayanan KN, Deleep R. Nair, and Amitava DasGupta. "Extraction of D31 Piezoelectric Coefficient of AlN Thin Film". In: 2021 IEEE 34th International Conference on Micro Electro Mechanical Systems (MEMS). 2021 IEEE 34th International Conference on Micro Electro Mechanical Systems (MEMS). Jan. 2021, pp. 623–625. DOI: 10.1109/MEMS51782.2021.9375172. URL: https://ieeexplore.ieee.org/document/9375172 (visited on 09/28/2025).
- [17] Ting Lv et al. "Fabrication and Characterization of High-Temperature AlN Thick-Film Piezoelectric Accelerometer". In: Ceramics International 50 (22, Part B Nov. 15, 2024), pp. 47008—47016. ISSN: 0272-8842. DOI: 10.1016/j.ceramint.2024.09.051. URL: https://www.sciencedirect.com/science/article/pii/S027288422404015X (visited on 09/28/2025).
- [18] Cícero L. A. Cunha et al. "Development and Applications of Aluminum Nitride Thin Film Technology". In: *Thin Films Deposition Methods and Applications*. IntechOpen, Aug. 1, 2022. ISBN: 978-1-80356-456-2. DOI: 10.5772/intechopen.106288. URL: https://www.intechopen.com/chapters/82904 (visited on 09/28/2025).
- [19] Nabeel Ahmad Khan Jadoon et al. "Recent Advances in Aluminum Nitride (AlN) Growth by Magnetron Sputtering Techniques and Its Applications". In: *Inorganics* 12.10 (Oct. 2024), p. 264. ISSN: 2304-6740. DOI: 10.3390/inorganics12100264. URL: https://www.mdpi.com/2304-6740/12/10/264 (visited on 09/28/2025).
- [20] Philipus N. Hishimone et al. "Methods of Fabricating Thin Films for Energy Materials and Devices". In: Lithium-Ion Batteries Thin Film for Energy Materials and Devices. IntechOpen, July 8, 2020. ISBN: 978-1-78985-464-0. DOI: 10.5772/intechopen.85912. URL: https://www.intechopen.com/chapters/70339 (visited on 09/29/2025).
- [21] Cícero L. A. Cunha, Tales C. Pimenta, and Mariana A. Fraga. "Growth and Properties of Sputtered Highly (100)-Oriented Oxygenated AlN Thin Films for SAW Sensing Applications". In: *Microsystem Technologies* 27.10 (Oct. 1, 2021), pp. 3773–3782. ISSN: 1432-1858. DOI: 10.1007/s00542-020-05165-1. URL: https://doi.org/10.1007/s00542-020-05165-1 (visited on 09/29/2025).
- [22] John A. Thornton. "The Microstructure of Sputter □ deposited Coatings". In: *Journal of Vacuum Science & Technology A* 4.6 (Nov. 1, 1986), pp. 3059–3065. ISSN: 0734-2101. DOI: 10.1116/1.573628. URL: https://doi.org/10.1116/1.573628 (visited on 04/11/2025).
- [23] M. A. Signore et al. "Structural and Morphological Evolution of Aluminum Nitride Thin Films: Influence of Additional Energy to the Sputtering Process". In: *Journal of Physics and Chemistry of Solids* 74.10 (Oct. 1, 2013), pp. 1444–1451. ISSN: 0022-3697. DOI: 10.1016/j.jpcs.2013.05.003. URL: https://www.sciencedirect.com/science/article/pii/S0022369713001911 (visited on 09/24/2025).
- Zhaoxuan Wei et al. "The Evolution of Preferred Orientation and Morphology of AlN Films under Various Sputtering Parameters". In: *Journal of Crystal Growth* 625 (Jan. 1, 2024), p. 127439. ISSN: 0022-0248. DOI: 10.1016/j.jcrysgro.2023.127439. URL: https://www.sciencedirect.com/science/article/pii/S0022024823003652 (visited on 09/29/2025).
- [25] Manohar Chirumamilla et al. "Magnetron Sputter Deposition of Nanostructured AlN Thin Films". In: *Applied Nano* 4.4 (Dec. 2023), pp. 280–292. ISSN: 2673-3501. DOI: 10.3390/applnano4040016. URL: https://www.mdpi.com/2673-3501/4/4/16 (visited on 09/29/2025).
- [26] V. R. Shayapov et al. "Highly Textured AIN Films Deposited by Pulsed DC Magnetron Sputtering with Optimized Process Parameters". In: *Solid State Communications* 397 (Mar. 1, 2025), p. 115821. ISSN: 0038-1098. DOI: 10.1016/j.ssc.2024.115821. URL: https://www.sciencedirect.com/science/article/pii/S0038109824003983 (visited on 09/24/2025).
- [27] Shakil Khan et al. "Texture of the Nano-Crystalline AlN Thin Films and the Growth Conditions in DC Magnetron Sputtering". In: *Progress in Natural Science: Materials International* 25.4 (Aug. 1, 2015), pp. 282–290. ISSN: 1002-0071. DOI: 10.1016/j.pnsc.2015.08.006. URL: https://www.sciencedirect.com/science/article/pii/S1002007115000842 (visited on 09/24/2025).

- [28] Matilde Kammer Sandager, Christian Kjelde, and Vladimir Popok. "Growth of Thin AlN Films on Si Wafers by Reactive Magnetron Sputtering: Role of Processing Pressure, Magnetron Power and Nitrogen/Argon Gas Flow Ratio". In: *Crystals* 12.10 (Oct. 2022), p. 1379. ISSN: 2073-4352. DOI: 10.3390/cryst12101379. URL: https://www.mdpi.com/2073-4352/12/10/1379 (visited on 09/29/2025).
- [29] Xianming He et al. "A Micro-Electromechanical Systems Based Vibration Energy Harvester with Aluminum Nitride Piezoelectric Thin Film Deposited by Pulsed Direct-Current Magnetron Sputtering". In: Applied Energy 228 (Oct. 15, 2018), pp. 881–890. ISSN: 0306-2619. DOI: 10.1016/j.apenergy.2018.07.001. URL: https://www.sciencedirect.com/science/article/pii/S0306261918310286 (visited on 09/28/2025).
- [30] F. Medjani et al. "Effect of Substrate Temperature and Bias Voltage on the Crystallite Orientation in RF Magnetron Sputtered AlN Thin Films". In: *Thin Solid Films*. INTERNATIONAL CONFERENCE ON SURFACES, COATINGS AND NANOSTRUCTURED MATERIALS 515.1 (Sept. 25, 2006), pp. 260–265. ISSN: 0040-6090. DOI: 10.1016/j.tsf.2005.12.145. URL: https://www.sciencedirect.com/science/article/pii/S0040609005024193 (visited on 09/24/2025).
- [31] Genshui Ke et al. "Highly C-Axis Oriented AlN Film Grown by Unbalanced Magnetron Reactive Sputtering and Its Electrical Properties". In: *Journal of Alloys and Compounds* 646 (Oct. 15, 2015), pp. 446–453. ISSN: 0925-8388. DOI: 10.1016/j.jallcom.2015.05.174. URL: https://www.sciencedirect.com/science/article/pii/S0925838815300736 (visited on 09/28/2025).
- [32] Yasuyoshi Saito et al. "Lead-Free Piezoceramics". In: *Nature* 432.7013 (Nov. 2004), pp. 84–87. ISSN: 1476-4687. DOI: 10.1038/nature03028. URL: https://www.nature.com/articles/nature03028 (visited on 09/29/2025).
- [33] Marco Liffredo et al. "Piezoelectric and Elastic Properties of Al0.60Sc0.40N Thin Films Deposited on Patterned Metal Electrodes". In: *Journal of Vacuum Science & Technology A* 42.4 (May 15, 2024), p. 043404. ISSN: 0734-2101. DOI: 10.1116/6.0003497. URL: https://doi.org/10.1116/6.0003497 (visited on 09/22/2025).
- [34] Ferenc Tasnádi et al. "Origin of the Anomalous Piezoelectric Response in Wurtzite Sc_xAl_{1-x}N Alloys". In: *Physical Review Letters* 104.13 (Apr. 2, 2010), p. 137601. DOI: 10.1103/PhysRevLett.104.137601. URL: https://link.aps.org/doi/10.1103/PhysRevLett.104.137601 (visited on 04/11/2025).
- [35] Nicolas Kurz et al. "Experimental Determination of the Electro-Acoustic Properties of Thin Film AlScN Using Surface Acoustic Wave Resonators". In: *Journal of Applied Physics* 126.7 (Aug. 15, 2019), p. 075106. ISSN: 0021-8979. DOI: 10.1063/1.5094611. URL: https://doi.org/10.1063/1.5094611 (visited on 09/26/2025).
- [36] Shiro Satoh et al. "Crystal Structure Deformation and Phase Transition of AlScN Thin Films in Whole Sc Concentration Range". In: *Journal of Applied Physics* 132.2 (July 11, 2022), p. 025103. ISSN: 0021-8979. DOI: 10.1063/5.0087505. URL: https://doi.org/10.1063/5.0087505 (visited on 06/12/2025).
- [37] Rossiny Beaucejour et al. "Controlling Residual Stress and Suppression of Anomalous Grains in Aluminum Scandium Nitride Films Grown Directly on Silicon". In: *Journal of Microelectromechanical Systems* 31.4 (Aug. 2022), pp. 604–611. ISSN: 1941-0158. DOI: 10.1109/JMEMS.2022.3167430. URL: https://ieeexplore.ieee.org/document/9770129 (visited on 04/11/2025).
- [38] Simon Fichtner et al. "AlScN: A III-V Semiconductor Based Ferroelectric". In: *Journal of Applied Physics* 125.11 (Mar. 18, 2019), p. 114103. ISSN: 0021-8979. DOI: 10.1063/1.5084945. URL: https://doi.org/10.1063/1.5084945 (visited on 06/12/2025).
- [39] Sergey Mishin and Yury Oshmyansky. "Magnetron Deposition of AlN and ScAlN for Mass-production for BAW Devices and MEMS". In: 2019 IEEE International Ultrasonics Symposium (IUS). 2019 IEEE International Ultrasonics Symposium (IUS). Oct. 2019, pp. 891–893. DOI: 10.1109/ULTSYM.2019. 8925969. URL: https://ieeexplore.ieee.org/document/8925969 (visited on 09/28/2025).
- [40] Alliance Concept. Clustertool with vacuum robot, CT200. Brochure. URL: https://www.alliance-concept.com/wp-content/uploads/brochure/UK/CT200_en.pdf (visited on 09/14/2025).
- [41] Pfeiffer SPIDER 600. EPFL. URL: https://www.epfl.ch/research/facilities/cmi/equipment/thin-films/pfeiffer-spider-600/ (visited on 09/14/2025).
- [42] Alliance Concept. *Thin layer coating by evaporation, EVA450*. Brochure. URL: https://www.alliance-concept.com/wp-content/uploads/brochure/UK/EVA450_en.pdf (visited on 09/14/2025).

- [43] EVG. EVG®150 Automated Resist Processing System. Brochure. URL: https://www.evgroup.com/fileadmin/media/products/lithography/resist_processing/evg150/EVG150_200mm_Flyer_23_01.pdf (visited on 09/14/2025).
- [44] Merck. Technical datasheet AZ® ECI 3000 Series. Brochure. 2021. URL: https://www.microchemicals.com/dokumente/datenblaetter/tds/merck/en/tds_az_eci_3000_series.pdf (visited on 09/14/2025).
- [45] Merck. Technical datasheet AZ® Organic Developers. Brochure. 2021. URL: https://www.microchemicals.com/dokumente/datenblaetter/tds/merck/en/tds_az_mif_developer.pdf (visited on 09/14/2025).
- [46] Heidelberg Instruments. MLA 150 THE ADVANCED MASKLESS ALIGNER. Brochure. URL: https://heidelberg-instruments.com/wp-content/uploads/2025/06/Heidelberg-Instruments-MLA150-Datasheet.pdf (visited on 09/14/2025).
- [47] NEXUS IBE Ion Beam Etch System. Veeco. URL: https://www.veeco.com/products/nexus-420si-ibe-ion-beam-etch-system/ (visited on 09/14/2025).
- [48] Etch | KLA. URL: https://www.kla.com/products/chip-manufacturing/etch (visited on 09/14/2025).
- [49] PVA Tepla. Resist Ashing System GIGAbatch 310 M. Brochure. URL: https://www.mbelectronique.fr/Web_PDF/1260_2016102015271263_Plasma-microwave_GIGAbatch-310-M_Specifications.pdf (visited on 09/14/2025).
- [50] Shipley. SVC-14 Datasheet. Brochure. URL: https://www.epfl.ch/research/facilities/cmi/wp-content/uploads/2024/09/TDS_SVC14.pdf (visited on 09/14/2025).
- [51] Don Berlincourt and Helmut H. A. Krueger. "Domain Processes in Lead Titanate Zirconate and Barium Titanate Ceramics". In: *Journal of Applied Physics* 30.11 (Nov. 1, 1959), pp. 1804–1810. ISSN: 0021-8979. DOI: 10.1063/1.1735059. URL: https://doi.org/10.1063/1.1735059 (visited on 09/14/2025).
- [52] Mark Stewart and Markys G. Cain. "Direct Piezoelectric Measurement: The Berlincourt Method". In: *Characterisation of Ferroelectric Bulk Materials and Thin Films*. Ed. by Markys G. Cain. Dordrecht: Springer Netherlands, 2014, pp. 37–64. ISBN: 978-1-4020-9311-1. DOI: 10.1007/978-1-4020-9311-1_3. URL: https://doi.org/10.1007/978-1-4020-9311-1_3 (visited on 09/28/2025).
- [53] George Gerald Stoney. "The Tension of Metallic Films Deposited by Electrolysis". In: *Proceedings of the Royal Society of London. Series A, Containing Papers of a Mathematical and Physical Character* 82.553 (Jan. 1909), pp. 172–175. DOI: 10.1098/rspa.1909.0021. URL: https://royalsocietypublishing.org/doi/10.1098/rspa.1909.0021 (visited on 09/14/2025).
- [54] Toho technologies. FLX 2320-S. Brochure. URL: https://tohotechnology.com/wp-content/uploads/2019/09/Toho_FLX2320S_D1.pdf (visited on 09/14/2025).
- [55] Filmetrics® R50-4PP Four-Point Probe System and Filmetrics R50-EC Eddy Current System | Sheet Resistance Measurement. KLA. URL: https://www.kla.com/products/instruments/sheet-resistance-measurement/filmetrics-r50 (visited on 09/14/2025).
- [56] Harland G Tompkins and James N Hilfiker. *Spectroscopic ellipsometry: practical application to thin film characterization*. Momentum Press, 2015.
- [57] J.A. Woollam. RC2. Brochure. URL: https://www.jawoollam.com/download/pdfs/rc2-brochure.pdf (visited on 09/14/2025).
- [58] J.A. Woollam. CompleteEASE. Brochure. 2022. URL: https://www.jawoollam.com/download/pdfs/completeease-brochure.pdf (visited on 09/14/2025).
- [59] Dimension FastScan AFM. URL: https://www.bruker.com/en/products-and-solutions/microscopes/materials-afm/dimension-fastscan.html (visited on 09/14/2025).
- [60] ScanAsyst-Fluid Plus | Veeco Probes | Bruker AFM Probes. URL: https://www.brukerafmprobes.com/p-3728-scanasyst-fluid.aspx (visited on 09/14/2025).
- [61] Home The Nanoscale World. URL: http://nanoscaleworld.bruker-axs.com/nanoscaleworld/ (visited on 09/28/2025).
- [62] Oxford Instruments. X-Max The largest area SDD. Brochure. 2008. URL: https://documents.uow.edu.au/content/groups/public/@web/@aiim/documents/doc/uow154676.pdf (visited on 09/14/2025).

- [63] George F. Harrington and José Santiso. "Back-to-Basics Tutorial: X-ray Diffraction of Thin Films". In: *Journal of Electroceramics* 47.4 (Dec. 1, 2021), pp. 141–163. ISSN: 1573-8663. DOI: 10.1007/s10832-021-00263-6. URL: https://doi.org/10.1007/s10832-021-00263-6 (visited on 09/15/2025).
- [64] A. L. Patterson. "The Scherrer Formula for X-Ray Particle Size Determination". In: *Physical Review* 56.10 (1939), pp. 978–982. DOI: 10.1103/PhysRev.56.978.
- [65] V X-rayreflectivitymeasurement. "X-Ray Thin-Film Measurement Techniques". In: ().
- [66] Bruker. Product Sheet XRD 45 D8 DISCOVER Plus. Brochure. 2017. URL: https://www.syntechinnovation.com/images/catalog/advance-analytical/5X-ray/XRD/D8_discover.pdf (visited on 09/14/2025).
- [67] EIGER2 R Detectors. URL: https://www.bruker.com/en/products-and-solutions/diffractometers-and-x-ray-microscopes/x-ray-diffractometers/davinci-components/detectors/EIGER2-R-500K-detector.html (visited on 09/14/2025).
- [68] DIFFRAC.EVA. URL: https://www.bruker.com/en/products-and-solutions/diffractometers-and-x-ray-microscopes/x-ray-diffractometers/diffrac-suite-software/diffrac-eva.html (visited on 09/14/2025).
- [69] DIFFRAC.LEPTOS. URL: https://www.bruker.com/en/products-and-solutions/diffractometers-and-x-ray-microscopes/x-ray-diffractometers/diffrac-suite-software/diffrac-leptos.html (visited on 09/28/2025).
- [70] MPICorporation. MPI Probe Selection Guide. Brochure. 2023. URL: https://www.mpi-corporation.com/wp-content/uploads/ASTPDF/MPI-Probe-Selection-Guide.pdf (visited on 09/15/2025).
- [71] Rohde Schwarz. RS®ZNB VECTOR NETWORK ANALYZER. Brochure. 2021. URL: https://scdn.rohde-schwarz.com/ur/pws/dl_downloads/pdm/cl_brochures_and_datasheets/product_brochure/3608_3278_12/ZNB_bro_en_3608-3278-12_v0500.pdf (visited on 09/15/2025).
- [72] Tao Zhang et al. "Effects of Electrodes on Performance Figures of Thin Film Bulk Acoustic Resonators". In: The Journal of the Acoustical Society of America 122.3 (Sept. 1, 2007), pp. 1646–1651. ISSN: 0001-4966. DOI: 10.1121/1.2764473. URL: https://pubs.aip.org/asa/jasa/article/122/3/1646/853621/Effects-of-electrodes-on-performance-figures-of (visited on 09/17/2025).
- [73] Tianji Zhou. "Resistivity Scaling Due to Electron Surface Scattering in Thin Metal Layers". In: *Physical Review B* 97.16 (2018). DOI: 10.1103/PhysRevB.97.165406.
- [74] Marc-Alexandre Dubois and Paul Muralt. "Stress and Piezoelectric Properties of Aluminum Nitride Thin Films Deposited onto Metal Electrodes by Pulsed Direct Current Reactive Sputtering". In: *Journal of Applied Physics* 89.11 (June 1, 2001), pp. 6389–6395. ISSN: 0021-8979. DOI: 10.1063/1.1359162. URL: https://doi.org/10.1063/1.1359162 (visited on 04/11/2025).
- [75] Juan Xiong et al. "Influence of Substrate Metals on the Crystal Growth of AlN Films". In: *International Journal of Minerals, Metallurgy, and Materials* 17.1 (Feb. 1, 2010), pp. 98–103. ISSN: 1869-103X. DOI: 10.1007/s12613-010-0117-y. URL: https://doi.org/10.1007/s12613-010-0117-y (visited on 04/11/2025).
- [76] R. Jakkaraju et al. "Integrated Approach to Electrode and AlN Depositions for Bulk Acoustic Wave (BAW) Devices". In: *Microelectronic Engineering*. Materials for Advanced Metallization 2003 70.2 (Nov. 1, 2003), pp. 566–570. ISSN: 0167-9317. DOI: 10.1016/S0167-9317(03)00386-1. URL: https://www.sciencedirect.com/science/article/pii/S0167931703003861 (visited on 09/17/2025).
- [77] Jin-Bock Lee et al. "Effects of Bottom Electrodes on the Orientation of AlN Films and the Frequency Responses of Resonators in AlN-based FBARs". In: *Thin Solid Films*. Proceedings of the 30th International Conference on Metallurgical Coatings and Thin Films 447–448 (Jan. 30, 2004), pp. 610–614. ISSN: 0040-6090. DOI: 10.1016/j.tsf.2003.07.023. URL: https://www.sciencedirect.com/science/article/pii/S0040609003012744 (visited on 09/18/2025).
- [78] R. E. Sah et al. "Crystallographic Texture of Submicron Thin Aluminum Nitride Films on Molybdenum Electrode for Suspended Micro and Nanosystems". In: ECS Journal of Solid State Science and Technology 2.4 (Feb. 20, 2013), P180. ISSN: 2162-8777. DOI: 10.1149/2.001305jss. URL: https://iopscience.iop.org/article/10.1149/2.001305jss/meta (visited on 09/18/2025).
- [79] John W. Arblaster. Selected Values of the Crystallographic Properties of Elements. 1 online resource (700 pages): illustrations vols. Materials Park: A S M International, 2018. ISBN: 1-62708-155-0 978-1-62708-155-9. URL: https://search.ebscohost.com/login.aspx?direct=true&scope=site&db=nlebk&db=nlabk&AN=1884539.

- [80] P. D. Desai, H. M. James, and C. Y. Ho. "Electrical Resistivity of Aluminum and Manganese". In: *Journal of Physical and Chemical Reference Data* 13.4 (Oct. 1, 1984), pp. 1131–1172. ISSN: 0047-2689. DOI: 10.1063/1.555725. URL: https://doi.org/10.1063/1.555725 (visited on 09/21/2025).
- [81] R. A. Matula. "Electrical Resistivity of Copper, Gold, Palladium, and Silver". In: *Journal of Physical and Chemical Reference Data* 8.4 (Oct. 1, 1979), pp. 1147–1298. ISSN: 0047-2689. DOI: 10.1063/1.555614. URL: https://doi.org/10.1063/1.555614 (visited on 09/21/2025).
- [82] P. D. Desai et al. "Electrical Resistivity of Selected Elements". In: Journal of Physical and Chemical Reference Data 13.4 (Oct. 1984), pp. 1069-1096. ISSN: 0047-2689. DOI: 10.1063/1.555723. eprint: https://pubs.aip.org/aip/jpr/article-pdf/13/4/1069/9766234/1069_1_online.pdf. URL: https://doi.org/10.1063/1.555723.
- [83] C.W.C. "Thermophysical Data on Platinum: Resistivity and Conductivity Values Recommended". In: *Platinum Metals Review* 28.4 (Oct. 1, 1984), pp. 164–165. ISSN: 0032-1400. DOI: 10.1595/003214084X284 164165. URL: https://technology.matthey.com/content/journals/10.1595/003214084X284 164165 (visited on 09/21/2025).
- [84] Walter C. Michels and Sally Wilford. "The Physical Properties of Titanium. I. Emissivity and Resistivity of the Commercial Metal". In: *Journal of Applied Physics* 20.12 (Dec. 1, 1949), pp. 1223–1226. ISSN: 0021-8979. DOI: 10.1063/1.1698312. URL: https://doi.org/10.1063/1.1698312 (visited on 09/21/2025).
- [85] O. Ambacher. "Growth and Applications of Group III-nitrides". In: *Journal of Physics D: Applied Physics* 31.20 (Oct. 1998), p. 2653. ISSN: 0022-3727. DOI: 10.1088/0022-3727/31/20/001. URL: https://dx.doi.org/10.1088/0022-3727/31/20/001 (visited on 09/21/2025).
- [86] G. F. Iriarte, J. G. Rodríguez, and F. Calle. "Synthesis of C-Axis Oriented AlN Thin Films on Different Substrates: A Review". In: Materials Research Bulletin 45.9 (Sept. 1, 2010), pp. 1039–1045. ISSN: 0025-5408. DOI: 10.1016/j.materresbull.2010.05.035. URL: https://www.sciencedirect.com/science/article/pii/S0025540810002023 (visited on 04/11/2025).
- [87] Cinzia Caliendo and P. Massimiliano Latino. "Characterization of Pt/AlN/Pt-based Structures for High Temperature, Microwave Electroacoustic Devices Applications". In: *Thin Solid Films* 519.19 (July 29, 2011), pp. 6326-6329. ISSN: 0040-6090. DOI: 10.1016/j.tsf.2011.04.017. URL: https://www.sciencedirect.com/science/article/pii/S0040609011008297 (visited on 09/18/2025).
- [88] P. Schmid et al. "Influence of the AlN/Pt-ratio on the Electro-Mechanical Properties of Multilayered AlN/Pt Thin Film Strain Gauges at High Temperatures". In: Sensors and Actuators A: Physical 302 (Feb. 1, 2020), p. 111805. ISSN: 0924-4247. DOI: 10.1016/j.sna.2019.111805. URL: https://www.sciencedirect.com/science/article/pii/S0924424719315419 (visited on 09/20/2025).
- [89] G. Schmidl et al. "The Influence of Deposition Parameters on Ti/Pt Film Growth by Confocal Sputtering and the Temperature Dependent Resistance Behavior Using SiOx and Al2O3 Substrates". In: *Applied Surface Science* 313 (Sept. 15, 2014), pp. 267–275. ISSN: 0169-4332. DOI: 10.1016/j.apsusc.2014.05.203. URL: https://www.sciencedirect.com/science/article/pii/S0169433214012446 (visited on 05/09/2025).
- [90] E. Slavcheva et al. "Effect of Sputtering Parameters on Surface Morphology and Catalytic Efficiency of Thin Platinum Films". In: *Applied Surface Science* 255.13 (Apr. 15, 2009), pp. 6479-6486. ISSN: 0169-4332. DOI: 10.1016/j.apsusc.2009.02.033. URL: https://www.sciencedirect.com/science/article/pii/S0169433209001457 (visited on 05/09/2025).
- [91] Monjoy Sreemany and Suchitra Sen. "Effect of Substrate Temperature and Annealing Temperature on the Structural, Electrical and Microstructural Properties of Thin Pt Films by Rf Magnetron Sputtering". In: *Applied Surface Science* 253.5 (Dec. 30, 2006), pp. 2739–2746. ISSN: 0169-4332. DOI: 10.1016/j.apsusc.2006.05.040. URL: https://www.sciencedirect.com/science/article/pii/S016943 3206007537 (visited on 05/09/2025).
- [92] X-Ray Data Booklet. Center for X-ray Optics and Advanced Light Source, Lawrence Berkeley National Laboratory. Oct. 2009. URL: https://xdb.lbl.gov/ (visited on 09/26/2025).
- [93] Yafei Zhang and Da Chen. "Introduction". In: *Multilayer Integrated Film Bulk Acoustic Resonators*. Ed. by Yafei Zhang and Da Chen. Berlin, Heidelberg: Springer, 2013, pp. 1–14. ISBN: 978-3-642-31776-7. DOI: 10.1007/978-3-642-31776-7_1. URL: https://doi.org/10.1007/978-3-642-31776-7_1 (visited on 09/26/2025).

- [94] T. Baron et al. "High-Overtone Bulk Acoustic Resonator". In: *Modeling and Measurement Methods for Acoustic Waves and for Acoustic Microdevices*. IntechOpen, Aug. 28, 2013. ISBN: 978-953-51-1189-4. DOI: 10.5772/56175. URL: https://www.intechopen.com/chapters/45583 (visited on 07/03/2025).
- [95] Matthew A. Hopcroft, William D. Nix, and Thomas W. Kenny. "What Is the Young's Modulus of Silicon?" In: *Journal of Microelectromechanical Systems* 19.2 (Apr. 2010), pp. 229–238. ISSN: 1941-0158. DOI: 10.1109/JMEMS.2009.2039697. URL: https://ieeexplore.ieee.org/document/5430873 (visited on 09/27/2025).
- [96] ASM Handbook Committee. Properties and Selection: Nonferrous Alloys and Special-Purpose Materials. ASM International, Jan. 1, 1990. ISBN: 978-1-62708-162-7. DOI: 10.31399/asm.hb.v02.978162708 1627. URL: https://dl.asminternational.org/handbooks/edited-volume/14/Properties-and-Selection-Nonferrous-Alloys-and (visited on 09/27/2025).
- [97] Frank Z. Bi and Bradley P. Barber. "Bulk Acoustic Wave RF Technology". In: *IEEE Microwave Magazine* 9.5 (Oct. 2008), pp. 65–80. ISSN: 1557-9581. DOI: 10.1109/MMM.2008.927633. URL: https://ieeexplore.ieee.org/abstract/document/4622343 (visited on 09/27/2025).
- [98] Krishna Naishadham. "4 Transmission Lines". In: *The Electrical Engineering Handbook*. Ed. by WAI-KAI Chen. Burlington: Academic Press, Jan. 1, 2005, pp. 525-537. ISBN: 978-0-12-170960-0. DOI: 10.1016/B978-012170960-0/50040-2. URL: https://www.sciencedirect.com/science/article/pii/B9780121709600500402 (visited on 09/27/2025).

Acknowledgments

I firstly thank both Professor Ricciardi and Villanueva for letting me access this amazing learning experience, that showed me, even if in a small scale, the beauty of scientific research.

I am extremely grateful for the excellent guidance and support that Marco provided me during the whole period of the thesis. You encouraged me to continue my work with curiosity and determination in the face of many technical setbacks, and I could have not asked for anything better.

My gratitude is also extended to the whole Advanced NEMS Group for their support and for welcoming me in their laboratory.

I thank Allegra for having being an amazing friend and reference point for the months I spent in Lausanne. I thank Doruk for being an excellent friend during the hot month of August, and I thank Andrea, Francesco, Fabrizio, Sole, Roberta, and all the friends who made these university years a memorable experience.

I thank my parents and my family for their unconditional support during the year. I hope I made you proud.

And I thank Maria Luisa, for having crossed the Alps so many times to spend some time with me.

This thesis is dedicated to all who made it possible, and I couldn't be more grateful.